Multidisciplinary approach for mapping protein-protein interaction surfaces: from mass spectrometry to computational and cell biology

Inaugural-Dissertation

zur Erlangung des Doktorgrades
der Mathematisch-Naturwissenschaftlichen Fakultät
der Heinrich-Heine-Universität Düsseldorf

vorgelegt von

Francisco Javier Castilla Porras

aus San Pablo de Buceite (Spanien)

Jülich, September 2023

Aus dem Institut für Biologische Informationsprozesse, Molekular- und Zellphysiologie (IBI-1) des Forschungszentrums Jülich

Gedruckt mit der Genehmigung der
Mathematisch-Naturwissenschaften Fakultät der
Heinrich-Heine-Universität Düsseldorf

Referentin: Prof. Dr. Patricia Hidalgo
Korreferentin: Dr. Mercedes Alfonso-Prieto

Tag der mündlichen Prüfung:

Ich versichere an Eides Statt, dass die Dissertation von mir selbständig und ohne unzulässige fremde Hilfe unter `Beachtung der Grundsätze zur Sicherung guter wissenschaftlicher Praxis´ an der Heinrich-Heine-Universität Düsseldorf erstellt worden ist.

Ort, Datum Unterschrift

Index

List of figures

List of supplemental figures

List of tables

List of supplemental tables

Abstract

In excitable cells, voltage-gated calcium channels (VGCC) couple electrical signals to a variety of cellular processes such as hormone secretion, neurotransmission, or muscle contraction. These hetero-multimeric channels are mainly composed of four subunits (α_1, β, γ and $\alpha_2\delta$), being the α_1 subunit ($Ca_v\alpha_1$) and the β auxiliary subunit ($Ca_v\beta$) the core complex of the channel. Whereas $Ca_v\alpha_1$ contains the voltage-sensing domain (VSD) and forms the ion conduction pathway, $Ca_v\beta$ modulates the biophysical properties and controls the expression of the calcium channel at the plasma membrane.

$Ca_v\beta$ is a protein belonging to the MAGUK superfamily and composed of two functional domains: an Src homology 3 (SH3) domain and a guanylate kinase (GK) domain. $Ca_v\beta$ evolved as an interactive module that can form homodimers and interact with multiple proteins expanding its functional capabilities. However, the lack of structural data on these interactions has hindered our understanding of the functional roles that they could have on VGCC fate.

Here, by means of cross-linking mass spectrometry (XL-MS) and protein-protein docking, I uncovered the interaction interfaces of $Ca_v\beta$/F-actin and $Ca_v\beta/Ca_v\beta$ complexes. Structure-based site directed mutagenesis allowed for the validation of hotspots that help discern the roles of the corresponding $Ca_v\beta$/F-actin and $Ca_v\beta/Ca_v\beta$ interactions. First, the disruption of $Ca_v\beta$/F-actin complex resulted in a decreased number of functionally available VGCC in membrane, suggesting a role of this interaction in the quality control of channels at the cell surface. Second, the study of $Ca_v\beta$ dimerization showed that such dimers adopt a head-to-tail conformation stabilized by a disulphide bridge previously reported to be functionally relevant.

Altogether, the results presented in this thesis reveal two $Ca_v\beta$ protein-protein interfaces that regulate VGCC functional status and availability at the plasma membrane and provide novel druggable contact surfaces to target channel dysfunction in VGCC-associated disorders. Moreover, these results point out to a model where $Ca_v\beta$/F-actin and $Ca_v\beta/Ca_v\beta$ interactions are mutually exclusive, providing a structural basis why both interactions have different functional outcomes on VGCC membrane availability.

Zusammenfassung

In erregbaren Zellen koppeln spannungsgesteuerte Calciumkanäle (VGCC) elektrische Signale an eine Vielzahl zellulärer Prozesse, wie z.B. Hormonsekretion, Neurotransmission oder Muskelkontraktion. Diese heteromultimeren Kanäle bestehen hauptsächlich aus vier Untereinheiten (α_1-, β-, γ- und $\alpha_2\delta$-Untereinheit). Die α_1-Untereinheit ($Ca_v\alpha_1$) und die β-Hilfsuntereinheit ($Ca_v\beta$) bilden den Kernkomplex des Kanals. Während $Ca_v\alpha_1$ die spannungsempfindliche Domäne (VSD) enthält und den Ionenleitungsweg bildet, moduliert $Ca_v\beta$ die biophysikalischen Eigenschaften und kontrolliert die Expression der Calciumkanäle an der Plasmamembran.

$Ca_v\beta$ ist ein Protein, das zur MAGUK-Superfamilie gehört und aus zwei funktionellen Domänen besteht: einer Src-Homologie-3-Domäne (SH3) und einer Guanylatkinase-Domäne (GK). $Ca_v\beta$ entwickelte sich zu einem interaktiven Modul, das Homodimere bilden und mit mehreren Proteinen interagieren kann, wodurch seine funktionellen Fähigkeiten erweitert werden. Ein Mangel an Strukturdaten bzgl. dieser Interaktionen, führt dazu, dass wir bis heute die funktionelle Rolle nicht verstehen, die sie für das Schicksal von VGCC haben könnten.

Mittels Cross-Linking Massenspektrometrie (XL-MS) und Protein-Protein Docking konnte ich die Interaktionsschnittstellen von $Ca_v\beta$/F-Actin und $Ca_v\beta$/$Ca_v\beta$ Komplexen aufdecken. Die strukturbasierte ortsgerichtete Mutagenese ermöglichte mir die Validierung von Hotspots, die dabei halfen, die Rollen der entsprechenden $Ca_v\beta$/F-Actin und $Ca_v\beta$/$Ca_v\beta$ Wechselwirkungen zu erkennen. Die Spaltung des $Ca_v\beta$/F-Actin Komplexes führte zu einer verringerten Anzahl funktionell verfügbarer VGCC in der Membran, was auf eine Rolle dieser Wechselwirkung bei der Qualitätskontrolle von Kanälen an der Zelloberfläche schließen lässt. Außerdem zeigte die Untersuchung der $Ca_v\beta$ Dimerisierung, dass solche Dimere eine Kopf-Schwanz-Konformation annehmen, die durch eine Disulfidbrücke stabilisiert werden, von der zuvor berichtet wurde, dass sie funktionell relevant ist.

Die in dieser Dissertation präsentierten Ergebnisse offenbaren zwei $Ca_v\beta$ Protein-Protein Schnittstellen, die den Funktionsstatus und die Verfügbarkeit von VGCC an der Plasmamembran regulieren. Somit stehen neue Kontaktoberflächen für die

Medikamentensuche zur Verfügung, um gezielt Kanalfunktionsstörung bei VGCC-assoziierten Krankheiten behandeln zu können. Darüber hinaus deuten diese Ergebnisse auf ein Modell hin, in dem sich $Ca_v\beta$/F-Actin und $Ca_v\beta$/$Ca_v\beta$ Wechselwirkungen gegenseitig ausschließen, was eine strukturelle Grundlage dafür liefert, warum beide Wechselwirkungen unterschiedliche funktionelle Auswirkungen auf die Verfügbarkeit der VGCC-Membran haben.

Chapter 1. Introduction

Calcium is one of the most important second messengers in cells, being involved in many important cellular processes such as gene expression, muscle contraction, enzyme regulation, hormones secretion and synaptic transmission[1]. Adaptation is a constant in life, and calcium signalling provides that flexibility needed for the cells to cope with stimuli and consequently respond. Thus, the conservation of calcium signalling across living beings gives us a clue on the importance that this divalent cation has had in the evolution of life.

When looking carefully into calcium chemical nature, one can find several features that have placed this ion in this key cellular roles. First, the divalent state of calcium enables the formation of more stable complexes with other partners than a monovalent ion could do. Second, the larger radius and more complex electron configuration make it more suitable for fitting in coordination sites, very common in biological macromolecules like proteins. Third, proteins usually form pockets which suit better calcium size rather than smaller ions. Finally, it is remarkable the ability of charged molecules such as calcium to introduce changes in local electrostatic fields in proteins, favouring changes between protein states[1,2]. In conclusion, calcium possesses several chemical characteristics that made it very suitable for intervening in cellular life.

Unlike many other cellular regulators, calcium cannot be synthesized or degraded by the cell itself. This fact drove cells to take advantage of calcium through its compartmentalization in different organelles, such as the endoplasmic reticulum (ER) or mitochondria. Under resting conditions, the intracellular calcium concentration ($[Ca^{2+}]_i$) is maintained at low levels (approximately 100 nM), but upon activation, $[Ca^{2+}]_i$ reaches millimolar concentrations by its release from subcellular compartments. Consequently, a great variety of vital processes are triggered in the cell[3].

The main pathway that calcium uses to enter excitable cells from the extracellular environment is through voltage-gated calcium channels (VGCCs). There is also a wide range of intracellular calcium channels which help maintain proper cytosolic calcium levels, such as the Ca^{2+}-ATPases[4] or IP_3 receptors (IP_3R)[5]; however, for the purpose of this thesis, I will focus now on VGCCs.

1.1 Voltage-gated calcium channels

VGCCs are large protein complexes located in the membrane of multiple excitable cells that activate in response to a depolarization of the membrane potential and passively introduce calcium into the cell. Oscillations in calcium cytosolic concentration are used by the cell to trigger signal transduction and control in-cell processes, being VGCCs the coupling element between the electrical activity and the intracellular processes[6,7]. According to their sensitivity to membrane depolarization, VGCCs were divided in two different classes: low voltage-activated calcium channels (LVACC), which are activated under not very intense depolarizations and high voltage-activated calcium channels (HVACC), which activate under higher depolarizations signals. According to their pharmacological and biophysical properties, VGCCs can be also classified into L-, N-, P/Q- and R-type[7,8].

The first characterisation of the VGCCs composition was carried out by Curtis and Catterall (1984), which led to the discovery of VGCC multimers from skeletal muscle[9]. Further studies have established that VGCCs are composed of five subunits, named α_1, α_2, β, γ and δ[10]. Out of those, it was shown that subunits α_2 and δ are covalently bound forming the $Ca_v\alpha_2\delta$ subunit. Regarding the γ subunit ($Ca_v\gamma$), although the γ_1 variant was copurified with skeletal-muscle calcium channels and recent data shows that this subunit may not be part of neuronal calcium channels, some effects on VGCCs (such as reduction on currents) have been observed. Thus, the γ subunit is now seen as a broader regulator involving other families of proteins such as the AMPA-type glutamate receptors rather than a specific component of VGCCs[11]. The only subunit which was found to be intracellular was the β subunit ($Ca_v\beta$), a globular protein that has very significant roles on VGCCs, such as promoting the channels trafficking to the plasma membrane and controlling the VGCCs biophysical properties[12]. Finally, because of its sensitivity to 3H-dihydropyridine (DHP), the α_1 subunit ($Ca_v\alpha_1$) was identified as the pore-forming subunit. The α_1 subunit is the principal component of VGCCs, responsible for their specific properties[7] and together with the $Ca_v\beta$, forms the core of the HVACC.

In 2016, the determination of the structure of the voltage-gated calcium channel $Ca_v1.1$ by Wu et al. (2016) became a milestone in the VGCCs research field[13]. A description of not only of the VGCC overall structure, but also of the α_1 mechanistic pathway or the inherent interactions between all the subunits was provided by this study (Figure 1.1).

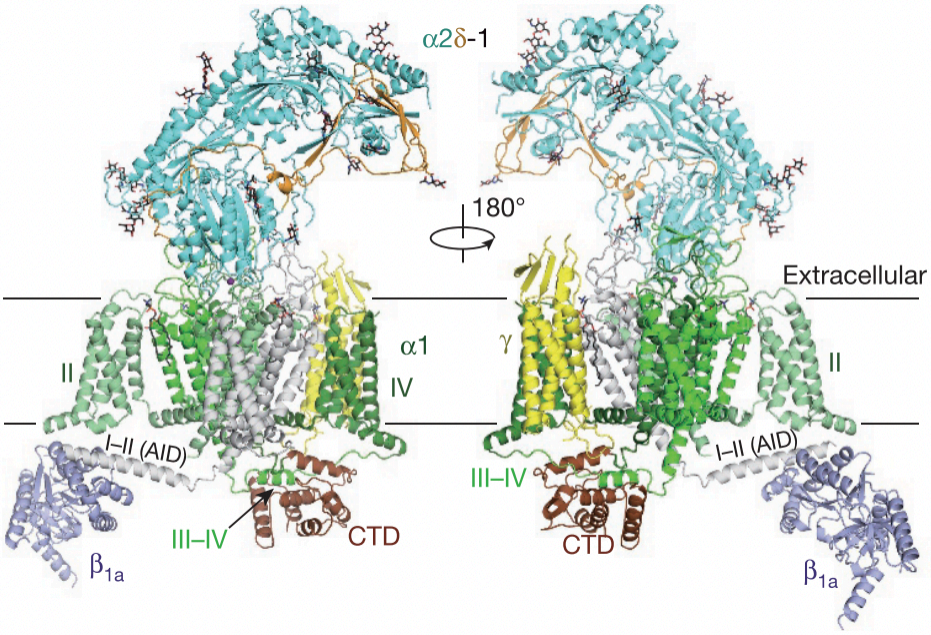

Figure 1.1. Structure of the $Ca_v1.1$ complex. The figure presents the 3.6 Å resolution structure of the calcium channel $Ca_v1.1$ resolved by cryoelectron microscopy (PDB 5GJV) with the different subunits colored in green (α_1), light purple (β), yellow (γ) and cyan ($\alpha_2\delta$). Although belonging to $Ca_v\alpha_1$, the α_1 interaction domain (AID) is colored in grey while the α_1 carboxyterminal domain (CTD) in brown. The four $Ca_v\alpha_1$ domains are indicated in numerals I-IV. Glycosyl and lipids moieties are shown as sticks. Image taken from Wu et al. (2016)[13].

1.1.1 The α_1 subunit

The α_1 pore-forming subunit is a 190- to 250-kDa integral membrane protein and the main component of the VGCCs. Located at the heart of the complex structure, it contains all the elements that characterise a VGCC, such as the voltage-sensitive region, the permeation pathway, the selectivity filter and binding sites for drugs. Its topology consists of four daisy-chained main domains (named I-IV) connected by three cytosolic loops (named I-II, II-III and III-IV, depending on the domain that they are connecting) flanked by the N- and C- intracellular termini (Figure 1.2). Each intracellular domain comprises six transmembrane α-helixes (S1-S6) grouped in two different functional domains: the voltage-sensing domain (VSD) formed by the helixes S1 to S4 and the pore domain (PD) formed by the helixes S5 to S6[14].

The cytosolic loops contain several protein-protein interaction sites that are used for the channel modulation. For instance, the so-called α_1 interaction domain (AID) is a consensus sequence of approximately fifteen amino acids located in the I-II cytosolic loop which the β subunit binds.

The C-terminus is also of importance because it bears the binding site for Ca^{2+}/calmodulin (IQ)[14].

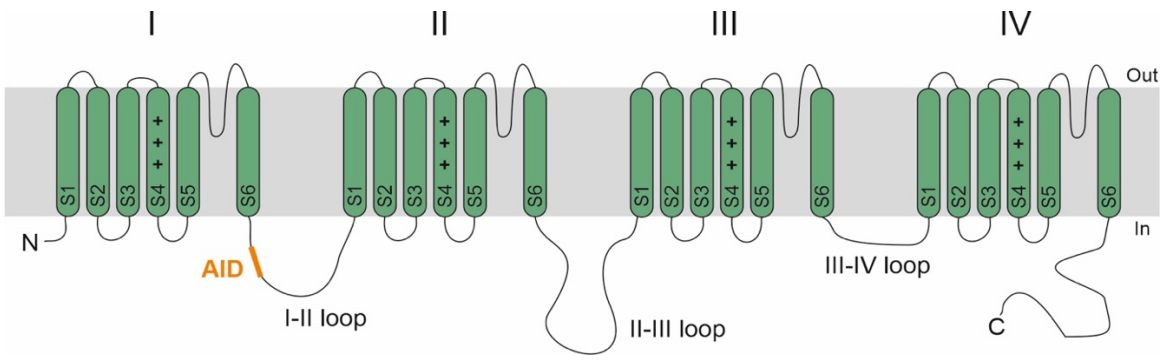

Figure 1.2. Membrane topology of $Ca_v\alpha_1$ subunit. The α_1 subunit consists of four domains (I-IV), each with six transmembrane helixes (S1-S6), connected by three intracellular loops. The S4 contains the positively charged voltage sensor (indicated here with '+'). The binding domain of $Ca_v\beta$s the AID, is highlighted in orange at the loop between S6 and S1 of domains I and II, respectively. Image adapted from Buraei et al (2010)[12].

The ten $Ca_v\alpha_1$ protein subtypes (encoded by the genes CACNA1A-I and CACNA1S) have been grouped in three different protein families according to their amino acids sequence identity: Ca_v1, Ca_v2 and Ca_v3 (Figure 1.3). Both Ca_v1 and Ca_v2 members are HVACC, but the four Ca_v1s ($Ca_v1.1$-4) are L-type channels, whereas the three Ca_v2s ($Ca_v2.1$-3) are P/Q-, N- and R-type respectively. The third group, Ca_v3, consists of the three LVACC channels ($Ca_v3.1$-3), which are characterised by T-type currents and by not being associated with any auxiliary subunits[15,16].

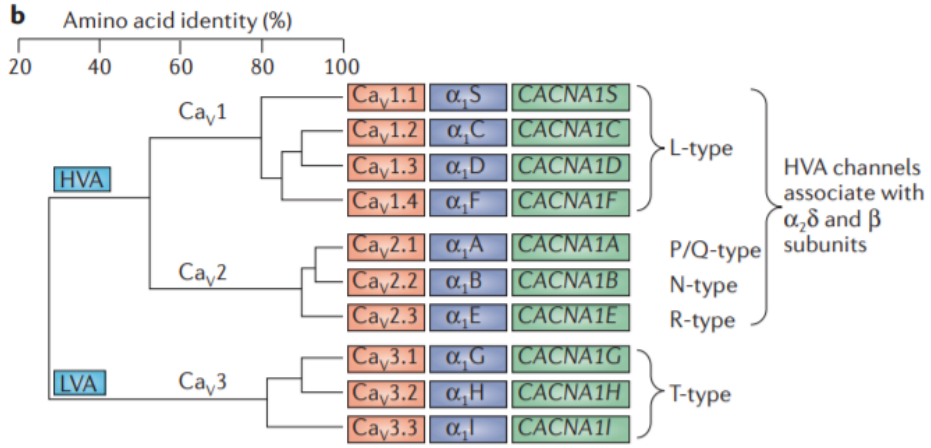

Figure 1.3. $Ca_v\alpha_1$ subunit family classification. $Ca_v\alpha_1$ can be divided into three major families (Ca_v1-3) according to its sequence identity. Ca_v1 and Ca_v2 families are also grouped as high-

voltage-activated (HVA) channels and can bind $\alpha_2\delta$ and β subunits, while Ca_v3 forms the group of low-voltage-activated (LVA) channels. Figure taken from Dolphin (2012)[17].

1.1.2 The β subunit

The β subunit of the VGCCs ($Ca_v\beta$) was first described as part of the discovery of VGCCs by Curtis and Catterall (1987), while it was first cloned two years later by Ruth et al (1989)[9,18]. $Ca_v\beta$ is a protein encoded by 4 different genes (CACNB1-4) with a MW ranging from 50-70 kDa. After the alternative splicing that the four isoforms can undergo, the number of $Ca_v\beta$s substantially increases up to more than 20 different proteins[10,12]. In general, all $Ca_v\beta$s isoforms are expressed preferentially in the brain, but also in other specific tissues. The main tissues where $Ca_v\beta$s are expressed are heart, skeletal muscle or spleen for $Ca_v\beta_1$; heart, adrenal gland and lung for $Ca_v\beta_2$; heart, endometrium and skeletal and smooth muscle for $Ca_v\beta_3$; kidney, skeletal muscle and very intensively in cerebellum for $Ca_v\beta_4$. Last but not least, it is remarkable that some splicing variants increase (β_{1b}, β_4) or decrease (β_{2c}, β_{2d}, β_{2e}) during the the development[12,19]. Altogether, the massive number of $Ca_v\beta$ variants are regulated not only at the tissue but also at the developmental level, which along with the variety of $Ca_v\alpha_1$, highlights the multidiversity in function of HVACCs.

The first structures of $Ca_v\beta$ were released in 2004 by three independent groups[20–22]. Those structures corresponded to a $Ca_v\beta_{2a}$, $Ca_v\beta_3$ and $Ca_v\beta_4$ respectively, and confirmed prior assumptions that the $Ca_v\beta$s contained an Src homology 3 (SH3) domain and a guanylate kinase (GK) domain. These two domains were connected by a linker called HOOK. Altogether, the SH3-GK module is known as the core of $Ca_v\beta$s[12].

In a more general sense, $Ca_v\beta$s belong to the superfamily of proteins called membrane-associated guanylate kinases (MAGUKs). MAGUKs are proteins with a large variety of functions but mainly involved in signal transduction and cell-cell communication[23]. Their common structure is formed by the SH3-HOOK-GK module plus several tandem PDZ (PSD-95/DLG/ZO-1) domains, which are one of the most ubiquitous protein-protein interaction domains in nature. Interestingly, $Ca_v\beta$s are the only MAGUK member that lacks PDZ domains.

The SH3 and GK domains of MAGUKs form a compact structure where the last two beta strands of the SH3 domain (βE and βF) are separated of the previous βD strand by the insertion of the HOOK (Figure 1.4). This special arrangement where the HOOK occludes the canonical

SH3 target binding site, was often used as an argument to explain why the SH3 domain of some MAGUK does not bind to proline-rich sequences[23,24]. However, several later articles have described SH3 of other MAGUK binding to proline-rich sequences[25,26], which would entail important conformational change forcing the target binding site exposure.

On the other hand, the MAGUKs' GK domain evolved from the enzyme guanylate kinase, which catalyzes a phosphoryl transfer from adenosine triphosphate (ATP) to guanosine monophosphate (GMP)[27]. In the case of MAGUKs and more specifically in the $Ca_v\beta$s, the guanylate kinase activity of the GK domain was lost during evolution. Moreover, $Ca_v\beta$s cannot bind either ATP, GMP or phospho-peptides. Instead, the GK domain seems to have evolved as a protein binding module[23,28].

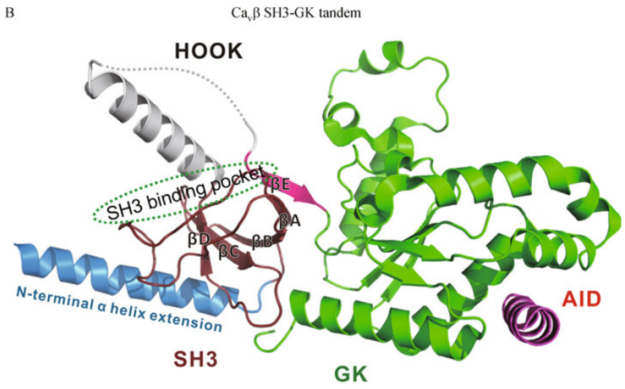

Figure 1.4. Molecular structure of $Ca_v\beta$. $Ca_v\beta$s are proteins consisting of two main domains, a SH3 domain (brown) and a GK domain (green) connected by a region called HOOK (grey). The α_1 interaction domain (AID) (pink) binds to a groove located in the GK domain. Image taken from Buraei et al. (2010)[12].

In conclusion, $Ca_v\beta$s possess some interesting structural characteristics that have been fine-tuned during evolution and explain its function as an important player in protein-protein interactions (PPI). Furthermore, some disease-causing mutations in $Ca_v\beta$s produce phenotypes that cannot be explained by altered biophysical properties of VGCC, which motivate the study of $Ca_v\beta$ PPI.

1.2 $Ca_v\beta$ interactors

Multiple functions have been described for $Ca_v\beta$s, which essentially depend on the $Ca_v\alpha_1$/$Ca_v\beta$ binding reversibility and its numerous interactors[12,19]. For instance, $Ca_v\beta$ interaction

with ryanodine receptors (RyR) in skeletal muscle seems to be indispensable for the 'excitation-contraction' (EC) coupling and $Ca_v\alpha_1$/RyR assembly[29]. The interaction with RGK GTPases reduces $Ca_v\beta$ availability for $Ca_v\alpha_1$ binding, decreasing HVACC membrane targeting[12]. Furthermore, dimerization of $Ca_v\beta$s and its binding to dynamin seem to have a crucial role on HVACC endocytic internalization[30,31]. Also, $Ca_v\beta$ interaction with RIM1 and synaptotagmin has a structural role on the synaptic vesicle releasing machinery. Lastly B56/PP2A complex interaction with $Ca_v\beta$ was described to be responsible for $Ca_v\beta_4$ nuclear targeting and its role on gene regulation in the nucleus[32]. Many other putative $Ca_v\beta$ interactors have been proposed in a recent proteomic study[33], but for the purpose of the thesis, I will focus on three $Ca_v\beta$ interactors: $Ca_v\alpha_1$, F-actin and $Ca_v\beta$.

1.2.1 $Ca_v\beta$/$Ca_v\alpha_1$ interaction

$Ca_v\beta$ binds with nanomolar affinity to $Ca_v\alpha_1$ at the intracellular loop located between the helixes S6 and S1 of the domains I and II respectively (Figure 1.2). This region, named as α_1 interaction domain (AID), encompasses a consensus motif (QQxExxLxGYxxWIxxxE) for all Ca_v1 and Ca_v2. On the other hand, AID binds to a hydrophobic groove located in the GK domain of $Ca_v\beta$ named as AID-binding pocket (Figure 1.4).

$Ca_v\beta$ is the most prominent interactor of $Ca_v\alpha_1$ and its role as its auxiliary subunit is crucial for a normal Ca_v function. For instance, $Ca_v\beta$/$Ca_v\alpha_1$ interaction has been proven *condicio sine qua non* for Ca_v plasma membrane targeting[12]. Two main hypotheses have been proposed for explaining the enhancement of Ca_v membrane targeting by $Ca_v\beta$: 1) $Ca_v\beta$ occludes endoplasmic reticulum (ER) retention signals on $Ca_v\alpha_1$[34,35], 2) $Ca_v\beta$ prevents $Ca_v\alpha_1$ from ubiquitination and proteosomal degradation[36].

$Ca_v\beta$ interaction with $Ca_v\alpha_1$ is also known to intensively modulate Ca_v1 and Ca_v2 biophysical properties. The gating properties of $Ca_v\alpha_1$, voltage dependence of activation (VDA), voltage dependence of inactivation (VDI) and kinetics are changed upon $Ca_v\beta$ binding. $Ca_v\beta$s shift VDA to more hyperpolarised voltages, allowing $Ca_v\alpha_1$ activation at lower voltages[37,38]. Moreover, $Ca_v\beta$s increase the maximum open probability of the $Ca_v\alpha_1$ and its insertion into the plasma membrane[39,40]. Altogether, $Ca_v\beta$ modulation over Ca_vs results in an increased calcium current density.

1.2.2 $Ca_v\beta$/F-actin interaction

Actin is the most abundant protein in cells, accounting for more than a 10% of the cell total weight. Moreover, it is a ubiquitous protein found in the vast majority of living beings showing an extraordinary conservation, which highlights its important roles for life[41].

Actin is a protein of approximately 375 amino acids which adopts a flat and quadrangular quaternary structure with a small cleft in the centre for ATP binding (Figure 1.5A-B). It can be divided in four subdomains (SD) with the N- and C-termini located in the subdomain 1. Actin can exist in two different main forms: globular and monomeric (G-actin, Figure 1.5A-B) or filamentous and polymeric (F-actin, Figure 1.5C-D)[41,42].

F-actin polymerisation depends on ATP hydrolysis. Briefly, new monomeric (ATP-bound) actin molecules assemble with other actin molecules with the help of nucleating factors upon ATP consumption. This produces a quasi-stable ADP-P_i/F-actin complex that persists till phosphate release, resulting in a final ADP-bound F-actin state. F-actin polymerisation occurs in both directions from the same seed but being much faster at the barbed end than at the pointed end (Figure 1.5C). This gives rise to a polarised helical double-stranded filament (Figure 1.5D)[41,43].

F-actin polymerisation and depolymerisation is a very fast and highly dynamic process characterised by the intervention of actin binding proteins (ABP). This regulation is crucial for the F-actin multifarious functions in cells. F-actin is involved in defining cellular shape, cell-cell and cell-matrix interactions, trafficking machinery, cytokinesis and determination of cell polarity[43,44]. Recent evidence indicates that both monomeric and filamentous actin are also present in the cell nucleus, where they are involved in the maintenance of nuclear architecture, stability, repair of double-stranded breaks (DSBs) or gene expression[45–48].

Actin is also one of the most recently identified interactors of $Ca_v\beta$. Stölting et al. (2015) first demonstrated with *in vitro* and *in vivo* experiments that $Ca_v\beta_2$ can interact with F-actin[49]. This interaction is mediated by both SH3 and GK domains of $Ca_v\beta$, as demonstrated by actin co-sedimentation assays. Moreover, fluorescence resonance energy transfer (FRET) between $Ca_v\beta$ and F-actin was observed in HeLa cells, further supporting the proximity of the two proteins in the cellular context. Interestingly, overexpression of $Ca_v\beta_2$ in HL-1 cells (a murine atrial cardiomyocyte cell line) increased L-type currents without altering the voltage dependency.

This upregulation is abolished after disrupting actin filaments with cytochalasin-D, suggesting that $Ca_v\beta_2$/F-actin interaction controls calcium channel insertion in cardiomyocytes.

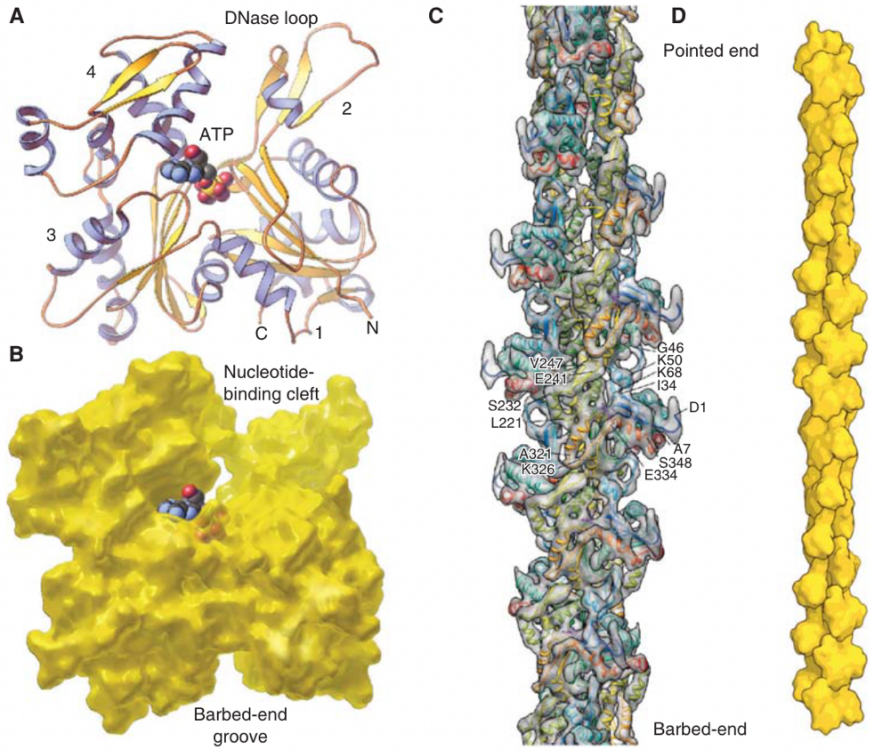

Figure 1.5. Structure of globular (G-) and filamentous (F-) actin. Actin possesses a clear globular structure with four main subdomains. The ATP nucleotide binds in a cleft between subdomains four and two. Upon ATP consumption, actin can polymerise into large filaments forming a double-stranded helix. Image taken from Pollard (2016)[41].

$Ca_v\beta_{4b}$ was also found to interact with F-actin and enhance spontaneous and evoked postsynaptic currents, as well as the size of ready-realisable pool (RRP) of synaptic vesicles (SVs) and its recovery after depletion in hippocampal neurons[50]. The enhanced synaptic transmission function of $Ca_v\beta_{4b}$ is dependent on intact actin filaments, as the disruption with cythocalasin-D abolishes it. Interestingly, a $Ca_v\beta_{4b}$ mutant with an impaired association to calcium channels retains the ability to increase the RRP size, suggesting that this $Ca_v\beta$ function is channel independent.

In summary, $Ca_v\beta$/F-actin interaction has been demonstrated in different physiological systems with different functions: while in cardiomyocytes it enhances L-type currents, in hippocampal neurons it regulates the size of RRP[51,52]. $Ca_v\beta$ interaction with F-actin is versatile and dependent

on the cellular context. However, the lack of structural data on the $Ca_v\beta$/F-actin complex still hampers our understanding of its multifarious roles in physiology and pathophysiology.

1.2.3 $Ca_v\beta$/$Ca_v\beta$ interaction

Several pieces of evidence have emerged that suggest that $Ca_v\beta$s can form oligomers. For example, $Ca_v\beta$ oligomerization seems to occur in intact vascular smooth muscle cells[53]. Interestingly, a previous study showed size-exclusion chromatography (SEC) profiles of $Ca_v\beta_{1b}$ compatible with $Ca_v\beta$ dimerization[39]. Also, $Ca_v\beta$s were shown to interact in a yeast-two hybrid assay; such results indicated that the SH3 domain of one $Ca_v\beta$ may interact with the GK domain of the other $Ca_v\beta$[54]. Moreover, it has been proved that isolated SH3 domains of $Ca_v\beta_2$ can dimerize[31]. Such interaction is fully dependent on a unique disulphide bond formed between the sole Cys residue present in $Ca_v\beta$s SH3 domain and was shown to promote dynamin-dependent endocytosis of $Ca_v1.2$. In the same study, $Ca_v\beta$ dimerization was demonstrated in cells by FRET. Interestingly, FRET efficiency between recombinantly expressed and purified $Ca_v\beta_2$s was decreased after incubation with the AID peptide. Such results suggest that $Ca_v\beta$ dimerization and $Ca_v\beta$/$Ca_v\alpha_1$ interaction are mutually exclusive processes.

Other members of the MAGUKs superfamily have been shown to form oligomers. One of the most studied ones is the MPP5-PSG protein. Like other MAGUKs, MPP5-PSG can form target-dependent oligomers. In this case, its binding with the cytoplasmic tail of crumbs (CRB-CT), a 37-residue tail of the CRB transmembrane protein, gives rise to a domain-swapped dimer where the GK domain of one chain interact with the SH3 of the other one and vice versa[28,55]. In this target dimer configuration, CRB-CT is hold by both SH3 and PDZ domains of the same chain. Although the PDZ domain do not participate in the dimeric interface and some features of the MPP5-PSG protein complex could fit with the one described for $Ca_v\beta$s, a direct comparison between $Ca_v\beta$s and other MAGUKs dimerization modes must be taken with caution.

In essence, whereas some functional roles of $Ca_v\beta$ dimerization are known, structural data are needed to have a deeper understanding the aforementioned pieces of evidence and the implications of $Ca_v\beta$ dimerization at the cellular level.

1.3 Aim of the dissertation

The capability of $Ca_v\beta$ to interact with diverse intracellular partners confers upon it the attribute of a multiregulatory protein modulating functions that impact calcium channel activity. To have a deeper understanding of the functional diversity of $Ca_v\beta$s, structural data defining the different $Ca_v\beta$ PPI are needed.

The study of the plethora of $Ca_v\beta$ interactors emerges as an attractive research field for understanding the physiological and pathophysiological roles of $Ca_v\beta$ in the previously mentioned cellular processes. Among those interactors, F-actin and $Ca_v\beta$ (via dimerization), can regulate the forward trafficking and endocytic recycling of Ca_vs respectively, resulting in an alteration of the channel function independent of its association status with Ca_vs[30,31,49,51,52].

However, the lack of structural data on these complexes hampers the understanding of the precise role of $Ca_v\beta$s on Ca_v cell surface availability and therefore, on the physiological processes reliant on it. A more detailed comprehension of $Ca_v\beta$/F-actin and $Ca_v\beta$/$Ca_v\beta$ interactions will support the rationally targeting of Ca_v-associated dysfunctions. The goal of my thesis was to study structurally both interactions by means of cross-linking mass spectrometry (XL-MS) and protein-protein docking to design rationally mutants with decreased affinity that will be validated by *in vitro* and *in cellulo* assays. Such structural characterisation will set the basis for discerning $Ca_v\beta$/F-actin and $Ca_v\beta$/$Ca_v\beta$ interactions roles *in vivo*.

Chapter 2. Methodologies

2.1 Mass spectrometry (MS)

Mass spectrometry (MS) is a technique that allows the determination of the mass-to-charge (m/z) ratio of analytes in a gas phase. In a typical proteomics applied MS workflow, a protein sample is previously denatured and digested by proteases (e.g. trypsin, gluC, chymotrypsin). The complex peptide mix is further separated by nano high-performance liquid chromatography (nano-HPLC) to reduce the complexity of the analytes injected at a single time in a mass spectrometer[56].

Mass spectrometers have three main components (Figure 2.1):

1. Ionization source. Analytes ionization is thought to introduce charges in the analytes to decrease the m/z ratio and facilitate its detection. Two main ionization techniques are used nowadays: electrospray ionization (ESI) and matrix-assisted laser desorption/ionization (MALDI). The following explanations will apply mainly to ESI. The ionization process occurs in two separate steps: first, analytes are volatilised and then ionised. Sample volatilization is achieved by passing the solution through a small capillary at a very high voltage (4kV) at atmospheric pressure. Then, the formed droplets containing charged analytes are converted to gas phase. Such process occurs as the organic solvent present in the droplets evaporates increasing charge density. When the coulombic repulsion between charged particles overcomes the surface tension, the small droplets undergo fission and form a gaseous phase[57,58].
2. Mass analyzer. Mass analyzers resolve ions based on its m/z ratio. There are five main types of analyzers that can in turn be divided in two major groups: beam-based and trapping analyzers [57]. The three main analyzers are briefly described below:

    a. Time of flight (ToF). In ToF analyzers, ions are initially accelerated with a fixed potential through a tube and the mass is determined from the velocity (kinetic energy) that they possess when reaching the detector.
    b. Quadrupole. A quadrupole analyzer is formed by four cylinders parallel to each other. Mass separation results here from the dynamic motion of an ion in an

oscillating electrical field. Quadrupoles can be used as mass filters by adjusting the electrical potential applied.

c. Orbitrap. Orbitraps are trapping analyzers where the ions are kept and rotated between an inner and outer electrode. The oscillating frequency of an ion when an electric potential is applied is proportional to its m/z value.

3. Detector. Detectors in mass spectrometers are typically electron multipliers (EM).

In tandem mass spectrometry mode (MS/MS), after the initial mass determination, specific ions are selected and subjected to fragmentation through collision dissociation, which allows the mass determination of its components. Normally, in tandem MS a quadrupole analyzer is firstly used to determine the mass of the peptides (MS1), while a second fragmentation is implemented to acquire the masses of its components (MS2). Specifically designed software can determine then the peptide sequence from its MS2 spectra[57].

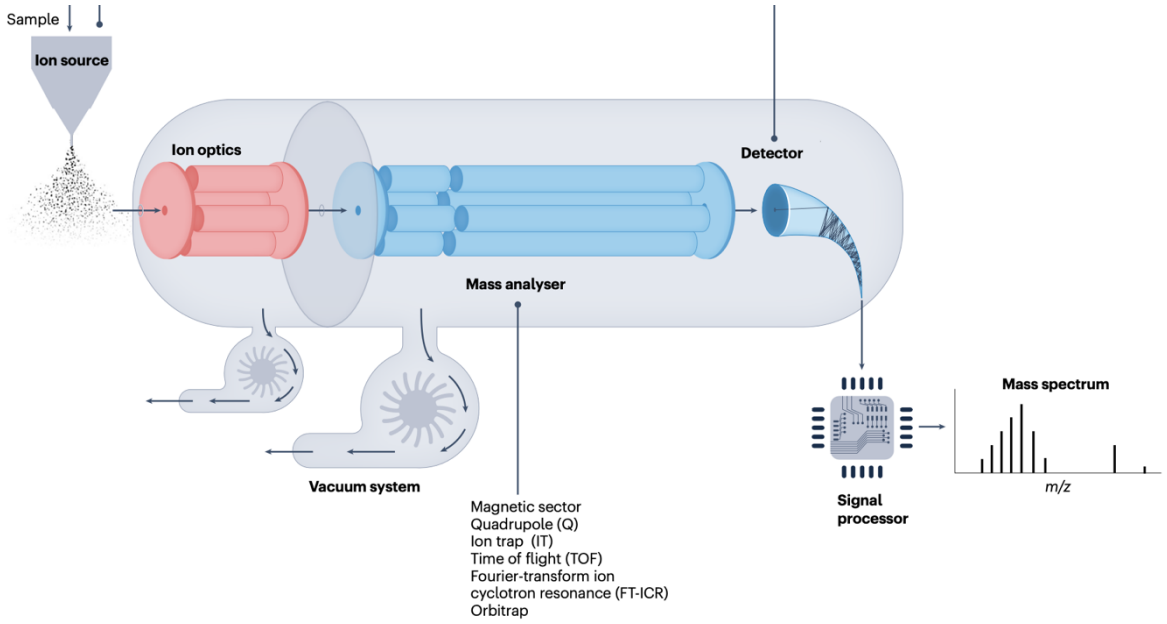

Figure 2.1. Functional components of a mass spectrometer. Mass spectrometers are composed of three main units: an ionization source, that is responsible for the volatilization and ionization of analytes, a mass analyzer, that resolves analytes m/z values according to physical estimations and a detector. Image taken from Prabhu et al. (2023)[58].

2.2 Cross-linking mass spectrometry (XL-MS)

Cross-linking mass spectrometry (XL-MS) is a robust technique that has been used to gain structural insight on protein networks or protein complexes that are not amenable for the most common structural determination techniques, that are nuclear magnetic resonance (NMR), X-ray crystallography and cryo-electron microscopy (cryo-EM). XL-MS is thought as an integrative process that starts with the introduction of covalent links between proximal residues in protein complexes using a cross-linker and follows with the identification of the cross-linked residues by MS. More specifically, if a specific protein interaction is to be studied, the position of the identified residues together with the cross-linker length can be used to define spatial constraints and dock the two proteins forming the complex with computational methods or study conformational changes of proteins[59,60].

Cross-linkers have two defined functional parts: the reactive group and the spacer (Figure 2.2):

a) The reactive group, located at both edges, determines the specificity of the cross-linker for certain functional groups on amino acids. The most commonly used cross-linkers, such as disuccinimidyl suberate (DSS), disuccinimidyl dibutyric urea (DSBU or BuUrBu) or disuccinimidyl sulfoxide (DSSO), contain a N-hydroxysuccinimidyl (NHS) ester as reactive group. This group reacts mainly with lysines (but also with serine, threonine and tyrosine to a lesser extent) and their use is widely extended because of the overall presence of lysine as a solvent accessible residue in proteins[59]. Residues such as aspartic and glutamic acid have also been targeted by specific acidic crosslinkers like 1-ethyl-3-(3-dimethylaminopropyl) carbodiimide hydrochloride (EDC). The targeting of acidic residues was recently improved by using the amine-based cross-linker dihydrazide sulfoxide (DHSO) in combination with the carboxyl activator 4-(4,6-dimethoxy-1,3,5-triazin-2-yl)-4-methyl-morpholinium chloride (DMTMM), which allowed the cross-linking of acidic residues at neutral pH[61].

   The use of photoreactive diazirine-consisting cross-linkers has made more amenable the study of solvent-inaccessible hydrophobic protein-protein interfaces which cannot be so easily studied by the previous mentioned cross-linkers[62].

b) The spacer determines the distance between the amino acids that can be cross-linked and has an influence on the data density and the spatial information derived. The use of different spacers must be considered depending on the information to be acquired. For instance, longer spacers are suitable for studying qualitatively a protein network, but it brings more ambiguity for structural modelling as the degrees of combinations that would fulfil the restraint increase[59,60].

Cross-linked peptides are always found in sub-stochiometric concentrations compared to the non-cross-linked species. Therefore, the incorporation of enrichable functional groups such as biotin (in the so-called protein interaction-reporters (PIRs) cross-linkers) or isotope-labeled atoms (by improving the identification of the cross-linked precursor) have brought major advances. Among them, the use of cleavable groups in the spacer significantly improved the unambiguous detection of cross-links[63].

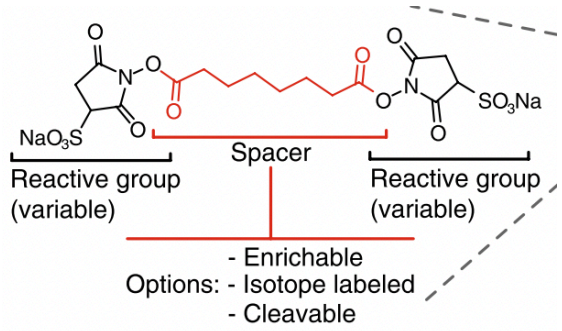

Figure 2.2. Components of a cross-linker. Cross-linkers have two main functional parts: a reactive group that is located at both edges and react with target amino acids and a spacer, which can be modified to be enrichable or isotope labeled or to contain cleavable groups that improve cross-link detection. Image taken from O´Reilly et al. (2018)[60].

As mentioned above, the incorporation the MS-cleavable groups in the spacer of cross-linkers transformed the field. Such groups carry labile bonds that can be cleaved under collisional activation in the MS. This lability has several consequences. First, by allowing a separate fragmentation of the cross-linked peptides, it solves the cofragmentation efficiency problem[64]. Second, the fragmentation of two inter-connected peptides to two separated peptides reduces the combinatorial search space from n^2 to 2n in data analysis. Finally, MS-cleavable cross-linkers can fragment creating characteristic doublet ion patterns, whose identification reduces the rate false-positive assignments. Some common groups found in MS-cleavable cross-linkers

are the urea group, present in DSBU and N,N'-Carbonyldiimidazole (CDI), or the sulfoxide group, present in DSSO and DHSO, each with a characteristic ion pattern (Figure 2.3).

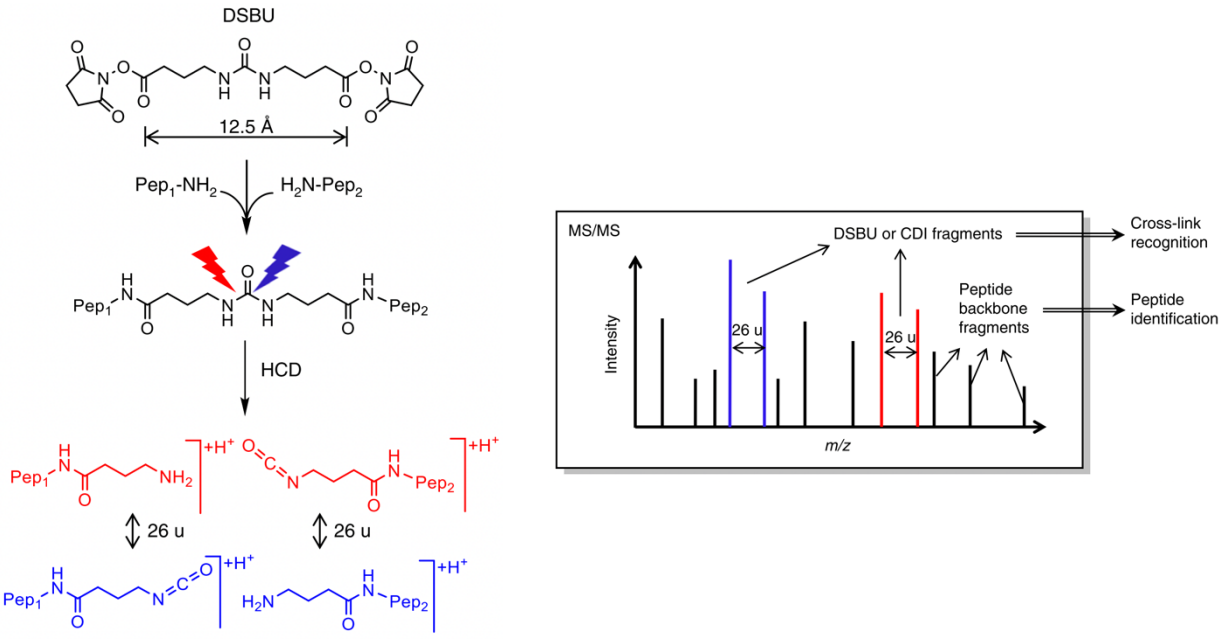

Figure 2.3. Characteristic fragmentation pattern of MS-cleavable cross-linkers. Labile groups located inside the spacer of MS-cleavable cross-linkers fragment upon induced collision creating ion pairs with a characteristic difference in mass. This typical pattern allows a unambiguous identification of the cross-linked peptides. Image taken from Iacobucci et al. (2018)[65].

A cross-linking reaction yields three types of cross-linked products: 1) dead-end or type 0, which are peptides bound to a partially hydrolyzed crosslinker; 2) intra-peptide or type 1, when the cross-linked amino acids belong to the same peptide; and 3) inter-peptide or type 3, when the cross-linked amino acids are part of different peptides. While dead-end cross-links can provide information about the solvent accessibility of a protein and intra-peptide are useful for modeling protein three-dimensional structures, inter-peptide cross-links provide the most valuable information for guiding protein-protein dockings of protein complexes[59,60,64,65].

2.2.1 Software for XL-MS

Table 2.1. Software used for XL-MS analysis.

Software	Use	Reference	URL
msConvertGUI	Conversion of MS raw data	[66]	https://proteowizard.sourceforge.io/projects.html
MaxQuant /MaxLynx	Analysis of large mass-spectrometric data sets / Analysis of MS data for cross-links identification	[67,68]	https://www.maxquant.org
MetaMorpheus	Analysis of MS data for cross-links identification	[69]	https://smith.chem.wisc.edu/content/software
MeroX	Analysis of MS data for cross-links identification	[65]	http://stavrox.com
SIM-XL	Analysis of MS data for cross-links identification	[70]	http://patternlabforproteomics.org/sim-xl/

2.3 XL-MS guided protein-protein docking

Computational docking is a technique to predict the three-dimensional structure of a complex starting from the individual structures. Although docking can also be used to predict the structure of a protein-ligand and protein-nucleic acid complexes, here I will focus on protein-protein docking. Computational docking approachess can be classified as *ab initio*, when the docking only considers the atomic coordinates of the partners, or data-driven, when existing experimental or predicted data is implemented in the protocol to drive the docking[71]. In this thesis I applied the latter approach, in particular using XL-MS data as distance restraints.

One of the computational pipelines allowing to derive integrative, data-driven models is the High Ambiguity Driven biomolecular DOCKing (HADDOCK). An important aspect of HADDOCK is that it can accept experimental (e.g: NMR, site-directed mutagenesis or XL-MS) or computationally predicted data, incorporate them as restraints to guide the docking search and, together with statistical and physical potentials, to score, rank the resulting solutions and produce high quality docked structures[71–74].

2.3.1 Distance restraints

The definition of distance restraints is intended to force groups of atoms to be at a specific distance from each other and that way increase the sampling of conformations compatible with the previously generated experimental data (e.g. cross-linking or mutagenesis data). HADDOCK allows to define two type of distance restraints, i.e. unambiguous and ambiguous restraints, depending on their characteristics, reliability and the ability to define a discrete pairwise atom distance[71,75].

2.3.1.1 Unambiguous restraints

Highly reliable inter-peptide cross-links identified by MS can be used to define unambiguous restraints by setting a specific distance range between the cross-linked residues according to the cross-linker length and type of the cross-linked amino acids. The restraint is usually set between the two alpha carbons (C_α) of the cross-linked amino acids since they are present in every amino acid and tend to have a smaller degree of flexibility. The distance range is specified by three numbers: the target distance (d^0), the lower margin (d^-) and the upper margin (d^+) and defined by subtraction or addition of the lower or upper margins to the target distance respectively[72,75,76].

To clarify this point, we can take a putative example of a protein called *A* and another called *B* that were cross-linked with DSBU. After MS analysis the cross-linked residues *a* and *b* were identified. The distance range for defining an unambiguous distance restraint must account for the cross-linker spacer length (12.5 Å for DSBU), the cross-linked amino acids side chain length (2 x 8 Å, for lysines) and a certain flexibility. Altogether, a distance range of 30 Å between the C_α of *a* and *b* can be used. Then, a range of 0-30 Å can be defined with a target distance d^0 = 30 Å, a lower margin d^- = 30 Å and an upper margin d^+ = 0 Å, so that $d^0 - d^-$ = 0 Å and $d^0 + d^+$ = 30 Å.

Unambiguous restraints will be applied in each step of the docking protocol (see section 2.3.4) and the corresponding distance restraining potential takes the form of a flat bottom harmonic potential. While the distance between the defined atoms is within the specified range, the restraint potential energy will remain zero, whereas it transitions to a linear potential after the upper bound to avoid large forces[76].

2.3.1.2 Ambiguous restraints

Experimental data, such as site-directed mutagenesis, or bioinformatic predictions, such as those generated with CPORT (see section 2.3.2), that cannot be defined in a straightforward manner as distance restraints between two discrete atoms are incorporated by HADDOCK in the form of Ambiguous Interaction Restraints (AIRs). AIRs are distance restraints that take the same functional form as unambiguous restraints, but are defined between the so-called active and passive residues[71].

1. Active residues:

Active residues are those which there is experimental evidence of their participation in protein-protein interactions, or in the absence of experimental data, a computational prediction indicating them as protein-protein interfacial residues. In the latter case, such residues must additionally have a solvent accessibility higher than 40% for either the main or side chain[77].

2. Passive residues:

Passive residues are solvent-accessible residues surrounding active residues (around 6.5 Å) that can potentially make additional protein-protein contacts[71].

For every active residue in a given protein, a unique AIR is created between that active residue and all the other active and passive residues in the other protein partner. Typically, a specific AIR is considered satisfied when the defined residue is within 3-4 Å of any other active or passive residue. In this way, the defined residue will be forced to contact a whole surface and not a specific residue, differently from the unambiguous restraints presented in section 2.3.1.1. Therefore, AIRs are useful to indicate protein-protein interfaces without predefining the spatial orientation of the partners[71,72,75].

2.3.2 Prediction of interfacial residues with CPORT

When experimental data on the protein-protein interface is missing or scarce, bioinformatic predictions of interfacial residues can be used to define AIRs to drive the protein-protein docking. Interfacial residue predictions are based on the analysis of different protein features such as its structure, sequence and evolutionary conservation of its residues.

Compared to *ab initio* dockings, integration of experimental data with predictions of interfacial residues has been shown to improve the performance of the docking protocol[78]. For that reason, in this thesis I used the Consensus Prediction Of interface Residues in Transient complexes (CPORT) webserver. CPORT is an algorithm that combines 6 different predictors for protein-protein interface residues and creates a consensus list of active and passive residues that can be used for docking with HADDOCK[78].

2.3.3 Restraints consistency analysis with DisVis

The identification of false-positive inter cross-links is of utmost importance for the success of protein-protein docking. DisVis is a software designed for evaluating data-consistency and information content of distance restraints, in particular cross-linked derived restraints. DisVis performs a full systematic 6-dimensional search of the three translational and rotational degrees of freedom of the two protein partners to determine the number of complexes consistent with the restraints. In addition, it outputs a density calculated as the center-of-mass position of the smallest protein partner with respect to the largest protein partner while fulfilling the highest number of consistent restraints at every position in space. In other words, DisVis calculates the reduction in the accessible interaction space (set of structure poses consistent a given set of distance restraints) when one or more distance restraints are imposed. The accessible interaction space will decrease depending on the information content of the restraint by both checking data consistency and analyzing violations. DisVis allows to discard false positive restraints and generate a filtered restraint set to drive docking[79,80].

When guiding a protein-protein docking with XL-MS data, it is helpful to provide an additional set of AIRs defined from solvent-accessible residues (e.g. calculated by NACCESS) and/or bioinformatic predicted interfacial residues (e.g. by CPORT) that are compatible with the XL-MS data, i.e. are located in the vicinity of the cross-linked residues. The interaction analysis feature of DisVis allows to identify the solvent accessible and/or predicted interfacial residues most contacted in the complexes consistent with the validated inter cross-links. Then, a curated list of active and passive residues complementing the experimental cross-linking data can be generated and used to define AIRs[79–81].

2.3.4 Protein-protein docking with HADDOCK

HADDOCK is a docking method characterized by its ability to incorporate experimental or predicted data in the form of restraints to drive molecular docking. It is based on python scripts derived from ARIA (Ambiguous Restraints for Iterative Assignment) that make use of CNS (Crystallography and NMR System) program[71,82].

The docking protocol of HADDOCK consists of three main steps, each with a different purpose[71,75,82]:

1. Rigid-body energy minimization (it0). In the first step, the topologies of the two protein partners are generated from the input individual structures, which will be treated as rigid bodies, that is, none of their geometrical parameters are modified. The rigid-body energy minimization is carried out by rotating and translating the partners around each other. In this step, complexes are biased to satisfy the defined AIRs.

2. Semi-flexible refinement in torsion angle space (it1). This step is intended to optimize the interface packing of the complexes. Therefore, flexibility is introduced only in those residues located at the protein-protein interface (defined as those residues within 5 Å of the other partner) to optimize their energetics by a three-step molecular-dynamics simulation. First, the partners orientations are optimized; second, the side chains of interfacial residues are allowed to move and finally both backbone and side chains of interfacial residues are considered flexible. Conformational changes might be driven by AIRs in this step.

3. Final refinement in explicit solvent (water). The final step consists of a short molecular dynamics simulation at 300 K in explicit solvent (either water or DMSO) to improve the general energetics of the docked complexes.

After each of the previously mentioned steps, the complexes are scored following the HADDOCK score function and ranked according to such score; only the best ones (by default, 200 out of the initial 1.000) are kept for the following step. The HADDOCK score function (Eq. 2.1) is a sum of weighted components which considers the van der Waals (E_{vdw}),

electrostatic (E_{elec}), desolvation (E_{desol}) and restraint violation (E_{air}) energies along with the buried surface area (BSA; term not included in the final scoring step)[71,82].

$$HADDOCK_{score-water} = 1.0\ E_{vdw} + 0.2\ E_{elec} + 1.0\ E_{desol} + 0.1\ E_{air} \qquad (2.1)$$

2.3.5 Software for XL-MS guided protein-protein docking

Table 2.2. Software used for XL-MS guided protein-protein docking.

Software	Use	Reference	URL
CPORT	Prediction of protein-protein interface residues	78	https://alcazar.science.uu.nl/services/CPORT/
DisVis	Data-consistency and analysis of restraints information content	79,80	https://wenmr.science.uu.nl./disvis/
GenTBL	Generation of restraints files in .tbl format	71,82	https://alcazar.science.uu.nl/services/GenTBL/
HADDOCK 2.4	Data-driven docking of protein complexes	71,82	https://wenmr.science.uu.nl/haddock2.4/
NACCESS	Calculation of residue solvent-accessibility	83	http://www.bioinf.manchester.ac.uk/naccess/
Python	Analysis of structural parameters from docked structures and data representation	84	https://www.python.org
VMD	Protein visualization and high-quality image production	85	https://www.ks.uiuc.edu/Research/vmd/

2.4 Computational Alanine Scanning (CAS)

Although protein-protein interfaces are composed of a varied network of amino acids that help maintain the interaction, it has been proved that only a small fraction of the interfacial residues account for most of the binding free energy. Those key residues were named 'hotspots' by Clackson and Wells (1995)[86] and following studies have shown that the presence of these hotspots seems to be an extended characteristic of protein-protein interfaces[87]. The identification of hotspots is then a crucial point for the rational design of point mutations

disrupting protein-protein complexes and validation of protein-protein interactions by site-directed mutagenesis.

2.4.1 CAS procedure

CAS algorithms are designed to systemically perform *in silico* mutations of interfacial residues and compute the difference in binding free energy (ΔΔG) upon Ala mutation (Eq. 2.2).

$$\Delta\Delta G = \Delta G^{WT} - \Delta G^{MUT} \quad (2.2)$$

All available CAS predictors follow a similar workflow for the calculation of ΔΔG upon a specific mutation. ΔG. Such calculations start by defining the subset of interfacial residues (typically those residues within 4-5 Å of the other partner), then by replacing the residues individually with alanine and finally by computing the ΔG of the mutated complex ($\Delta G^{MUT}_{complex}$). Later, the protein stability change upon a mutation on both partners separately (ΔG^{MUT}_{A} and ΔG^{MUT}_{B}) is calculated. At the same time, the binding free energy for the WT complex ($\Delta G^{WT}_{complex}$) and the values for each partner are calculated too (ΔG^{WT}_{A} and ΔG^{WT}_{B}) [87,88]. Finally, the total change of binding free energy is computed as follows:

$$\Delta\Delta G_{bind} = \left(\Delta G^{WT}_{complex} - \Delta G^{WT}_{A} - \Delta G^{WT}_{B}\right) - \left(\Delta G^{MUT}_{complex} - \Delta G^{MUT}_{A} - \Delta G^{MUT}_{B}\right) \quad (2.3)$$

Although the estimation of a change in protein folding (ΔG_A and ΔG_B) upon mutation is amenable for computational methods, the prediction of binding energy changes remains challenging. CAS predictors vary on their way to estimate $\Delta G_{complex}$. Most of them depend on physical energy-based or statistical potentials or a combination of both. Recently, new CAS predictors have been developed using Machine Learning (ML). One clear advantage of ML-based predictors is that they use a more extensive parametrization, including more structural and evolutive terms for the estimation of ΔG. On the other hand, although ML-based predictors seem to outperform the classical physical/statistical-based ones, the dependence on high quality and varied datasets employed for their training could represent a limitation[89,90]. Therefore, a reasonable solution is the combination of different CAS software to obtain a consensus prediction for ΔΔG.

2.4.2 Software for CAS

Table 2.3. Software used for CAS. P: Physical energy-based predictor, S: Statistical-based predictor, P/S: Physical energy and statistical-based predictor, ML: Machine Learning-based predictor.

Software	Use	Reference	URL	CAS type
Anchor	Hot-spots identification	[91]	http://structure.pitt.edu/anchor/	P
BeAtMuSiC	Hot-spots identification	[88]	http://babylone.ulb.ac.be/beatmusic/	S
BUDE	Hot-spots identification	[92]	https://pragmaticproteindesign.bio.ed.ac.uk/balas/	S
mCSM-PPI2	Hot-spots identification	[93]	https://biosig.lab.uq.edu.au./mcsm_ppi2/	ML
Mutabind2	Hot-spots identification	[90,93]	https://lilab.jysw.suda.edu.cn/research/mutabind2/	P/S
Robetta	Hot-spots identification	[94]	https://robetta.bakerlab.org/alascansubmit.jsp	P/S
SAAMBE_3D	Hot-spots identification	[89]	http://compbio.clemson.edu/saambe_webserver/index3D.php	ML

2.5 Methods for studying $Ca_v\beta_2$/Actin interaction

$Ca_v\beta$ and actin interaction was unveiled following a XL-MS guided protein-protein docking protocol. Briefly, recombinantly expressed and purified $Ca_v\beta$ was chemically cross-linked with *in vitro* polymerized actin (F-actin) using two different MS-cleavable cross-linkers: DSBU and DSSO. The cross-linked complexes were resolved by SDS-PAGE and the bands of interest excised, processed, and analyzed by high resolution tandem mass spectrometry. MS data was analyzed with three different XL-software (Merox[65], MetaMorpheus[69] and MaxLynx[68]). Identified inter cross-links were defined as distances to guide a protein-protein docking in the HADDOCK 2.4 webserver[71,82]. The top four structures of the best scored cluster were subjected to a CAS to predict putative hotspots. Six different CAS software (Anchor[91], Robetta[94], BUDE[92], BeAtMuSiC[88], Mutabind2[89,90] and SAAMBE-3D[89]) were used to obtain a consensus prediction of $Ca_v\beta$ hotspots. Six and eight point Ala mutations were introduced in

$Ca_v\beta$ by site-directed mutagenesis. The mutant's affinity for F-actin was tested by actin co-sedimentation assays. Finally, the role of $Ca_v\beta$/Actin interaction was assessed *in cellulo* by electrophysiological recordings of $Ca_v\beta$ WT and $Ca_v\beta$ hotspot mutant with the calcium channel $Ca_v1.2$. A detailed description of the materials and methods are included in the enclosed manuscript (see section 3.1).

2.6 Methods for studying $Ca_v\beta_2$ dimerization

2.6.1 $Ca_v\beta_2$ purification

BL-21 (DE3) *Escherichia coli* (Novagen) bacteria were transformed with a cDNA encoding the core of a rat $Ca_v\beta_2$ subunit (UniProt ID Q8VGC3) with a poly-His tag (His_6-$Ca_v\beta_2$ core, for simplicity $Ca_v\beta_2$ core). The bacteria were grown in LB medium/Ampicillin (50 μg/ml) at 37 °C until OD_{600} reached a value of 0.6; in that moment, $Ca_v\beta_2$ core expression was induced with 0.5 mM isopropyl-D-thiogalactopyranoside (IPTG) for 2 hours.

After induction, bacteria were centrifuged at 6,000 xg 4 °C during 15 min in a Beckman Coulter centrifuge (Avanti JXN-30) and stored at -80 °C until used. Then, the pellet was resuspended in binding buffer (20 mM Phosphate pH 8, 500 mM NaCl, 30 mM Imidazole) supplemented with protease inhibitors (Complete Protease Inhibitor tablet, EDTA-free, Roche) and lysed in a W-450 D sonicator (Branson) using a 40% amplitude and a 2 minute programme.

The lysate was cleared by centrifugation (15.000 xg, 15 min, 4 °C) and the supernatant loaded on a HisTrap™ HP Ni^{2+}-NTA column (Cytiva), previously equilibrated with binding buffer. The protein was eluted using a 1 ml/min flowrate with an imidazole gradient in elution buffer (20 mM Phosphate pH 8, 500 mM NaCl, 500 mM Imidazole). Fractions of interest were collected and subjected to size-exclusion chromatography on a Superdex 200 16/600 column (Cytiva), previously equilibrated in GF-buffer (20 mM Phosphate pH 8, 150 mM NaCl).

The peak corresponding to the protein was subjected again to an analytical Superdex 200 10/30 column (Cytiva) in order to check the protein proper folding. The protein purity was assessed by denaturing SDS-PAGE. Protein samples were diluted in Laemmli sample buffer and run in a vertical electrophoresis cell (BioRad) with SDS-running buffer at 200V for 50 min. Gels were then stained for 30 min in a Coomassie staining solution and destained overnight with

Coomassie destaining solution. Protein bands were identified by comparing then with the molecular weight standard PageRuler^{TM} Plus.

2.6.2 Isotopic labelling (^{15}N) and purification of ^{15}N-Ca$_v\beta_2$ core

BL-21 (DE3) *Escherichia coli* bacteria previously transformed with the cDNA encoding Ca$_v\beta_2$ core were precultured in 5 ml LB medium/Ampicillin and grown overnight at 37 °C. Then, 500 µl of the preculture were added to 25 ml of minimal medium supplemented with Ammonium-^{15}N chloride as nitrogen source (for the complete recipe, please check Table 2.12) and incubated at 37 °C until the OD_{600} reached again a value of 0.6. Next, 25 ml of the grown bacteria in minimal medium were added to 475 ml minimal medium and grown at 37 °C until the OD_{600} reached a value of 0.6 again. In that moment, expression of Ca$_v\beta_2$ core was induced with 0.5 mM IPTG for 2 hours. The conditions for the purification of the ^{15}N-Ca$_v\beta_2$ core follow exactly the same as those specified in the section 2.6.1.

2.6.3 Determination of the heavy (^{15}N) and light (^{14}N) Ca$_v\beta_2$ core experimental masses

An Agilent UHPLC-ESI-QTOF-MS system was used to determine the labeling efficiency of ^{15}N-Ca$_v\beta_2$ core. The UHPLC (Agilent 1290 Infinity series) system consisted of a binary pump system, an autosampler, a thermostatted column compartment and a 6250 accurate-mass QTOF-MS with an electrospray ionization (ESI) interface with a resolution of 20,000. 2 µg of both light (^{14}N) and heavy (^{15}N) Ca$_v\beta_2$ core were injected separately and the chromatographic separation was performed on a Accucore-150-C4 (100 x 4.6 mm) 2.6 µm particle size; (Thermo Scientific, USA). Column temperature was kept at 50°C and flow rate was 500 µL/min. The mobile phase consisted of solvent A which was 0.025% HFBA and 1% FA in water, and solvent B, which was 0.025% HFBA and 1% FA in Acetonitrile. Sample injection volume was 10 ul. At the beginning of the run there was an isocratic step of 5% B (0 to 2 min) followed by an increase to 95% B within 30 min. 95% B was held for 2 min in order to clean the column. The gradient returned to 5% B within 0.1 min and equilibrated the system for 2 min. Detection was performed with the QTOF mass detector in the ESI positive ionization mode. The nebulizer pressure was set to 20 psig and the drying gas flow was set to 11 L/min. A fragmentation voltage of 215 V, a skimmer voltage of 68 V and an octopole voltage of 750 V were used. The mass range was set to m/z 500 to 3,000 and data acquisition rate was two spectra. Source temperature was set to 300°C. MassHunter software LC-MS Data Acquisition

B.05.01 (Agilent Technologies, Palo Alto, CA, USA) was used to control the instrument and data acquisition.

The heavy and light experimental masses were determined by taking a subrange of consecutive m/z values and submitting them to the server ESIprot[95]. ESIprot is able to calculate the different charge states associated to each m/z value, providing an average deconvoluted molecular weight.

2.6.4 Denaturation and refolding of heavy and light $Ca_v\beta_2$ core

The objective of this denaturation/refolding procedure is to ensure a proper recombination of the heavy and light $Ca_v\beta_2$ core monomers. Both protein forms were diluted separately to achieve a concentration of 0.05 mg/ml (1 μM) in denaturing buffer (20 mM Phosphate pH 8, 150 mM NaCl, 10 mM DTT, 3M Guanidine-HCl) and incubated for 1 h at 4 °C. Then, both were mixed and incubated overnight at 4 °C while rotating. After the incubation, the denaturing reagent Guanidine-HCl was eliminated through sequential dialysis using a 8 kDa cutoff dialysis membrane (SERVA). After dialysis and to eliminate possible aggregates, the $Ca_v\beta_2$ core mix was centrifuged at 15,000 xg 4 °C for 15 min and concentrated up to 0.5 mg/ml (10 μM).

2.6.5 Chemical cross-linking

Since there is no available cross-linking analysis software able to analyze data resulting from stably labeled homodimers with MS-cleavable cross-linkers, a non-cleavable cross-linker, disuccinimidyl suberate (DSS) was used. DSS contains identical NHS groups at either end, reactive against lysine residues, separated by a spacer of length 11.4 Å.

A 10 μM solution containing $Ca_v\beta_2$ core was cross-linked with DSS (Thermo Scientific) 20x molar excess and incubated for 30 min at 22 °C. After incubation, the cross-linking reaction was quenched with 50 mM Tris-HCl for 30 min and the samples resolved by denaturing SDS-PAGE. After SDS-PAGE, bands of interest were cut and dried at 45 ºC for 45 min.

2.6.6 In-gel digestion

Protein bands were chopped and destained by three times alternating 10-min treatments with buffer A (10 mM ammoniumhydrogencarbonate, pH 8.3) and buffer B (buffer A:100% acetonitrile from Merck KGaA, Darmstadt, Germanyin a ratio of 50:50 (v/v)). After the second incubation with 50 mM ammonium bicarbonate, samples were treated with 50 µL 10 mM dithiothreitol (DTT) (AppliChem GmbH, Darmstadt, Germany) for 1 h at 56 °C and with 50 µL 50 mM IAA (Merck KGaA) for 45 min at room temperature before the destaining protocol was continued. Finally, gel pieces were dried in a vacuum concentrator (RVC2-25CD plus, Martin Christ Gefriertrocknungsanlagen, Osterode am Harz, Germany). Digestion was initiated by adding 8 µL of trypsin solution (0.015 µg/µL, Serva, Heidelberg, Germany) and was performed overnight. The digestion was stopped, and peptides eluted by incubating the gel pieces twice for 15 min with 30 µL of a 1:1 solution containing 100% acetonitrile and 0.1% (v/v) TFA (Merck KGaA, Darmstadt, Germany) in an ice-cooled ultrasonic bath. Samples were dried in a vacuum concentrator and resuspended in 40 µL 0.1% (v/v) TFA. Afterwards, the peptide concentration was determined by amino acid analysis (AAA) as described in reference [96].

2.6.7 Nano LC-ESI-MS/MS measurements

Tryptic peptides were measured by nano LC-ESI-MS/MS. A Vanquish Neo UHPLC-system (Thermo Scientific, Bremen, Germany) was utilized for nano HPLC analysis using the following solvent system: (A) 0.1% FA; (B) 84% ACN, 0.1% FA. Samples were initially loaded on a trap column (Thermo PepMap Neo cartridge, 100 µm × 2 cm, particle size 5 µm, pore size 100 Å, C18) with a flow rate of 30 µl/min with 0.1% TFA. After sample concentration and washing, the trap column was serially connected with an analytical C18 column (Thermo DNV PepMap Neo, 75 µm × 50 cm, particle size 2 µm, pore size 100 Å), and the peptides were separated with a flow rate of 400 nl/min using a solvent gradient of 1% to 21% B for 70 min at 60 °C. The protocol continued with a gradient of 21% to 40% buffer B for 95 min and a column wash for 5 minutes with 95% B (84% acetonitrile in 0.1% TFA). After each sample measurement, 1 h of column washing was performed for equilibration. The HPLC system was on-line connected to the nano-electrospray ionization source of a Q-Exactive HF (Thermo Scientific, Bremen, Germany). Full MS spectra were scanned between 400–1,600 m/z with a resolution of 120,000 at 200 m/z (AGC target 1e6, 20 ms maximum injection time). Capillary

temperature was set to 275 °C and spray voltage to 1,500 V (positive mode). Lock mass polydimethylcyclosiloxane (m/z 445.120) was used for internal recalibration. The m/z values initiating MS/MS were set on a dynamic exclusion list for 30 s and the 10 most intensive ions (charge 2+ to 7+) were selected for fragmentation. MS/MS fragments were generated by higher-energy-collision-induced dissociation and the fragmentation was performed with 28% normalized collision energy. The fragment analysis was performed in an Orbitrap analyzer with resolution 30,000 at 200 m/z (AGC 1e6, maximum injection time 120 ms).

2.6.8 Cross-linking data analysis

Cross-linking data was analysed with the software SIM-XL[70]. The raw MS data and $Ca_v\beta_2$ core fasta sequence file were provided. The search was performed with the following specifications: cross-linker DSS, 20 ppm and 20 ppm for the precursor and fragment ion precision, respectively, and higher-energy C-trap dissociation (HCD) as fragmentation method. The fixed modification of carbamidomethylation of cysteine was taken into consideration. Up to three missed cleavages were allowed for trypsin. The homodimer analysis feature of SIM-XL was activated and ^{15}N labelling was chosen. Every cross-link resulting from the search with a score higher than 3 for inter-links and 2 for intra-links was checked manually to ensure a proper peak assignment and classified as Excellent, Good, Medium, Fair and Poor according to software developers' recommendation[63,70].

2.6.9 Protein-protein docking with HADDOCK.

The rat $Ca_v\beta_2$ structure with PDB code 5V2P was used to run a data-driven docking of dimeric $Ca_v\beta_2$ (Figure 2.4) according to a standard docking protocol for homooligomers[97]. Such *ab initio* approach had to be employed here due to the identified cross-linked residues being located in disordered regions in the protein structure. Briefly, ambiguous restraints in the form of active and passive residues predicted with CPORT were provided. To ensure no large variations in the homodimer conformation occur, NonCrystallographic symmetry (NCS) restraints were selected and defined as a segment of the protein length. Such restraint enforces that the two monomers should be identical, without defining any symmetry operation between them. Moreover, a C2 symmetry restraint was defined for the homodimer. As it was not possible to incorporate experimental data in the form of distance restraints, the structure sampling was increased to 10,000 poses for rigid body docking, and 400 for the semi-flexible refinement and explicit solvent refinement steps. A final refinement with a short molecular dynamics

simulation of 2.5 ns in water was performed. The final 400 structures were analysed and clustered according to their protein-protein interface RMSD (i-RMSD) using a cutoff of 7.5 Å.

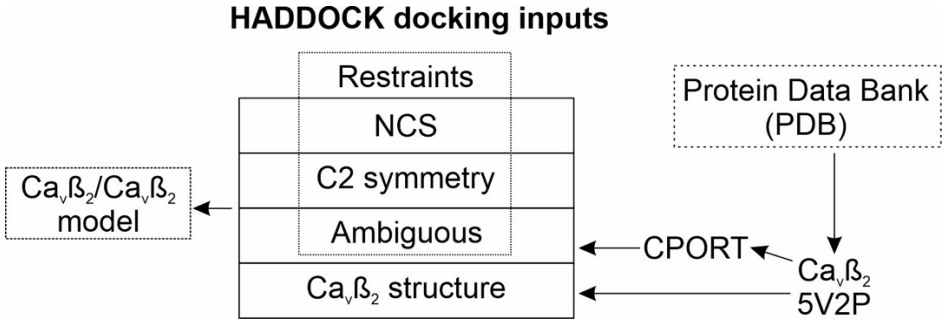

Figure 2.4. $Ca_v\beta_2$ dimer modeling workflow.

2.6.10 Downstream docked structures analysis

In order to analyse the resulting structures of the HADDOCK docking, the Python library MDAnalysis was used[98,99]. MDAnalysis is a library designed for the analysis of ensembles of structures, e.g. from molecular dynamics (MD) simulations trajectories. Data on structures are stored in Numpy arrays, which allow an easy access to the atomic coordinates to perform the desired calculations. In particular, MDAnalysis was used here to store the atomic coordinates of HADDOCK docked structures and measure inter-atomic distances. The resulting data was plotted using the libraries Matplotlib[100] and Seaborn[101] of Python.

Distances between DSS-cross-linked residues were measured in every resulting structure from the docking. As some residues were located in non-resolved regions of the $Ca_v\beta_2$ structure (PDB 5V2P), the distance to the closest resolved residue was measured instead. Then distances were weight-averaged. Such weights were calculated as the number of residues between the non-resolved and the closest resolved one normalized by the value of the cross-link displaying the smallest value. At the same time, to evaluate the conformation of dimers (e.g. head-to-head or head-to-tail), the distance between the center of mass of the SH3 domain of one chain and the GK of the partner chain was measured.

Interestingly, HADDOCK cluster structures displaying lower inter cross-linked distances were characterized by a head-to-tail conformation. This evidence was taking into consideration to select the best-scored cluster whose component structures presented such conformation for further experimental validation.

2.6.11 Computational Alanine Scanning

The top four structures belonging to that HADDOCK cluster selected as described in the previous section were analysed using a set of seven CAS predictors (listed in Table 2.3) to identify hotspots (section 2.4). Residues were ranked according to their difference in binding free energy upon Ala mutation (ΔΔG), which was averaged over the four docked structures and over the seven predictors to obtain a consensus prediction.

The set of 10 residues located at the dimeric interface showing the highest ΔΔG value were inspected to study the molecular interactions that they were involved with. Residues whose mutation could affect protein stability or could be counteracted by a neighbour residue able to form the same type of protein-protein interaction across the interface were discarded. Finally, a set of six residues (C113, H131, R134, D388, D394 and Y402, see section 3.2.3) was selected for alanine substitution.

2.6.12 Site-directed mutagenesis

2.6.12.1 Construction of plasmids

The software VectorNTI (InforMax Inc) was used for designing the cloning strategy, primers and sequencing of the vectors. Briefly, the strategy consisted in introducing six point mutations by the creation of two cassettes using as template a pRSET vector with a cDNA encoding the core of a rat poly-His $Ca_v\beta_2$ subunit. The first cassette grouped the first three mutations (C113A, H131A and R134A) and they were introduced by overlapping PCR using the restriction sites NheI and ApaI. The second cassette grouped the other three point mutations (D388A, D394A and Y402) and were introduced with a unique PCR using the restriction sites ApaI and EcoRI. Finally, the second cassette was subcloned in the vector bearing the first three mutations.

2.6.12.2 Polymerase Chain Reaction (PCR)

PCR was used to amplify regions of the cDNA encoding the WT $Ca_v\beta_2$ core with primers carrying the desired mutations. The PCR was carried out with the KOD Hot Start DNA Polymerase Kit (Merck Millipore) according to the manufacturer's protocol. Further details on the PCR are provided in Table 2.4 and Table 2.5.

Table 2.4. PCR reaction mixture.

Component	Volume (µl)	Final Concentration
10X Buffer for KOD hot Start DNA polymerase	5	1X
25 mM $MgSO_4$	3	1.5 mM
dNTPs	5	0.2 mM
H_2O bidistilled	Rest till total volume	
Sense primer (10 µM in water)	1.5	0.3 µM
Antisense primer (10 µM in water)	1.5	0.3 µM
Template DNA (10 ng)	Corresponding volume	
KOD hot Start DNA Polymerase (1 U/µl)	1	0.02 U/µl
Total volume	50	

The following conditions for the temperature cycles were used:

Table 2.5. Thermocycling conditions.

Step		Temperature (ºC)	Time (s)
40 cycles	Polymerase activation	95	120
	denaturation	95	20
	Annealing	56	20
	Extension	68	20
	Hold	8	-

When the PCR was finished, the resulting solution was run in a 1.5% agarose gel at 120V for 20 min in TAE buffer. DNA fragments were detected by mixing with SYBR Safe DNA Gel Stain (1X; Invitrogen) and visualized in a Biorad Gel DocTM XR+ System (Bio-Rad, Munich). DNA ladder GeneRuler 1 kb (ThermoScientific) molecular mass markers was used. The band of interest was excised, and the amplified DNA purified using the NucleoSpin Gel and PCR-Cleanup Kit (Macherey-Nagel) according to the manufacturer's instructions. The PCR fragment was eluted in water and stored till use.

Table 2.6. List of primers. s: sense; as: antisense.

Number	Sequence	Direction
1	GACGATAAGGATCCTAGCCGCCC	s
2	GCTTGGCTGCCTGTTCAGCCTGTAGCCTCATGTTCTCTAGTTTGACCG GGCTTGGAATAAATCCGATTTCAGCGCCTTC	as

3	GAAGGCGCTGAAATCGGATTTATTCCAAGCCCGGTCAAACTAGAGA ACATGAGGCTACAGGCTGAACAGGCAGCCAAGC	s
4	CAGGGAGGGGCCCACCAAC	as
5	TGTTGGTGGGCCCCTCCC	s
6	GCTTCGAATTCTCAAAGGAGAGGGTTGGGGAGGTTACTGCTGGGAG GGTGGGTGGCCTTCCAGTACGCCTCCAGAGCGTCGGCGAGATGCTCA CAAGCAGCCTCAAGTTGGTTCTCAGCCAAGATC	as

2.6.12.3 Restriction digestion

In order to clone the purified PCR amplified DNA fragment in the desired vector, both PCR fragments and vector were digested with the same pair of enzymes (Table 2.7). Restrictions total volumes were 30 ul or 10ul and performed for 60 or 30 min at 37 ºC depending on whether they were preparative or analytic respectively.

Table 2.7. Restriction digestion conditions

Component	Analytic (µl)	Preparative
FastDigest Enzyme I	0.2	1
FastDigest Enzyme II	0.2	1
10X FastDigest Green Buffer	1	3
Plasmid or PCR fragment	For 1 µg	For 3 µg
H_2O bidistilled	Rest till total volume	Rest till total volume
Total volume	10	30

The bands of interest were visualized and purified according to the protocol described in the section 2.6.12.2.

2.6.12.4 Ligation of DNA fragments.

The purified and restricted vector and PCR fragment were covalently linked by a T4 DNA ligase. The process of the ligation was carried out using the Rapid DNA Ligation Kit (ThermoScientific) according to the manufacturer's instructions. Briefly, the components were mixed (Table 2.8) and incubated at 22 ºC for 20 min at 320 rpm.

Table 2.8. Ligation conditions

Component	Volume (µl)
Linearized vector	For 100 ng
Insert DNA (1:3 vector:insert excess)	

5X Rapid Ligation buffer	4
T4 DNA Ligase, 5 U/µl	1
H_2O bidistilled	Rest till total volume
Total volume	20

2.6.12.5 Transformation in TOP10 F competent cells

For transformation, 50 µl of competent TOP 10 F cell suspension (Invitrogen) were mixed with 5 µl of ligated DNA and incubated on ice for 20 min. After a 42 °C heat shock, the suspension was again incubated on ice for 10 min. Then, 200 µl LB medium was added and bacteria incubated for 30 min at 37 °C while shaking at 800 rpm. Then bacteria were plated on LB agar containing ampicillin and incubated overnight at 37 °C.

2.6.12.6 Colony isolation and sequencing

Colonies were picked and grown in 5 ml LB medium with Ampicillin. For Mini preparation, the NucleoSpin Plasmid Kit from Macherey-Nagel was used according to manufacturers' instructions. DNA was eluted in Tris-EDTA buffer for long-time storage. The concentrations of the purified vectors were measured with the NanoDrop photometer (NanoDrop 2000, ThermoScientific). A control restriction (Table 2.7) was performed to evaluate the right DNA band pattern. Then, the vectors were sent for sequencing.

The identity of cDNAs was verified by DNA sequence analysis. Sequencing was performed by Eurofins Genomics (Ebersberg, Germany).

2.6.13 $Ca_v\beta_2$ core 6A purification

In general terms, $Ca_v\beta_2$ core 6A purification was identical to the one for $Ca_v\beta_2$ core described in section 2.6.1. The main change was the use of GF-300 buffer (20 mM Phosphate pH8, 300 mM NaCl) for the size-exclusion chromatography step.

2.6.14 GST-based pull-down assay

For this assay, Glutathione S-transferase (GST) as a negative control and the fusion protein GST-AID were fixed separately on glutathione beads (Cytiva) and equilibrated in GF-buffer supplemented with 1% Triton-X100. Then, refolded $Ca_v\beta_2$ core was incubated with the beads at 22 °C for 30 min. A control with $Ca_v\beta_2$ core which was not subjected to denaturation

was included. After incubation, the proteins on the beads were washed, eluted in Laemli loading buffer and resolved by denaturing SDS-PAGE.

2.6.15 Tryptophan Intrinsic Fluorescence

Intrinsic fluorescence experiments were performed using a FS5 Fluorescence Spectrometer (Edinburgh Instruments, UK) equipped with 500 µl cuvette holder coupled to a SC-25 temperature holder and a TC-1S temperature controller (Quantum Northwest, USA). Tryptophan residues were excited at 280 nm and the emission spectra were recorded at 300–430 nm in steps of 1 nm over a range of temperatures between 20 °C and 74 °C. For data analysis, the spectral center of mass (CM) was determined as follows:

$$CM = \frac{\sum_i F_i \lambda_i}{\sum_i F_i} \tag{2.4}$$

Where F is the fluorescence intensity and λ the wavelength at *i* temperature. CM dependency on temperature was studied. The transition temperatures were obtained by non-linear regression fitting to a two-state or three-state transition model when necessary:

$$y = \frac{\alpha_n + \beta_n T}{1 + e^{\frac{4T_m(T-T_m)}{T\Delta T}}} + \frac{\alpha_d + \beta_d T}{1 + e^{\frac{4T_m(T_m-T)}{T\Delta T}}} \tag{2.5}$$

Two-state transition

$$y = \frac{\alpha_n + \beta_n T + (\alpha_I + \beta_I T)e^{-\frac{\Delta G1}{RT}} + (\alpha_d + \beta_d T)e^{-\frac{\Delta G1+\Delta G2}{RT}}}{1 + e^{\frac{-\Delta G1}{RT}} + e^{-\frac{\Delta G1+\Delta G2}{RT}}} \tag{2.6}$$

Three-state transition

$$\Delta G_1 = \frac{4T_{m1}(T_{m1} - T)}{\Delta T_1} \tag{2.6.1}$$

$$\Delta G_2 = \frac{4T_{m2}(T_{m2} - T)}{\Delta T_2} \tag{2.6.2}$$

Where y is CM, α and β are the intercept and slope of the native (n), denatured (d) or intermediate (I) states respectively, T the temperature, T_m the transition temperature, ΔT the width of the transition and *e* the exponential function.

2.6.16 Blue-native gel electrophoresis (BN-PAGE)

In order to study the different oligomeric states of the $Ca_v\beta_2$ core and $Ca_v\beta_2$ core 6A in native conditions, BN-PAGE was used. BN-PAGE was performed as described in reference [102]. Briefly, for the gel and buffer preparations, only SDS-free reagents were used. The samples were diluted in loading buffer (100 mM Tris-HCl pH 8, 40% glycerol, 0.5% Coomassie Brilliant Blue) and run in a gradient gel with polyacrylamide concentrations ranging from 4% to 14% in the separating gel and 4% as stacking gel. A cathode buffer (100 mM Histidine pH 8, 0.002% ServaBlue G) and an anode buffer (100 mM Tris-HCl pH 8.8) were prepared freshly and filtered with a 0.45 µm membrane before use. The gel was runned for 16 h at 25 V and 4 °C. For clearing the bands, the gel was destained in native destaining solution (7.5% Acetic acid, 5% Ethanol).

2.6.17 Densitometric analysis with Image Lab

BN-PAGE gels were visualized in a Biorad Gel DocTM XR+ System (Bio-Rad, Munich), scanned and analyzed with Image Lab Software (RRID:SCR_014210). The Auto Analysis feature of Image Lab was used. Briefly, gel lanes were found, and rectangular regions of interest (ROIs) were drawn. Then, the bands on each lane were detected using the low sensitive detection mode and the profile plots calculated. These profiles represent the relative intensity of the contents over the lane length. The raw intensity value of each peak is calculated as the area under the curve by integration of the peak. After background subtraction, the adjusted intensity values for each band were exported and further analyzed with OriginPro (OriginLab, Northampton USA).

2.6.18 Statistical analysis with OriginPro

The adjusted integrated values of the monomeric and dimeric bands were used to calculate the dimeric fraction as follows:

$$Dimeric\ fraction = \frac{I_D}{I_M + I_D} \tag{2.7}$$

Where I_M and I_D correspond to the adjusted intensities of the monomeric and dimeric bands of the proteins respectively. Statistical differences between the $Ca_v\beta_2$ core and $Ca_v\beta_2$ core 6A dimeric fractions were computed using a Student t-test in OriginPro.

2.7 Chemicals and solutions

Table 2.9. Reagents and materials for protein expression and purification

Reagents and Materials	Catalog N°
BL21 (DE3) competent *E.coli* cells, BioLabs	C25271
Isopropylthio-β-galactoside (IPTG) BioChemica, AppliChem	A1008
Glycerol, AppliChem	A2926
cOmplete™ EDTA-free Protease Inhibitor Cocktail, Roche, Merck	05056489001
Syringe filter 0.22µm, Fisher Scientific	15181499
DURAPORE®0.22µm Membrane filters, Merck	GVWP04700
HisTrap™ HP column, Cytiva	17524701
Superdex™ 200 pg HiLoad™ 16/60 column, Cytiva	28989335
Superdex™ 200 Increase 10/300 GL column, Cytiva	28990944
Amicon® Ultra-15 Centrifugal Filters (10K), Merck Millipore Ltd.	UFC9010
Nickel Sulfate Hexahydrate ($NiSO_4$), Merck	N4882
Sodium di-Hydrogen Phosphate 1-hydrate (NaH_2PO_4), AppliChem	131965
Ethylenediaminetetraacetic acid (EDTA), Carl Roth	1PHC
Guanidine Hydrochoride, Fisher	BP178-1
Dithiothreitol (DTT), AppliChem	A1101
Imidazole hydrochloride, Merck	I3386

Table 2.10. List of compounds for SDS-PAGE

Compounds	Catalog N°
Acetic-acid 96%, Merck	1.00062
Ammonium persulfate (APS), AppliChem	A1142
Bromphenol blue, Sigma Chemical	B-6896
Coomassie Brilliant Blue, SERVA	17525
Ethanol 99.8% Denatured, AppliChem	147194
Glycine for analysis, AppliChem	131340
Hydrochloric acid 32% for analysis (HCl), Merck	1.00319

PageRuler™ Plus, Prestained Protein Ladder, Thermo Scientific™	26619
Acrylamide/Bis Solution, 37.5:1, SERVA	10688
Sodium dodecyl sulphate (SDS), SERVA	20765
Tetramethylethylenediamine (TEMED), Merck	T9281
Tris for molecular biology, AppliChem	A2264

Table 2.11. List of compounds for chemical cross-linking

Compounds	Catalog N°
Pierce™ DSS, No-Weight™ format, Thermo Scientific	A39267
Dimethylsulfoxide (DMSO) anhydrous, Invitrogen™	D12345

Table 2.12. Minimal medium

Component	Amount	Catalog Nº
Calcium chloride ($CaCl_2$), AppliChem	0.1 mM	131232.1210
Magnesium Sulfate ($MgSO_4$), KMF Optichem	2 mM	KMF.08-886.0500
Thiamine, Merck	10 ug/ml	T1270
Ammonium-^{15}N chloride ($^{15}NH_4Cl$), Merck	1 mg/ml	299251
Glucose, AppliChem	7 mg/ml	A3666,1000
M9 Medium 10x	5%	-
Metal Mix 100x	1%	-
Ampicillin, AppliChem	0.1 %	A3650

Table 2.13. M9 10x

Component	Amount	Catalog Nº
Disodium hydrogen phosphate (Na_2HPO_4), AppliChem	60 g/L	122507.1211
Sodium di-Hydrogen Phosphate 1-hydrate (NaH_2PO_4), AppliChem	30 g/L	131965.1211
Sodium chloride (NaCl), AppliChem	5 g/L	131659.1211

Table 2.14. Metal Mix 100x

Component	Amount	Catalog Nº
Iron (III) chloride hexahydrate ($FeCl_3$ x $6H_2O$), Merck	0.83 g/L	F2877
Zinc chloride ($ZnCl_2$), ApplicChem	84 mg/L	A3451,0500
Copper (II) Chloride hydrate ($CuCl_2$ x $2H_2O$), Riedel-deHäen	13 mg/L	12825
Boric acid (H_3BO_3), Merck	10 mg/L	B0252
EDTA, Merck	5 g/L	E9884

Manganese (II) chloride tetrahydrate ($MnCl_2$ x $4H_2O$), Merck	1.67 mg/L	M-3634

Table 2.15. Reagents and kits used in site-directed mutagenesis

Reagents and Kits	Catalog N°
pRSET, Invitrogen™	V35120
pcDNA 3.1 (+),Invitrogen™	V79020
KOD Hot Start DNA Polymerase Kit, Sigma Aldrich	71086
Primers, Eurofins Genomics	-
NucleoSpin Gel and PCR Clean-up, Macherey-Nagel	740609
Rapid DNA Ligation Kit, Thermo Scientific™	K1422
FastDigest ApaI, Thermo Scientific™	FD1414
FastDigest EcoRI, Thermo Scientific™	FD0275
FastDigest NheI, Thermo Scientific™	FD0974
FastDigest BamHI, Thermo Scientific™	FD0054
FastDigest Green Buffer (10X), Thermo Scientific™	B72
NucleoSpin Plasmid (DNA Purifikation Kit), Macherey-Nagel	740588
Agarose NEEO ultra-quality, Carl Roth	2267
SYBR™ Safe DNA Gel Stain, Invitrogen, ThermoFischer	S33102
GeneRuler 1 kb DNA Ladder, Thermo Scientific™	SM0313
LB-Medium/-Agar (Miller), AppliChem	A0954/A0927
Ampicillin, Applichem	A3650
TOP10F competent *E.coli* cells, Invitrogen	C303006

Table 2.16. List of compounds for BN-PAGE

Compounds	Catalog N°
L-Histidine, Merck	H800
Coomassie, SERVA	17524
Native Marker liquid mix, SERVA	39219.01
Korasilon paste, Kurt Obermeier	2007434

Chapter 3. Results

3.1 Interaction of $Ca_V\beta$ and actin supports the clearance of functionally defective $Ca_V1.2$ channels

Francisco Castilla, Victor Lugo, Erick Miranda-Laferte, Nadine Jordan, Pitter Huesgen, Beatrix Santiago-Schübel, Mercedes Alfonso-Prieto, Patricia Hidalgo

Pages: 44 –99

Status: To be submitted

Contribution: I designed and performed the cloning of cDNA constructs encoding $Ca_v\beta$ used in this study and carried out the expression and purification of the proteins, *in vitro* cross-linking, analysed and collected all data for mass spectrometry, protein-protein docking, binding assays, western blots, laser scanning confocal microscopy, except for the electrophysiological data; prepared the figures and contributed to writing the manuscript.

Interaction of $Ca_V\beta$ and actin supports the clearance of functionally defective $Ca_V1.2$ channels

Francisco Castilla[1,2], Victor Lugo[1], Erick Miranda-Laferte[1], Nadine Jordan[1], Pitter Huesgen[3], Beatrix Santiago-Schübel[3], Mercedes Alfonso-Prieto[4,5], Patricia Hidalgo[1,6]

[1]Institute of Biological Information Processing (IBI-1) - Molecular and Cellular Physiology, Forschungszentrum Jülich, 52425 Jülich, Germany

[2]Graduate Program, Faculty of Mathematics and Natural Sciences, Heinrich-Heine University, 40225 Düsseldorf, Germany

[3]Central Institute of Engineering, Electronics and Analytics (ZEA-3), Forschungszentrum Jülich, 52425 Jülich, Germany

[4]Institute of Neuroscience and Medicine (INM-9) and Institute for Advanced Simulations (IAS-5), Forschungszentrum Jülich, 52425 Jülich, Germany

[5]Cécile and Vogt Institute for Brain Research, Medical Faculty, Heinrich-Heine University, 40225 Düsseldorf, Germany

[6]Institute of Biochemistry, Heinrich-Heine University, 40225 Düsseldorf, Germany

Correspondence:

Beatrix Santiago-Schübel. Forschungszentrum Jülich, Central Institute of Engineering, Electronics and Analytics (ZEA-3). Email: b.santiago-schuebel@fz-juelich.de
Mercedes Alfonso-Prieto. Forschungszentrum Jülich, Institute of Neuroscience and Medicine (INM-9) and Institute for Advanced Simulations (IAS-5). Email: m.alfonso-prieto@fz-juelich.de
Patricia Hidalgo. Forschungszentrum Jülich, Institute of Biological Information Processing (IBI-1), Jülich. Email: pa.hidalgo@fz-juelich.de

KEY WORDS: calcium channel β-subunit, actin filaments, cross-linking mass spectrometry, protein-protein docking, hotspots, $Ca_V1.2$ surface expression

Running Title: $Ca_V\beta$/actin interaction surface

Abstract

Voltage-gated calcium channels (Ca_V) couple membrane depolarization to calcium-triggered cellular responses. Their malfunction associates with several cardiovascular and neurological disorders. $Ca_V\beta$, a core component of Ca_V complex, regulates dynamically conduction and trafficking of the channel through multifarious mechanisms by rewiring the cellular repertoire of protein interactions. Among them, $Ca_V\beta$ interaction with cytoskeletal actin up-regulates L-type calcium currents in cardiac cells in an unclear manner. We here identified the interaction surface between $Ca_V\beta$ and actin using cross-linking mass spectrometry and protein-protein docking. The molecular complex involves one $Ca_V\beta$ simultaneously interacting with two adjacent actin monomers. Electrostatic mapping reveals a patch of positively charged residues at the $Ca_V\beta$ contact interface complementary to the negatively charged surface of actin. Consistently, increasing the ionic strength decreases the *in vitro* binding affinity of $Ca_V\beta$ for actin. Computational alanine scanning identified a common set of eight hotspots in two members of the $Ca_V\beta$ family, $Ca_V\beta_2$ and $Ca_V\beta_4$, that significantly decreased their interaction with actin *in vitro* while preserving association with the Ca_V channel complex. In cells coexpressing L-type $Ca_V1.2$ channel with the actin association-deficient $Ca_V\beta_2$ mutant, ionic currents were considerably reduced without changes in the total amount of channels at the plasma membrane. Stationary noise-analysis showed a significant decrease in the number of functionally available channels without alterations in the unitary properties of the remaining channels, suggesting an increased fraction of conduction-defective channels. Our results uncover a role of $Ca_V\beta$/actin association in the quality control of Ca_V channels at the cell surface and provide a molecular model that expands the landscape of drug targetable protein-protein interfaces in Ca_V associated channelopathies.

Introduction

Voltage-gated calcium channels (Ca_V) couple membrane depolarization to numerous calcium triggered cellular responses including muscle contraction, neurotransmission and gene expression[1]. Anomalous calcium influx through Ca_V channels results in several cardiovascular, neurological and psychiatric pathologic conditions that are collectively known as calcium channelopathies[2-11].

The functional core of the of the high voltage-activated calcium channel complex is formed by the $Ca_V\alpha_1$ pore-forming subunit and the β-subunit ($Ca_V\beta$), which multiply regulates calcium signaling pathways by directly controlling calcium permeation and intracellular trafficking of $Ca_V\alpha_1$ [12-15].

Besides, $Ca_V\beta$ interacts with diverse protein partners, even in cellular systems lacking functional Ca_V channels, and fulfils a variety of functions beyond its canonical task in potentiating ionic currents as part of the Ca_V protein complex[12,13,16-20].

$Ca_V\beta$ family encompasses four subclasses ($Ca_V\beta_1$ to $Ca_V\beta_4$), each with several alternative splice variants, different regulatory functions and tissue-expression patterns, and likely tissue specific protein-protein interaction (PPI) networks[12,13,17,21-23]. $Ca_V\beta$ exhibits a modular architecture, being one of the smallest members of the membrane-associated guanylate kinase (MAGUK) family and containing two PPI domains: one Src homology 3 (SH3) domain and one guanylate kinase (GK) domain that are highly conserved among the different isoforms. In contrast, the N- and C-terminal regions and the linker joining the two conserved domains (known as HOOK) are variable in sequence and length. The SH3 and GK domains form the functional core of the protein recapitulating most of the channel modulatory functions[24-26].

High-resolution crystal structures are available for $Ca_V\beta_2$, $Ca_V\beta_3$ and $Ca_V\beta_4$ subunits alone and in complex with the highly conserved consensus sequence of 18 amino acids located on the intracellular I-II loop of $Ca_V\alpha_1$ known as the α_1 interaction domain (AID)[27-30]. The AID forms an α-helix that fits into a conserved hydrophobic groove (α-binding pocket or ABP) formed exclusively by GK residues. $Ca_V\beta$ has an elongated shape, with the SH3 and GK domains lying on opposite sides. However, no crystallographic data are available for the flexible regions.

The repertoire of $Ca_V\beta$ interacting partners includes filamentous actin (F-actin)[31,32]. We have previously demonstrated that two $Ca_V\beta$ isoforms, $Ca_V\beta_2$ and $Ca_V\beta_4$, which are highly expressed in heart and brain, respectively, associate directly with actin.

In the absence of a molecular model for the $Ca_V\beta$/actin interaction, its functional impact has been explored in the past using inhibitors of actin polymerization as a tool to disrupt this interaction[31,32]. Using this strategy, it has been shown that this PPI upregulates L-type calcium currents in HL-1 cardiomyocytes, evoking the condition observed in certain myocardial dysfunctions[31]. In primary hippocampal neurons this interaction enhances synaptic strength[32].

Here we elucidated the interaction surface of $Ca_V\beta_2$ and $Ca_V\beta_4$, with actin by a combination of chemical cross-linking mass spectrometry (XL-MS) and computational biology. We identified several hotspots residues that allowed the generation of $Ca_V\beta$ mutants with significantly reduced *in vitro* affinity for actin, while maintaining the affinity for the AID site.

Electrophysiological recordings from cells coexpressing $Ca_V1.2$ with a $Ca_V\beta_2$ actin-association-deficient mutant revealed diminished ionic currents compared to cells coexpressing wild-type $Ca_V\beta_2$. Combining gating currents measurements and stationary noise analysis, we show that the $Ca_V\beta_2$ mutant reduces the number of functionally available channels at the plasma membrane and propose a model in which the $Ca_V\beta$/actin interaction regulates the clearance of defective channels from the plasma membrane.

Besides defining a new role for $Ca_V\beta$ in endocytic quality control of Ca_v at the cell surface, our findings introduce a potentially novel druggable protein-protein interface for intervening in Ca_V-associated genetic diseases.

Methods

cDNA constructs and chemicals. Rat $Ca_V\beta_2$ and human $Ca_V\beta_4$ corresponding to UniProtKB accession numbers, Q8VGC3-2 and O00305-1, respectively, were used in this study. The pRSETB plasmids (Invitrogen, Carlsbad, CA, USA) encompassing the core regions of $Ca_V\beta_2$ (residues 23-422) and $Ca_V\beta_4$ (residues 50-408) have been previously described[25,31,32]. The pRSETB vector containing the $Ca_V\beta_4$ R482X epilepsy-causing mutant (residues 1-431) was generated by overlapping PCR and standard molecular biology methods using the vector pRSETB $Ca_V\beta_4$ as template. All recombinant proteins are expressed with a 6xHistidine tag fused to their N-terminus. $Ca_V1.2$-mNeonGreen (rabbit $Ca_V1.2$ cDNA (accession number UniProtKB P15381) and $Ca_V\beta_2$-mRFP constructs used for electrophysiology have been previously described[31,33]. Rabbit skeletal muscle actin protein and actin binding protein Biochem kit were purchased from Cytoskeleton (Cytoskeleton, Inc, Denver, CO, USA). The mass spectrometry cleavable cross-linkers DSBU (Disuccinimidyl Dibutyric Urea) and DSSO (Disuccinimidyl Sulfoxide) were purchased from Thermo Fischer Scientific.

Mutagenesis. The constructs $Ca_V\beta_2$-core 8Ala, $Ca_V\beta_2$-core 6Ala, $Ca_V\beta_4$ R482X 8Ala and $Ca_V\beta_4$ R482X 6Ala were generated by overlapping PCR and standard molecular biology methods using the pRSETB $Ca_V\beta_2$-core and pRSETB $Ca_V\beta_4$ R482X vectors as templates for the $Ca_V\beta_2$ and $Ca_V\beta_4$ mutants, respectively. $Ca_V\beta_2$ 8Ala-mRFP inserted in p156rrl vector was generated in a similar way as pRSETB $Ca_V\beta_2$-core 8Ala, but using the plasmid p156rrl $Ca_V\beta_2$-mRFP as template.

Expression and purification of $Ca_V\beta$s. Recombinant $Ca_V\beta$ subunits were expressed in *E.coli* and purified from the soluble fraction of the crude lysate using Ni^{2+}-metal affinity chromatography (HisTrap™, Cytiva), followed by size exclusion chromatography onto a

Superdex-200 16/60 column (Cytiva), as described previously[34]. Both chromatographic steps were done on columns attached to a Fast Performance Liquid Chromatography (FPLC) ÄKTA™ system (ÄKTA™ pure, Cytiva). Eluted fractions from the Superdex-200 column equilibrated with GF-150 buffer (20 mM phosphate pH 8, 150 mM NaCl) for $Ca_V\beta_2$-core wild-type and mutants or with GF-300 (20 mM phosphate pH 8, 300 mM NaCl) for $Ca_V\beta_4$-core and $Ca_V\beta_4$ R482X and the alanine mutants, were pooled, concentrated, flash frozen and stored at -80°C until use. Rabbit skeletal muscle actin protein was prepared and polymerized according to the manufacturer's instructions (Cytoskeleton, Inc, Denver, CO, USA).

Chemical cross-linking reaction and protein digestion. Cross-linking reactions were carried out with $Ca_V\beta_2$-core and polymerised actin. $Ca_V\beta$ protein in GF-150 buffer was centrifuged at 150.000 x *g* for 45 min at 4 °C to remove aggregates. After centrifugation, the supernatant fraction was transferred into a new tube and saved for cross-linking reactions. $Ca_V\beta$ (5 µg) and actin (5 µg) were mixed and incubated at RT for 30 minutes to enable interaction. Either a molar excess of 5x for DSBU or 2.5x for DSSO was added and the reaction mix was incubated for 60 minutes at RT. The reaction volume was 50 µl. After reaction with the cross-linkers, the mixtures were quenched by the addition of Tris-HCl pH 8 to an end concentration of 50 mM. Afterwards, the cross-linking reaction mixtures were analysed by SDS-PAGE. After staining the gel with R-250 Coomassie blue staining solution, the desired bands were excised from the acrylamide gel, dehydrated and stored at -20°C until use. The protein bands were cut in small pieces and reduced with a solution of 20 mM dithiothreitol for 30 min at 56 °C, cooled to RT and then alkylated with 10 mM iodoacetamide for 30 min in darkness. The samples were digested with MS-grade approved trypsin (SERVA, Germany) using an enzyme:protein ratio of 1:50 overnight at 37 °C. Peptides were de-salted using self-made C18 STAGE-Tips[35].

LC-MS/MS analysis. Digested peptides were analysed using an EASY-nanoLC (Thermo) coupled to a Q-Exactive Plus or Orbitrap Eclipse mass spectrometer (Thermo Fisher Scientific) via nanospray source. Peptides were separated with a 50 cm long, self-packed column filled with 1.9 µm C18-AQ Reprosil Pur beads (Dr. Maisch) and the column temperature was maintained at 50 °C using a column oven (PRSO-V2). Peptides were eluted with an effective solvent gradient ranging from 2-35% buffer B within 30 or 60 min.

For DSBU/DSSO-XL identification, digested proteins were analyzed using a HCD/CID-acquisition method. Full scans were recorded at resolution of 70,000 and a scan range from 375-1,750 m/z (AGC 3.6e6, max injection time 20 ms). MS/MS scans were recorded at 35,000 resolution and a scan range from 200-2,000 m/z (AGC 5e5, max injection time 115 ms for CID isolation width 1.9 m/z). Singly and doubly charged ions were excluded from fragmentation since cross-linked peptides tend to occur at a charge state of 3+ or above. All precursors that have been selected for fragmentation were excluded from fragmentation for 20 s.

Cross-link identification. MS raw data were converted to *mzML* format with the program msconvert GUI from ProteoWizard Toolkit version 3[36]. The cross-linked peptide fragments were subsequently identified using Merox v.2.0, MetaMorpheus v.1.0.2 and MaxLynx v.2.2.0.0[37-39]. The MS data in *mzML* format and fasta sequence files for $Ca_V\beta_2$-core (residues 23-422) and actin, corresponding to UniProtKB accession numbers, Q8VGC3-2 and P68135, respectively, were provided and the searches were performed using 10 ppm as precursor, 20 ppm as fragment ion precision, and a False Discovery Rate, FDR of 1%. Fixed modification of cysteine carbamidomethylation and variable modifications of N-terminus acetylation and methionine oxidation were used. Up to three missed cleavages of trypsin were allowed. Inter cross-links identified by at least two software were selected for further analysis. From sixteen cross-links fulfilling this criterion, three were redundant (i.e. identified with both DSBU and DSSO), resulting in a total number of thirteen unique cross-links.

Cross-link Filtering. The thirteen unique inter cross-links identified by MS/MS were examined with the webserver DisVis to check the consistency of the cross-links dataset and quantify the information content of the corresponding distance restraints[40,41]. The identified cross-linked residues map to one narrow cluster on $Ca_V\beta_2$ but to two discrete patches on different accessible surfaces of the actin monomer. However, when considering two adjacent actin subunits they form a continuous patch exposed on one surface of an actin protofilament. Hence, the input files used for DisVis analysis were two adjacent actin subunits (*n* and *n*+2 or chains A and C, respectively, from PDB 5OOE) as fixed chain and $Ca_V\beta2$ (PDB 5V2P) as scanning chain[42,43]. Distance restraints were defined considering that the $Ca_V\beta_2$/actin XLs can be formed with either monomer of the two adjacent actin subunits, resulting in 26 XL-derived distance restraints, with allowed distance range between 0 and 30 Å, to consider the Lys side chain length and its flexibility plus the cross-linker length. Four consecutive DisVis filtering steps were performed; in each iteration, restraints with Z-score larger than 1.0 (and thus high probability to be false positives) were discarded and the remaining restraints were used as input for the subsequent DisVis calculation. This iterative procedure resulted in a set of ten DisVis-filtered distance restraints from XL-MS data that were used to guide the protein-protein docking with the HADDOCK 2.4 webserver[44,45].

Bioinformatic predictions. The XL-derived distance restraints are long range (~30 Å). Thus, additional information on the putative interfaces can help to guide the docking, e.g. from bioinformatics predictions[46-48]. First, we used NACCESS to identify residues that have solvent accessibility ≥ 40% in each of the individual proteins[49]. Then, the list of NACCESS residues was filtered with DisVis using a complete scanning with the aforementioned dimeric actin and $Ca_V\beta_2$ structures and the set of 10 XL-derived distance restraints[40,41]. Residues predicted to have an interaction fraction larger than 1.0 in each protein were kept. However, for $Ca_V\beta_2$ such filtering yielded only putative interacting residues in the GK domain, due to the XL-derived

distance restraints being all located in this domain. Therefore, prediction of additional putative protein-protein interface residues in the $Ca_V\beta_2$ SH3 domain, as well as actin, was carried out using CPORT[50]. The list of CPORT-predicted actin residues was manually curated to select residues belonging to the same side of the filament where the cross-linked residues are located. The manually curated list of CPORT residues for $Ca_V\beta_2$ SH3 and actin, as well as the DisVis-filtered list of NACCESS residues for $Ca_V\beta_2$ GK and actin, were used as active residues for the information-driven docking of the two proteins.

Protein-protein docking. $Ca_V\beta_2$ (PDB 5V2P) or $Ca_V\beta_4$ (PDB 1VYV) and a dimeric structure of actin (extracted from PDB 5OOE) were used for the XL-MS guided protein-protein docking with the HADDOCK 2.4 webserver[44,45]. Distance restraints were defined employing a hybrid protocol[30,42,43]. Unambiguous restraints were defined using the aforementioned DisVis-filtered distance restraints between $Ca_V\beta_2$ and actin, allowing a Cα-Cα distance between cross-linked residues between 0 and 30 Å. In addition, ambiguous restraints were defined using as active residues the bioinformatics predicted residues, as explained in the previous section[40,41]. Additionally, a center of mass restraint was included to enforce the contact between the two partners. The docking calculation comprises three stages: (i) rigid body docking to generate 1,000 protein-protein complex structures; (ii) semi-flexible simulated annealing simulation with flexible interface residues to refine the 200 best scored poses; and (iii) a final refinement with a 2.5 ns molecular dynamics simulation in water in which the two proteins are fully flexible. The final 200 docking structures were clustered based on their protein-protein interface RMSD (i-RMSD) using a 7.5 Å cutoff and the resulting clusters were ranked based on the average HADDOCK score of their top four members.

The cluster with the best average HADDOCK score was selected for further analysis. The docking structures within this top cluster were first checked for their consistency with the XL-derived distance restraints by calculating the Cα-Cα distance for each of the $Ca_V\beta$–actin pairs. Then, the residue contact frequency was evaluated as the number of structures of the top cluster in which residue *i* of one protein partner is within 5 Å of the other protein in the complex and normalized by the total number of structures belonging to the top cluster. The assumption is that residues with higher contact frequencies have higher probability to actually be at the protein-protein interface, as done in references[50,51]. The electrostatic potential of each protein partner was calculated using the APBS webserver and the corresponding crystal structures[52].

Computational alanine scanning (CAS). The top four structures of the best scored cluster produced by HADDOCK 2.4 were analysed using CAS to predict putative hotspots (i.e. residues at the $Ca_V\beta$/actin interaction surface contributing the most to the binding energy of the complex). A set of six different webtools were used to calculate the change in binding free energy upon Ala mutation (ΔΔG); three of them are based on empirical energy functions (Anchor, Robetta and the BUDE implementation in BAlaS), and the other three on machine

learning trained statistical potentials (BeAtMuSiC, Mutabind2 and SAAMBE-3D)[53-59]. Residues were ranked according to the ΔΔG values averaged over the four docked structures analysed (to account for protein flexibility) and then over the six webtools used (to obtain a consensus prediction).

In vitro F-actin co-sedimentation assay. The F-actin co-sedimentation assay was performed according to the manufacturer's instructions (except that Tris-HCl was replaced by HEPES in the polymerization buffer) and as previously described[31,32]. Actin was polymerized by incubation in actin polymerizing buffer containing (in mM): 5 HEPES, 0.2 $CaCl_2$, 50 KCl, 2 $MgCl_2$, 1 ATP, pH 8.0. The desired recombinant $Ca_V\beta$ proteins were incubated with polymerized actin in polymerization buffer in a 50 µl reaction, followed by high-speed centrifugation for 20 min at 150.000 x *g*, 4 °C. The supernatant and pellet fractions were recovered and resolved by denaturing SDS-PAGE. In control reactions, $Ca_V\beta$ alone was subjected to centrifugation, followed by recovery of supernatant and pellet fractions and denaturing SDS-PAGE to quantify pelleting of the protein in the absence of actin. Phalloidin was used in all experiments at a concentration of 25 µM to stabilize actin filaments. Raw intensities of the protein bands were estimated by densitometry using the Fiji ImageJ software[60]. Association of $Ca_V\beta$ proteins with F-actin was reported as the fraction of $Ca_V\beta$ bound, calculated from the ratio of band intensities of the protein found in the pellet over the total protein (i.e. protein found in supernatant and pellet).

Pull down assays. Either GST fused to the AID peptide (GST-AID) or GST alone, as negative control, were used as bait in a standard GST pull down assay as described[61]. Briefly, GST-AID or GST were immobilized onto glutathione-sepharose beads and then incubated with the desired $Ca_V\beta$ constructs at room temperature. After several washing steps, the bound proteins were eluted with SDS-loading buffer and resolved in SDS-PAGE.

Intrinsic fluorescence spectroscopy. Intrinsic fluorescence experiments were performed using a FS5 Fluorescence Spectrometer (Edinburgh Instruments, UK) equipped with 500 µl cuvette coupled to a SC-25 temperature holder and a TC-1S temperature controller (Quantum Northwest, USA). Excitation was done at 280 nm in steps of 1 nm over a range of temperatures between 20 °C and 74 °C and the emission spectra were recorded at 300–430 nm in steps of 1 nm. For data analysis, the spectral center of mass (CM) was determined as follows, and plotted against the temperature:

$$CM_i = \frac{\sum_i F_i \lambda_i}{\sum_i F_i} \qquad \text{(Eq. 1)}$$

Where F is the fluorescence intensity and λ the wavelength at a temperature i. The transition temperatures were then obtained by non-linear regression fitting using a two-state transition model:

$$y = \frac{\alpha_n + \beta_n T}{1 + e^{\frac{4T_m(T-T_m)}{T\Delta T}}} + \frac{\alpha_d + \beta_d T}{1 + e^{\frac{4T_m(T_m-T)}{T\Delta T}}} \quad \text{(Eq. 2)}$$

Where *y* is CM, *α* and *β* are the *y* intercept and slope of the native (*N*) or denatured (*D*) states respectively, *T* the temperature, T_m the transition temperature, ΔT the width of the transition and *e* the exponential function.

Cell culture and transfection. HEK293 cells were cultured in Dulbecco's modified Eagle medium (DMEM) supplemented with 10% fetal bovine serum (Sigma-Aldrich), L-glutamine (2 mM), and incubated in a 5% CO_2 atmosphere. For electrophysiological experiments, cells were seeded onto 50 mm dishes and transfected using Lipofectamine 2000 (Thermo Fisher Scientific) following the manufacturer's instructions using 3 µg and 1 µg of $Ca_V1.2$-mNeonGreen and $Ca_V\beta$-mRFP expressing constructs, respectively. For western blot analysis, the same protocol was followed except that cells were transfected only with wild-type and mutant $Ca_V\beta$-mRFP expressing constructs. For laser scanning confocal fluorescence microscopy, HEK293 cells were seeded onto 35 mm glass-bottom dishes (µ-Dish ibidi) and transfected with 2 µg of the corresponding plasmids using Lipofectamine 2000 (Thermo Fisher Scientific).

Western blot analysis of cell lysates. Cells were lysed using RIPA buffer supplemented with a protease inhibit cocktail (Sigma-Aldrich). Lysates were subjected to centrifugation and the supernatant was collected and resolved by SDS-PAGE. Proteins were then electrically transferred onto nitrocellulose membrane (GE Healthcare, Life Science) for 1 h. Membranes were blocked using 5% BSA in TBS buffer (10 mM Tris, 150 mM NaCl, pH 7.5) and incubated for immunodetection with anti-CACNB2 antibody (Novus Biologicals) or anti-GADPH (Sigma). After several washes, membranes were incubated with a goat anti-rabbit IgG HRP-conjugated secondary antibody (Pierce). Protein detection was performed using a chemiluminescent detection kit (SuperSignal West Femto Chemiluminescent Substrate, Thermo Scientific).

*Laser scanning confocal fluorescence microscop*y. Confocal imaging was performed 24 hours after cell transfection on a Leica inverted confocal microscope using a 63x/1.4 NA oil immersion objective (Nikon). Cells were excited with a 543 nm HeNe laser to visualize the wild-type and mutant $Ca_V\beta_2$ constructs fused to mRFP ($Ca_V\beta_2$-mRFP and $Ca_V\beta_2$ 8Ala-mRFP). The emitted light was monitored at 550–625 nm. Images were exported, formatted and the brightness was adjusted using Fiji ImageJ[60].

Electrophysiology. Whole-cell patch clamp recordings from cells transiently co-expressing $Ca_V1.2$-mNeonGreen with either wild-type $Ca_V\beta_2$ or $Ca_V\beta_2$ 8Ala mutant were performed 24 hours after transfection using the EPC-10 amplifier equipped with the PatchMaster software (HEKA Elektronik). $Ca_V1.2$ was fused to mNeonGreen and $Ca_V\beta_2$ constructs to mRFP to enable recognition of transfected cells. Recordings and analysis were done in a blind fashion

with respect to the $Ca_V\beta_2$ construct used. Ionic currents were elicited by 60 ms duration voltage steps from +50 mV to +70 mV in 5 mV increments from a holding potential of -90 mV and using Ba^{2+} as charge carrier. Gating currents were recorded during voltage steps near the reversal potential for Ba^{2+} which was determined empirically by stepping to different potentials in 2 mV increments[33,62]. The total charge movement was obtained by integrating the On gating current elicited at the reversal potential for Ba^{2+} over time. Borosilicate glass patch pipettes (Harvard Apparatus) were pulled using a Sutter P-1000 puller (Harvard Apparatus) and fire-polished using a Narishige MF-830 microforge. Patch pipettes with electrical resistances between 1.0–2.0 MΩ were used. Series resistance compensation was applied, resulting in a voltage error of less than 5 mV. The pipette solution contained (in mM): 135 cesium-methanesulfonate, 10 EGTA, 5 CsCl, 1 $MgCl_2$ and 10 HEPES, with the pH adjusted to 7.3 with CsOH. The extracellular recording solution contained (in mM): 140 tetraethylammonium-MeSO3, 10 $BaCl_2$ and 10 HEPES buffer, with the pH adjusted at 7.3 with tetraethylammonium hydroxide. Data was analysed with Python 3.8 version using common libraries including numpy, pyplot, scipy, seaborn and pandas and presented as the mean ± SEM. Differences between data sets were analysed using t-test.

The voltage dependence of activation is described by the plot of the relative open probabilities ($P_{open}(V)$) versus voltage. $P_{open}(V)$ were calculated by normalizing each steady-state current amplitude to the maximal value (I/Imax) and fitted to a Boltzmann function to obtain the half-activation voltage ($V_{1/2}$), Equation 3.

$$P_{open}(V) = \frac{1}{1 + e^{\frac{-(V_m - V_{1/2})}{k}}} \qquad \text{(Eq. 3)}$$

where V_m is the membrane potential, V_{rev} is the reversal potential and k the slope.

Stationary noise variance analysis. The analysis of the variance (σ^2) of the mean macroscopic current (‹I›) of repeated current recordings obtained at different voltages was performed as described[63]. Currents were elicited by 150 ms duration voltage steps from +50 mV to +70 mV in 5 mV increments from a holding potential of -90 mV and using Ba^{2+} as charge carrier. This analysis was done for each cell in order to compute the number of functional channels (n) and the unitary conductance (γ). The ionic current recorded through a defined population of ion channels is a function of the number of functionally available channels (n), the single-unitary current (i) and the probability to be found in the open state (Po) (Eq. 4).

$$I = n \times i \times Po \qquad \text{(Eq. 4)}$$

Considering a fixed unitary channel conductance (γ) that has been shown for Ca_Vs[64-66], the current through a single channel (i) varies then linearly with the membrane potential (V_m) and equals the γ times the driving force (V_m - V_{rev}), where V_{rev} is the reversal potential according to Eq. 5.

$$i = \gamma(V_m - V_{rev}) \qquad \text{(Eq. 5)}$$

In such a case, the relationship between the variance and the mean macroscopic current (‹I›) is defined then by the following equation (Eq.6)[63]. The number of functionally available channels, n and the unitary conductance γ were obtained by fitting the data to Eq. 6.

$$\frac{\sigma^2}{\langle I\rangle(V_m - V_{rev})} = -\frac{1}{n}\left(\frac{\langle I\rangle}{V_m - V_{rev}}\right) + \gamma \qquad \text{(Eq. 6)}$$

Having determined n (from Eq. 6), i was readily computed from Eq. 5 and the maximum open probability of the channel (Po_{max}) was obtained from Eq. 4 for the value of the maximal current amplitude (I_{max}) as stated in Eq. 7.

$$Po_{max} = \frac{I_{max}}{n \times i} \qquad \text{(Eq. 7)}$$

The values for the three parameters, n, γ and Po_{max}, obtained from the original set of data (n=10, number of cells) were subjected to bootstrap iterations[67] where 10 random samples with replacements are taken from the original set of 10 measurements, generating a synthetic set of for each parameter. This procedure was repeated 500.000 times and the reported values are given by the mean value and SD. Differences between data sets were analysed using Bootstrapped t-test.

Results

Chemical cross-linking and identification of cross-linked peptides by mass spectrometry. Chemical cross-linking combined with mass spectrometry (XL-MS) was performed to map the contact surface between recombinant $Ca_V\beta_2$ and *in vitro* polymerized actin. Given that recombinant full-length $Ca_V\beta$ proteins are less stable than their corresponding core regions counterparts, we here employed $Ca_V\beta_2$-core which is more stable under the lower salt conditions used for actin polymerization[26,31]. $Ca_V\beta_2$-core elutes as a monodisperse peak from the size exclusion chromatography column and no signal of protein aggregation was visible (Figure 1A-B).

Two different MS-cleavable cross-linkers, DSSO and DSBU, with a spacer arm of 10.3 Å and 12.5 Å, respectively, were employed reacting both mainly with lysine residues but also with

serine, threonine and tyrosine residues. In control reactions, either $Ca_V\beta_2$-core (48.2 kDa) alone or actin (43 kDa) alone were incubated with the cross-linkers (Figure 1C-D). The cross-linked proteins were resolved by SDS-PAGE and excised from the gel for further analysis.

Although, the efficiency of the cross-linking reaction for $Ca_V\beta_2$-core and actin was low, sufficient inter cross-linked products were obtained with DSBU as well as for DSSO. In both cases, a product with an apparent molecular mass of about 110 kDa that was fully absent in control reactions, suggesting the formation of inter-molecular chemical links between $Ca_V\beta_2$-core and actin, was excised from the gel and analysed (Figure 1C-D).

Identification of the cross-linked peptides between $Ca_V\beta_2$-core and actin was performed by nano LC-MS/MS and the data were analysed with three software packages, MaxLynx, Merox and MetaMorpheus, as described in Material and Methods[37-39]. A total of 30 inter-molecular cross-links were identified using DSSO and DSBU and the ones identified by at least two software were further selected resulting in a total of 13 non-redundant cross-links (Supplementary Table 1). The residues involved in cross-links between $Ca_V\beta_2$ and actin narrowly cluster on $Ca_V\beta_2$-GK domain (K347, K354, K358 and K362), while they distribute within two discrete patches on different regions in one actin monomer (S62 and K63 in one cluster and K293, K317, K328 and K330 in the other one). However, these two clusters form a contiguous patch in the surface of two adjacent actin subunits within an actin protofilament (Figure 1E). Applying DisVis software to evaluate the information content of the 13 XL-MS derived distance restraints showed no consistency with all 13, but with a set of ten conforming restraints, which reduced the accessible interaction space to 0.7 % of the full interaction space (Figure 1E-F and Supplemental Table S2)[40,41].

Structural model of the interaction between $Ca_V\beta$ and actin

Docking-based modeling of the biomolecular interaction between $Ca_V\beta_2$ and actin was performed with the HADDOCK 2.4 webserver[44,45]. As described in Material and Methods, we used the XL-MS distance constraints resulting from DisVis analysis and the interface information predicted with bioinformatics.

All generated $Ca_V\beta_2$/actin models were clustered using their protein-protein interface RMSD (i-RMSD) and the resulting clusters were ranked according to the average HADDOCK score (Supplemental Table S3 and Supplemental Figure S1A). The best scored cluster, populated with 190 models, was selected for further analysis. No violations of the maximum-bound of 30 Å between Cα-Cα of two cross-linked residues were observed in all 190 models, except for one $Ca_V\beta$-actin pair (K358-K317), where a fraction of the complexes exceeds the distance cut-off up to 35 Å (Supplemental Figure S1B). Maximum Cα-Cα distances of 35 Å have been considered before to account for conformational flexibility and ambiguity in the cross-link assignment[68-71].

The top scoring model for the protein-protein complex illustrates that $Ca_V\beta_2$ fits on a hollow formed by two adjacent actin monomers of one protofilament (Figure 2A). The protein-protein interaction interface between $Ca_V\beta_2$ and actin was defined by mapping the contact frequency of each residue of the protein complex onto the corresponding three-dimensional structures. The residues with the largest contact frequency form a continuous patch in $Ca_V\beta_2$ extending both the SH3 and GK domains and in actin both monomers (Figure 2B). The GK domain establishes contacts with subdomains SD1 and SD3 of one actin subunit, whereas the SH3 domain interacts with residues distributed along subdomains SD1 and SD2 in the neighbouring actin monomer (Figure 2).

Calculation of the electrostatic potential surface of $Ca_V\beta_2$ and actin shows a positive-charged patch on $Ca_V\beta_2$ binding surface, mainly located in the GK domain, which matches a dominant negative charge distribution on the actin interaction surface, suggesting electrostatic binding complementarity (Figure 2C).

To examine the contribution of electrostatic interactions, we measured the dependence of $Ca_V\beta_2$/ actin complex formation on ionic strength. Binding of $Ca_V\beta_2$-core to actin at different NaCl concentrations, ranging from 30 mM to 150 mM, was assessed by F-actin co-sedimentation assay, a widely used method for analysing association of proteins with actin[72,73]. To avoid discrepancies arising from effects of the different salt concentrations on actin polymerization, phalloidin was used to stabilize actin. $Ca_V\beta_2$-core was incubated with *in vitro* polymerized actin and, after high-speed centrifugation, the pellet and supernatant fractions were resolved by SDS-PAGE. In control reactions, $Ca_V\beta_2$-core alone is centrifuged and the recovered fractions also resolved by SDS-PAGE (Figure 3).

$Ca_V\beta_2$-core alone is virtually excluded from the pellet fraction at all NaCl concentrations tested in control reactions (Figure 3A, bottom panel). However, the fraction of $Ca_V\beta_2$-core co-sedimenting with actin decreased steadily with increasing NaCl concentrations and, at the highest NaCl concentrations used, no $Ca_V\beta_2$-core protein was detected in the pellet (Figure 3 and Supplemental Figure S2). Thus, binding of $Ca_V\beta_2$ to actin depends on the salt concentration, validating that electrostatic interactions indeed contribute to the binding stability of $Ca_V\beta_2$/actin complex.

Identification of hotspots residues at $Ca_V\beta_2$/actin interaction interface.

Residues at $Ca_V\beta_2$ contributing predominantly to the protein-protein binding energy, the so-called hotspots, were predicted by computational alanine scanning using six different webservers (Anchor, Robetta, BUDE, BeAtMuSiC, Mutabind2 and SAAMBE-3D)[53-59]. The change in free energy (ΔΔG) due to alanine substitution of each $Ca_V\beta_2$ residue at the protein-protein interface was calculated as an average over the top four structures of the best cluster for each of the six predictors (Supplemental Figure S3A-F). Then, the ΔΔG values were

averaged over all six predictors and the resulting consensus ΔΔG values were used to rank the $Ca_V\beta_2$ residues as hotspots (Supplemental Figure S3G). The top seven ranked predicted hotspots residues in crystallographic resolved segments at the $Ca_V\beta_2$ interaction surface were further selected for experimental validation (Figure 4A). Two of these seven identified hotspot residues are located on the SH3 domain (K90 and R128) and five on the GK domain (K347, Q350, K354, K358, and N365). In addition, we observed that L364, the top ranked hydrophobic residue in the GK domain, lies within the hotspot region (Figure 4A).

We investigated the functional role of the hotspot residues by substituting them in $Ca_V\beta_2$-core by alanine. Two different $Ca_V\beta_2$-core mutant proteins, $Ca_V\beta_2$-core 8Ala and $Ca_V\beta_2$-core 6Ala, bearing alanine substitutions either at all eight predicted hotspots (GK+SH3) residues or at the six located on the GK domain, respectively, were generated (Figure 4B). The amino acid substitutions introduced in $Ca_V\beta_2$-core do not destabilize the mutant proteins, as judged by the lack of aggregates and monodispersity of the peaks eluting from the size-exclusion column (Figure 4B).

F-actin co-sedimentation assays were used to compare the ability of the wild-type (WT) and mutant proteins to interact with F-actin. In control reactions, negligible amounts of $Ca_V\beta_2$-core WT as well as of mutant proteins were found in the pellet after high-speed centrifugation (Figure 4C, lanes 3, 8 and 12). In the presence of actin, the fraction of $Ca_V\beta_2$-core that co-sedimented was significantly reduced for the mutant proteins (Fraction bound = 0.11 ± 0.03 for $Ca_V\beta_2$-core 6Ala, 0.09 ± 0.02 for $Ca_V\beta_2$-core 8Ala and 0.24 ± 0.03 for $Ca_V\beta_2$-core WT, Figure 4D and Supplemental Figure S4A-E).

To discard the possibility that the reduced actin binding activity observed for $Ca_V\beta_2$-core hotspots mutants was due to differences in the stability of the proteins in the F-actin co-sedimentation assay buffer, we compared their intrinsic fluorescence. Minute differences in the thermal unfolding curves and unfolding transition temperature (T_m) were observed among $Ca_V\beta_2$-core WT and mutant proteins, indicating comparable structural stabilities in the assay buffer (Supplemental Figure S4F).

Altogether, these results prove that the computationally predicted hotspots in the $Ca_V\beta_2$ interaction surface with actin significantly contribute to complex formation *in vitro*.

Previous results suggesting that $Ca_V\beta$ can associate simultaneously with actin and the $Ca_V\alpha_1$ high-affinity AID site anticipate that the actin association deficient $Ca_V\beta_2$ mutants might preserve binding capability to AID[32]. Accordingly, the eight identified $Ca_V\beta_2$ hotspots that are relevant for binding to actin show no steric clashes with the hotspots for interacting with AID[29,74] (Supplemental Figure S5A). Moreover, pull down assays using as bait the AID peptide fused to GST demonstrate that both mutants, $Ca_V\beta_2$-core 6Ala and $Ca_V\beta_2$-core 8Ala, still associate with AID peptide, underlying the idea that $Ca_V\beta_2$ association with actin and AID is not mutually exclusive (Figure 4E Supplemental Figure S5B).

Integrating $Ca_V\beta_2$-derived XL-MS data for computational docking of $Ca_V\beta_4$ and actin

$Ca_V\beta_4$, the central component of the Ca_V complex in human brain, also associates with actin[32]. Amino acid alignment with $Ca_V\beta_2$ shows conservation of all four lysine residues involved in the XL-MS-based distance restraints used for modelling $Ca_V\beta_2$/actin interaction (Supplemental Figure S6). Therefore, we exploited the analogous restraints, together with bioinformatics-based predictions of interfacial residues, to guide molecular docking for $Ca_V\beta_4$ and actin.

The best scored cluster for the HADDOCK-generated $Ca_V\beta_4$/actin complex is populated with 157 models, with Cα-Cα distances between two crosslinked residues < 35 Å (Supplemental Table S3 and Supplemental Figure S7).

Structural comparison of the HADDOCK models for the $Ca_V\beta_4$/actin and $Ca_V\beta_2$/actin complexes yielded a backbone RMSD of 3.1 Å between the two bound $Ca_V\beta$s with respect to the actin dimer reference, indicating a relatively high degree of structural similarity[75] (Figure 5A).

Computational alanine scanning for $Ca_v\beta_4$/actin interaction identified as hotspots a number of residues including the eight amino acids analogous to the ones in $Ca_V\beta_2$ proven to affect binding to actin (Supplemental Figure S8).

The predicted hotspots mutations were introduced in the background of the carboxyl-terminally truncated naturally occurring mutant of $Ca_V\beta_4$, $Ca_V\beta_4$ R482X, that turn out to display higher *in vitro* apparent affinity for actin as compared to its $Ca_V\beta_4$-core counterpart (Supplemental Figure S9A-B). Although its etiology remains unclear, $Ca_V\beta_4$ R482X has been associated with juvenile myoclonic epilepsy[7,8,76].

By analogy to $Ca_V\beta_2$, the two $Ca_V\beta_4$ R482X mutants containing substitutions by alanine in either all eight hotspots residues ($Ca_V\beta_4$ R482X 8Ala) or in the six located within the GK domain ($Ca_V\beta_4$ R482X 6Ala) were generated (Figure 5B).

Size exclusion chromatography profiles supported the structural integrity of the recombinant $Ca_V\beta_4$ R482X and the hotspot $Ca_V\beta_4$ R482X Ala mutant proteins (Figure 5B). Furthermore, the intrinsic fluorescence measurements of $Ca_V\beta_4$ R482X and $Ca_V\beta_4$ R482X Ala mutants in actin co-sedimentation assay buffer showed statistically undistinguishable unfolding transition temperatures (Supplemental Figure S9C).

However, binding of $Ca_V\beta_4$ R482X Ala mutants to actin was dramatically altered. While more than 80% of the total $Ca_V\beta_4$ R482X protein amount distributes in the pellet fraction together with actin, only 40% of $Ca_V\beta_4$ R482X 6Ala and less than the 10% of $Ca_V\beta_4$ R482X 8Ala cosediment with actin (Figure 5C-D and Supplemental Figure S10). In control experiments in which the $Ca_V\beta_4$ R482X proteins are centrifuged in the absence of actin they remain almost completely in the supernatant. As for $Ca_V\beta_2$, $Ca_V\beta_4$ R482X and the hotspot mutants preserved their ability to associate with the AID peptide (Figure 5E and Supplemental Figure S9D).

Taken together, these results demonstrate the crucial contribution of the mutated residues to the affinity of $Ca_V\beta_4$ for actin and highlight the agreement between the *in vitro* experimental results and the generated molecular model for $Ca_V\beta$/actin interaction.

$Ca_V\beta_2$ hotspots mutant reduces the number of functionally available L-type $Ca_V1.2$ channels

We next assessed *in vivo* the effect of the $Ca_V\beta$ mutations that impaired association with actin. To this aim, full-length wild-type $Ca_V\beta_2$ and a mutant protein encompassing the eight experimentally validated hotspots mutations were fused to mRFP to generate a $Ca_V\beta_2$-mRFP fusion constructs, hereinafter referred to as wild-type $Ca_V\beta_2$ ($Ca_V\beta_2$ WT) and $Ca_V\beta_2$ hotspots mutant ($Ca_V\beta_2$ MUT). Laser scanning confocal images of cell expressing either $Ca_V\beta_2$ WT or $Ca_V\beta_2$ MUT show that the mutant protein preserves the well-established plasma membrane localization of wild-type $Ca_V\beta_2$ [77-79] (Figure 6A). Moreover, western blot analysis probed with anti-$Ca_V\beta_2$ of crude cell lysates from cells expressing the wild-type and the mutant protein displayed comparable levels of expression (Figure 6B and Supplemental Figure S11). Thus, hotspot mutations of $Ca_V\beta_2$ affect neither cellular localization nor expression of the protein.

Whole-cell recordings from cells coexpressing $Ca_V1.2$ L-type subunit and $Ca_V\beta_2$ hotspot mutant showed a significant decrease in the magnitude of the average ionic peak current compared to cells expressing $Ca_V1.2$ and $Ca_V\beta_2$ WT (from -3.9 ± 0.26 nA for $Ca_V1.2/Ca_V\beta_2$ WT to -2.5 ± 0.27 nA for $Ca_V1.2/Ca_V\beta_2$ MUT, p = 0.00075) (Figure 6C). This decrease in L-type current was accompanied by only a modest rightward shift in the voltage dependence of activation of about 4 mV in the half-activation voltage ($V_{½}$) (Figure 6C). This suggests that a reduced open probability of the channel does not account for the dramatic reduction in $Ca_V1.2$-mediated ionic current induced by the $Ca_V\beta_2$ hotspots mutant.

Therefore, $Ca_V1.2$ downregulation might be then caused by changes in the other parameters describing the function for the magnitude of the ionic current (Eq. 4-5); a decrease in the number of channels assembled at the plasma membrane or in their unitary conductance, or both.

We first addressed whether or not the cell surface expression of the channel was affected by $Ca_V\beta_2$ MUT. To this aim, we recorded the gating currents from cells coexpressing $Ca_V1.2$ with either $Ca_V\beta_2$ WT or $Ca_V\beta_2$ MUT, as previously described[33,34,62,80].

Gating currents arise from the voltage driven movement of charged residues (gating charges) within the voltage sensor and their integral provides the total charge moved during the voltage step (*Qon*), which is a function of the number of channels assembled into the plasma membrane and the number of charges displaced per channel[81-83].

Qon calculated for $Ca_V1.2$ coexpressed with either $Ca_V\beta_2$ WT or $Ca_V\beta_2$ MUT did not differ significantly from each other showing that impaired association of $Ca_V\beta_2$ with actin did not compromise the total expression of $Ca_V1.2$ channels at the cell surface (p = 0.19) (Figure 6D). To gain insight about the single channel-properties, we conducted stationary noise variance analysis of macroscopic currents that provides also information on the number of functionally available channels [84,85].

The fluctuations in the whole-cell current were computed for repeated current recordings at different voltages from cells coexpressing $Ca_V1.2$ with either $Ca_V\beta_2$ WT or $Ca_V\beta_2$ MUT, as described[63]. The plot of the variance (σ^2) as a function of the mean macroscopic current ($\langle I \rangle$) yield a straight line (Eq. 6) from which the number of functionally available channels n and the unitary conductance γ are calculated directly from the slope and y-intercept, respectively (Figure 7A).

The box plots with superimposed data points from all analysed cells show that the average value for n calculated for cells coexpressing $Ca_V1.2$ with $Ca_V\beta_2$ MUT is significantly smaller than the one obtained for cells expressing the wild-type subunit combination (Figure 6B). Using Bootstrap method[67], the mean n obtained from the bootstrap sample distributions was 11,779 ± 1,250 for $Ca_V1.2$ /$Ca_V\beta_2$ WT and 6,843 ± 1,424 for $Ca_V1.2$ /$Ca_V\beta_2$ MUT (p =0.009). In contrast, non-significant difference in γ (p = 0.66) and maximum open probability of the channel ($Po_{max,}$ calculated from equation Eq. 7, p = 0.29) between $Ca_V1.2$ channels complexed with $Ca_V\beta_2$ WT or $Ca_V\beta_2$ MUT was found (Figure 6B). Moreover, the extent of reduction of 42% in the number of channels closely matches the decrease by 36% of the average macroscopic peak current caused by $Ca_V\beta_2$ hotspots mutant as compared with the wild-type protein.

Since gating currents recordings showed no differences in the total number of channels at the plasma membrane, these results suggest that $Ca_V\beta_2$ MUT promotes colonization of the plasma membrane by non-functional or defective channels with an intact voltage sensor.

Discussion

Protein-protein interactions are involved in almost every biological process, both in health and disease. Unveiling the contact surfaces of PPIs advances our understanding of the underlying molecular mechanisms controlling cell function and dysfunction and enables their intervention. In this study, we identified the PPI interface between $Ca_V\beta$ and actin by means of cross-linking mass spectrometry and protein-protein docking. We generated $Ca_V\beta$ hotspots mutants with reduced capacity to bind actin and subsequently evaluated their functional impact. The interaction interface between $Ca_V\beta$ and actin displays electrostatic complementary that was confirmed by the sensitivity of the binding reaction to ionic strength. Electrostatic interactions between actin binding proteins and the negatively charged actin surface have been frequently observed[73,86]. Furthermore, the model for $Ca_V\beta$/actin complex presented here is consistent with

in vitro assays that showed that both, the SH3 and GK domains of $Ca_V\beta$ bind to actin and that the association of $Ca_V\beta$ with actin and the AID peptide are not mutually exclusive[31,32].

$Ca_V\beta_2$ hotspots mutant induced a significant decrease in the macroscopic current mediated by $Ca_V1.2$ with a reduction in the number of $Ca_V1.2$ channels evaluated by noise analysis but without alterations in the cell surface density of $Ca_V1.2$ assessed by gating currents measurements.

Unless the gating charges are not intact, gating currents compute the total number of channels expressed at the cell surface, independent of their competence to mediate ionic currents[83]. In contrast, noise variance analysis of the macroscopic currents provides information about the number of functionally competent channels, i.e, channels that are available for activation, and their single channel-properties[84]. Silent channels contribute neither to the macroscopic current nor to the fluctuations in the macroscopic current around its mean value (variance).

Therefore, using a combination of gating currents and stationary noise analysis, we determined that the $Ca_V1.2$ current reduction triggered by $Ca_V\beta_2$ MUT can be accounted for by a decrease in the number of functionally available $Ca_V1.2$ channels with no alterations in the single-channel properties of the remaining channels. Worth noting is that the smaller unitary conductance value for $Ca_V1.2$ reported here could be attributed to the absence of Ca_V agonists, such as Bay K8644, in our whole cell current recordings[87,88].

The fact that the extent of $Ca_V\beta_2$ MUT-induced reduction in the number of functionally competent channels is comparable to the decrease in the average macroscopic peak current and no changes in Po or conductance were observed argues in favour as solely mechanism responsible for current reduction.

Still, a conceivably but very unlikely scenario is that $Ca_V\beta_2$ MUT stabilizes a low Po or silent gating mode[64,87,89]. This mode of action has been reported for Rem GTPase inhibition of $Ca_V1.2$ mediated currents[90]. Although, we cannot unambiguously discard the existence of an unprecedented long-lived low or silent gating mode in $Ca_V1.2$ channels complexed with $Ca_V\beta_2$ MUT, all the experimental evidence published so far shows that $Ca_V\alpha_1$, not $Ca_V\beta$, encodes the gating modes, that $Ca_V\beta$ lacks the ability to affect the proportion of the different gating modes or create new ones, and that it facilitates pore opening, among others, by increasing the fraction of time that the channel spent in the open state within the already existing highly open mode[91-93].

Therefore, we conclude that the acquisition of non-conducting attributes of $Ca_V1.2$ induced by $Ca_V\beta$ MUT, and the subsequent decreased ionic current, results from the accumulation of functionally damaged silent channels. This suggests a role of $Ca_V\beta$/actin interaction in the channel´s endocytic quality control process that is responsible for maintaining proteins in their native, functional conformation. Conformationally damaged proteins are recognized, endocytosed and either degraded or repaired and then reinserted into the plasma membrane

via recycling[94-96]. The impact of $Ca_V\beta$/actin association in regulating the endocytic quality control of $Ca_V1.2$ channels at the cell surface agree with previous findings demonstrating a crucial role of $Ca_V\beta$ and the actin cytoskeleton in the endocytic recycling of the channel[33,97].

As expected from the high degree of sequence homology and three-dimensional structure similarity among $Ca_V\beta$s, our data on $Ca_V\beta_2$ and $Ca_V\beta_4$ show conservation between their PPI interfaces with actin. Computational alanine scanning revealed a set of eight hotspots located in the SH3 and GK domains, shared by $Ca_V\beta_2$ and $Ca_V\beta_4$, that reduces the *in vitro* affinity for actin upon mutation to alanine. However, the lack of structural data for the variable N- and C-terminal and HOOK regions in the crystal structures of $Ca_V\beta$ prevents the assessment of the contribution of these segments to the interaction[28-30,42]. It has been proposed that context-specific PPI networks determine the functional outcome across cellular types and that intrinsically disordered regions are important in mediating molecular recognition in protein interaction networks and establishing interactions with various partners enabling regulation of diverse cellular activities[98,99]. Thus, the unstructured variable regions of $Ca_V\beta$ may as well serve the rewiring of protein interactions adapting the biological response to the cellular condition in normal and diseased states.

We here found that the premature-termination $Ca_V\beta_4$ R482X mutant associated with juvenile myoclonic epilepsy (lacking 38 amino acids at the C-terminus) exhibit an apparent higher *in vitro* affinity for actin than $Ca_V\beta_4$-core (devoid of the N- and C-terminal segments). This result supports the notion that the variable regions of this protein play a role in fine-tuning this interaction.

Unfortunately, direct comparison of *in vitro* experimental affinities for $Ca_V\beta_4$ R482X and $Ca_V\beta_4$ wild-type was unviable, because the high salt concentration required for the stability of the full-length recombinant $Ca_V\beta_4$ would preclude actin binding. $Ca_V\beta_4$ R482X exhibits a modest effect on Ca_V permeation that is insufficient to account for the diseased condition suggesting that a channel unrelated function may be the cause[7]. It becomes then interesting to investigate in the future whether or not aberrancies in the $Ca_V\beta_4$ R482X/actin PPI play a role in the onset of the disorder. So far, we have shown that $Ca_V\beta_4$/actin interaction increases synaptic strength independent of $Ca_V\beta_4$ association state with the channel complex[32].

Aberrant PPIs are linked to several human diseases and they are emerging rapidly as pharmacological targets for therapeutic treatment of such conditions[100-105]. In this context, our findings introduce a new PPI with potential application as a target for peptidomimetic approaches in $Ca_V1.2$-associated dysfunctions, and offer an alternative framework to advance our knowledge into the etiology of $Ca_V\beta$-associated genetic disorders. Ultimately, our results provide new insights into the life cycle of voltage-gated calcium channels by revealing a molecular interaction contributing to maintain functionally fit channels at the cell surface. We discover that an intact $Ca_V\beta_2$/actin interaction supports the clearance of defective channels

from the plasma membrane, and in turn, maintains the integrity of the cell membrane, by regulating their quality control system.

Data availability

The mass spectrometry raw and search data have been deposited to the ProteomeXchange Consortium (http://proteomecentral.proteomexchange.org) via the PRIDE partner repository[106] with the dataset identifiers PXD044723 and PXD044630 for DSBU and DSSO derived data respectively.

Data needed to reproduce the docking results shown in this paper (HADDOCK distance restraint files) and resulting Ca_Vβ-F-actin complex models are available at Zenodo (https://doi.org/10.5281/zenodo.8276447).

Acknowledgements

We thank Marcus Krüger and Andreas Schmidt (CECAD, University of Cologne, Germany) for Orbitrap mass spectrometry measurements. We are very grateful to Prof. Christoph Fahlke and Prof. Alan Neely for helpful discussions.

Author contributions

FC, performed, designed, acquired most of the experiments. Analysed all data collected for mass spectrometry, protein-protein docking, in vitro cross-linking and binding assays and western blots, performed protein expression and purification and laser scanning confocal microscopy images; prepared the figures for the manuscript; VL, designed, performed, recorded and analysed all the electrophysiological experiments and prepared the corresponding figures. EM, molecular biology and discussion; NJ, generation of cDNA constructs, protein expression and purification, cell culture; PFH, mass spectrometry discussion; BSS, design, analysis and discussion mass spectrometry; MAP, design, analysis and discussion computational biology; P.H. conceived the project, designed experiments and wrote the manuscript.

Competing interests Statement

The authors declare that they do not have any competing interests, either financial or non-financial.

Funding

Networking doctoral candidates (Vernetzungsdoktoranden) program, Forschungszentrum Jülich.

Figure Legends

Figure 1. **Chemical cross-linking mass spectrometry (XL-MS) and computational analysis define a set of distance constraints for modeling $Ca_V\beta$/actin complex**. **A**, Schematic linear representation of the domain architecture (top) and crystal structure (bottom) of the rat $Ca_V\beta_2$ (UniProtKB Q8VGC3-2; PDB 5V2P). The Src homology 3 (SH3) and guanylate kinase (GK) domains, highly conserved among the members of the $Ca_V\beta$ family, are labeled. **B**, Size-exclusion chromatography profile of $Ca_V\beta_2$-core in GF-150 buffer containing 20 mM sodium phosphate, 150 mM NaCl, pH 8.0. The inset shows the purified protein resolved onto a reducing SDS-PAGE. Numbers denote the molecular masses of molecular weight standards. **C**, SDS-PAGE analysis of DSSO cross-linked $Ca_V\beta_2$-core/actin; lane 1, molecular weight standards; lane 2, cross-linking reaction of $Ca_V\beta_2$-core with actin; lane 3, actin alone incubated with DSSO; and lane 4, $Ca_V\beta_2$-core alone incubated with the cross-linker. The band enclosed by a red square was excised from the gel for tryptic digestion and further analyzed by LC-MS/MS. **D**, Same as *C* but for DSBU cross-linker. **E**, Scheme showing the location and residue number of the amino acids involved in inter-molecular cross-links between $Ca_V\beta_2$-core/actin selected after DisVis analysis (top panel) and 3D representation of two adjacent actin monomers in one protofilament, named *n* and *n+2*, showing the amino acids participating in cross-links mapped on the actin structure. Residues in monomer *n+2* are labelled in bold with an apostrophe (’). The amino acids involved in distance restraints are shown as spheres, with green and red indicating, consistency and violations, respectively, with the accessible interaction space of $Ca_V\beta_2$ with respect to actin (cyan surface). The green residues form a contiguous patch on two adjacent actin subunits (green contour) laying within the accessible interaction space. For comparison, the residues within one actin subunit encompass a surface incompatible with the accessible interaction space (black dashed contour). **F**, Structural mapping of the cross-links (red lines) that satisfied data consistency upon DisVis filtering considering one $Ca_V\beta_2$ molecule and two adjacent actin monomers. Actin is shown in space-filling and ribbon diagram, while for clarity only the ribbon of $Ca_V\beta_2$ is displayed.

Figure 2. **Model of $Ca_V\beta_2$ bound to actin shows an extended contact surface and electrostatic complementarity**. **A**, Space-filling and ribbon diagram showing two views related by a 90° rotation of the best-scoring docking model of $Ca_V\beta_2$ complexed with actin. One molecule of $Ca_V\beta_2$, represented in blue, interacts with two adjacent monomers in one actin protofilament, named *n* (light yellow) and *n+2* (light pink). Actin subunits are labeled following their position along the filament from the pointed end (-) to the barbed end (+). For clarity, in the right panel the space-filling for $Ca_V\beta_2$ was removed. The four actin subdomains, SD1-SD4, are labelled in the *n* monomer of actin. **B**, Surface models of $Ca_V\beta_2$ and actin showing the

contact frequency of $Ca_V\beta_2$ and actin residues. **C**, same as *B* but showing the electrostatic potential map of both proteins.

Figure 3. Binding of $Ca_V\beta_2$ to actin depends on the ionic strength. A, SDS-PAGE of a representative F-actin co-sedimentation assay at the indicated NaCl concentrations. Briefly, $Ca_V\beta_2$-core was incubated with actin in actin polymerization buffer, centrifuged and the supernatant (S) and pellet (P) fractions were separated. The pellet fraction was resuspended in the same volume as the volume of the supernatant. Supernatant and pellet fractions were then resolved by denaturing SDS-PAGE. In control reactions, $Ca_V\beta_2$-core alone was centrifuged and the supernatant and pellet fractions separated and resolved by SDS-PAGE (lower panel). For clarity, irrelevant lanes were cropped from the source images (as indicated by the white space) and the full gel images are shown in Supplementary Figure S4. **B**, Plot of the fraction of $Ca_V\beta_2$-core bound to actin calculated by densitometry against the indicated NaCl concentrations. Lines represent the average value ± standard error of the mean (SEM). n.s, not significant; * $p < 0.05$; ** $p < 0.01$; Unpaired two-tailed t-test. Each experiment was repeated three times.

Figure 4. **Alanine substitution of predicted protein-protein interaction hotspots decreases the *in vitro* affinity of $Ca_V\beta_2$ for actin but not for the AID peptide**. **A**, Structure of $Ca_V\beta_2$ (blue ribbon) highlighting the eight predicted hotspot residues (red spheres) that were mutated to alanine in the background of $Ca_V\beta_2$-core. Two actin subunits interacting with $Ca_V\beta_2$ are shown in space-filling model with the subunits oriented from the barbed end (*n*+2, light pink) to the pointed end (*n*, light yellow). Note that this orientation is different from the one shown for the complex in Figure 2. **B**, Linear representation of $Ca_V\beta_2$-core domain structure indicating the two hotspot mutants, $Ca_V\beta_2$-core 6Ala bearing six hotspot mutations located within the GK domain and $Ca_V\beta_2$-core 8Ala carrying two additional mutations of hotspots within the SH3 domain. Bottom panel shows the size-exclusion chromatography profiles of the hotspot mutants, $Ca_V\beta_2$-core 6Ala (orange) and $Ca_V\beta_2$-core 8Ala (green). **C**, SDS-PAGE of representative F-actin co-sedimentation assays for $Ca_V\beta_2$-core wild-type (lanes 2-5), $Ca_V\beta_2$-core 6Ala (lanes 7-10) and $Ca_V\beta_2$-core 8Ala (lanes 11-14) and the respective control reactions with the proteins alone in the absence of actin. S, supernatant fraction; P, pellet fraction. **D**, Plot of the fraction of the indicated $Ca_V\beta_2$-core proteins bound to actin. Lines represent the average value ± standard error of the mean (SEM). n.s, not significant; ** $p < 0.01$; Unpaired two-tailed t-test. Each experiment was repeated three times and full images are shown in Supplementary Figure S7. **E**, SDS-PAGE of a representative pull down assay using either GST alone or fused to the AID site (GST-AID) as bait and as prey the different $Ca_V\beta_2$-core proteins: $Ca_V\beta_2$-core WT (WT), $Ca_V\beta_2$-core 6Ala (6Ala) and $Ca_V\beta_2$-core 8Ala (8Ala). Lane 1, molecular

weight standards; lanes 2-4, $Ca_V\beta_2$-core protein used as input for the assay; lanes 5, 7 and 9, elution fractions from the control pull down assay using GST as bait and the indicated proteins as prey; lanes 6, 8 and 10, elution fractions from the pull down assay using GST-AID as bait and the indicated proteins as prey. All $Ca_V\beta_2$-core proteins, wild-type and mutants are pulled down with GST-AID but not with GST alone. Each experiment was repeated three times and full images are shown in Supplementary Figure S6.

Figure 5. **Hotspots substitutions in $Ca_V\beta_4$ R482X mutant associated with juvenile myoclonic epilepsy blunt association with actin**. **A**, Superimposition of the backbone heavy atoms of the bound structures of $Ca_V\beta_2$ (cyan ribbon diagram) and $Ca_V\beta_4$ (purple ribbon diagram). Each $Ca_V\beta$ structure is the average of the four best scored models. For clarity, two actin subunits used as reference for the alignment are shown in space-filling model in light yellow and pink. **B**, Linear representation of $Ca_V\beta_4$ domain structure indicating the positions of predicted hotspots substituted by alanine and of the premature stop codon at position 482 encoding $Ca_V\beta_4$ R482X mutant associated with juvenile myoclonic epilepsy. Sequence numbering according to human $Ca_V\beta_4$ (UniProtKB accession number O00305-1). The two hotspot mutants bearing the indicated amino acid substitutions in either six or eight positions were introduced in $Ca_V\beta_4$ R482X background and the corresponding size-exclusion chromatography profiles of $Ca_V\beta_4$ R482X (black), $Ca_V\beta_4$ R482X 6Ala (orange) and $Ca_V\beta_4$ R482X 8Ala (green) are shown. **C**, SDS-PAGE of F-actin co-sedimentation assays for $Ca_V\beta_4$ R482X (lanes 2-5), $Ca_V\beta_4$ R482X 6Ala (lanes 6-9) and $Ca_V\beta_4$ R482X 8Ala (lanes 10-13). S, supernatant fraction; P, pellet fraction. **D**, Graph of the fraction of the indicated $Ca_V\beta_4$ R482X protein bound to actin. Lines represent the average value ± standard error of the mean (SEM). $^{**}p < 0.01$; $^{***}p < 0.001$; $^{****}p < 0.0001$ Unpaired two-tailed t-test. Each experiment was repeated three times and full images are shown in Supplementary Figure S10. **E**, SDS-PAGE of a representative pull down assay using either GST alone or fused to the AID site (GST-AID) as bait and as prey $Ca_V\beta_4$ R482X or $Ca_V\beta_4$ R482X 6Ala or $Ca_V\beta_4$ R482X. Lane 1, molecular weight standards; lanes 2-4, $Ca_V\beta_4$ R482X proteins used as input for the assay; lanes 5, 7 and 9, elution fractions from the control pull down assay using GST as bait and the indicated proteins as prey; lanes 6, 8 and 10, same as lanes 5, 7 and 9 but using GST-AID as bait. All $Ca_V\beta_4$ R482X proteins tested bind to GST-AID but not with GST alone. Each experiment was repeated three times and full images are shown in Supplementary Figure S9.

Figure 6. Actin-association deficient $Ca_V\beta_2$ mutant decreases $Ca_V1.2$-mediated ion currents channels but not gating currents. A, Representative laser scanning confocal images of HEK293 cells expressing either wild-type $Ca_V\beta_2$ ($Ca_V\beta_2$ WT) or $Ca_V\beta_2$ hotspots

mutant ($Ca_V\beta_2$ MUT) with impaired actin binding. For visualization and identification of transfected cells, both $Ca_V\beta_2$ constructs were fused to mRFP. The white arrowheads point to $Ca_V\beta_2$ localized at the plasma membrane. Scale bar: 10 µm. **B**, Western blot (WB) of representative crude lysates from HEK293 cells expressing either $Ca_V\beta_2$ WT or $Ca_V\beta_2$ MUT. Crude cell lysates were resolved by SDS-PAGE and transferred to nitrocellulose membrane for probing with anti-$Ca_V\beta$ (top panel) and anti-GAPDH for using as loading control (bottom panel). Each WB was repeated three times and full images are shown in Supplementary Figure S13. **C**, Representative ionic current traces, current *versus* voltage (I/V) and relative open probabilities versus voltage plot obtained from HEK293 cells transiently cotransfected with $Ca_V1.2$ (fused to mNeonGreen) and either $Ca_V\beta_2$ WT or $Ca_V\beta_2$ MUT (fused to mRFP). Ionic currents were elicited by voltage steps from -50 to +70 mV in 5 mV increments with a holding potential of -90 mV. For clarity, only the currents traces induced by -50, -15 and +50 mV pulses are shown. *n* size (number of cells); 32 and 29 for $Ca_V1.2/Ca_V\beta_2$ WT and $Ca_V1.2/Ca_V\beta_2$ MUT, respectively. **D**, Representative gating current traces from HEK293 cells co-expressing $Ca_V1.2$ with either $Ca_V\beta_2$ WT or $Ca_V\beta_2$ MUT and corresponding plots of the total charge movement (*Qon*). *Qon* was obtained from the integral of the *On* gating current over time (shaded area under the gating current) during the voltage step to the reversal potential for Ba^{2+}, as shown in the inset. The median *Qon* value is indicated by a line in each box of the plot and whiskers indicate 95% confidence.

Figure 7. Actin-association deficient $Ca_V\beta_2$ mutant decreases the number of functionally available $Ca_V1.2$ channels A, Representative current traces and plot of the relationship between variance and mean macroscopic current $\left(\frac{\sigma^2}{\langle I\rangle(V_m - V_{rev})}\right)$ versus $\left(\frac{\langle I\rangle}{V_m - V_{rev}}\right)$ obtained at different voltages for two representative cells expressing $Ca_V1.2$ complexed with either $Ca_V\beta_2$ WT or $Ca_V\beta_2$ MUT according to Eq. 6. The red lines delineating the current traces correspond to the time window used for noise analysis. The number of functionally available channels *n* and the unitary conductance γ were calculated from the slope and the *y*-intercept of the linear fit, respectively. **B**, Top panel shows the box plots of *n*, γ and Po_{max}, for all analysed cells (original sample size, n = 10) and bottom panel, the respective bootstrap distributions (Bootstrap sample N= 500,000). n.s. non-significant, **p* < 0.05; Unpaired two-tailed t-test.

Figure 8. Model for the role of $Ca_V\beta$-actin in endocytic quality control of $Ca_V1.2$ at the cell surface. A competent $Ca_V\beta$-actin interaction permits the clearance of defective $Ca_V1.2$ channels from the plasma membrane. Disruption of this interaction leads to the accumulation of non-functional channels and a reduction in ionic current.

References

1 Catterall, W. A. Voltage-gated calcium channels. *Cold Spring Harb.Perspect.Biol.* **3**, a003947 (2011).

2 Vergnol, A., Traoré, M., Pietri-Rouxel, F. & Falcone, S. New Insights in CaVβ Subunits: Role in the Regulation of Gene Expression and Cellular Homeostasis. *Frontiers in cell and developmental biology* **10**, 880441, doi:10.3389/fcell.2022.880441 (2022).

3 Zamponi, G. W., Striessnig, J., Koschak, A. & Dolphin, A. C. The Physiology, Pathology, and Pharmacology of Voltage-Gated Calcium Channels and Their Future Therapeutic Potential. *Pharmacol Rev* **67**, 821-870, doi:10.1124/pr.114.009654 (2015).

4 Bidaud, I. & Lory, P. Hallmarks of the channelopathies associated with L-type calcium channels: a focus on the Timothy mutations in Ca(v)1.2 channels. *Biochimie* **93**, 2080-2086, doi:10.1016/j.biochi.2011.05.015 (2011).

5 Wemhoner, K. *et al.* Gain-of-function mutations in the calcium channel CACNA1C (Cav1.2) cause non-syndromic long-QT but not Timothy syndrome. *Journal of molecular and cellular cardiology* **80**, 186-195, doi:10.1016/j.yjmcc.2015.01.002 (2015).

6 Lanzetti, S. & Di Biase, V. Small Molecules as Modulators of Voltage-Gated Calcium Channels in Neurological Disorders: State of the Art and Perspectives. *Molecules* **27** (2022).

7 Escayg, A. *et al.* Coding and noncoding variation of the human calcium-channel beta4- subunit gene CACNB4 in patients with idiopathic generalized epilepsy and episodic ataxia. *Am.J.Hum.Genet.* **66**, 1531-1539 (2000).

8 Coste de Bagneaux, P. *et al.* A homozygous missense variant in CACNB4 encoding the auxiliary calcium channel beta4 subunit causes a severe neurodevelopmental disorder and impairs channel and non-channel functions. *PLoS Genet* **16**, e1008625 (2020).

9 Andrade, A. *et al.* Genetic Associations between Voltage-Gated Calcium Channels and Psychiatric Disorders. *International journal of molecular sciences* **20**, doi:10.3390/ijms20143537 (2019).

10 Lorenzon, N. M. & Beam, K. G. Disease causing mutations of calcium channels. *Channels (Austin, Tex.)* **2**, 163-179, doi:10.4161/chan.2.3.5950 (2008).

11 Lorenzon, N. M. & Beam, K. G. Calcium channelopathies. *Kidney Int* **57**, 794-802, doi:10.1046/j.1523-1755.2000.00917.x (2000).

12 Hidalgo, P. & Neely, A. Multiplicity of protein interactions and functions of the voltage-gated calcium channel β-subunit. *Cell calcium* **42**, 389-396 (2007).

13 Rima, M. *et al.* Protein partners of the calcium channel β-subunit highlight new cellular functions. *The Biochemical journal* **473**, 1831-1844, doi:10.1042/bcj20160125 (2016).

14 Neely, A. & Hidalgo, P. Structure-function of proteins interacting with the α_1 pore-forming subunit of high-voltage-activated calcium channels. *Frontiers in physiology* **5**, 209, doi:10.3389/fphys.2014.00209 (2014).

15 Buraei, Z. & Yang, J. Structure and function of the beta subunit of voltage-gated Ca(2)(+) channels. *Biochimica et biophysica acta* **1828**, 1530-1540, doi:10.1016/j.bbamem.2012.08.028 (2013).

16 Hofmann, F., Belkacemi, A. & Flockerzi, V. Emerging alternative functions for the auxiliary subunits of the voltage-gated calcium channels. *Current molecular pharmacology* **8**, 162-168 (2015).

17 Cruz-Garcia, Y. *et al.* Nanoenviroments of the β-Subunit of L-Type Voltage-Gated Calcium Channels in Adult Cardiomyocytes. *Frontiers in cell and developmental biology* **9**, 724778, doi:10.3389/fcell.2021.724778 (2021).

18 Pickel, S. *et al.* The β(2)-Subunit of Voltage-Gated Calcium Channels Regulates Cardiomyocyte Hypertrophy. *Frontiers in cardiovascular medicine* **8**, 704657, doi:10.3389/fcvm.2021.704657 (2021).

19 Belkacemi, A. *et al.* IP(3) Receptor-Dependent Cytoplasmic Ca(2+) Signals Are Tightly Controlled by Cavβ3. *Cell reports* **22**, 1339-1349, doi:10.1016/j.celrep.2018.01.010 (2018).

20 Erdogmus, S. *et al.* Cavβ1 regulates T cell expansion and apoptosis independently of voltage-gated Ca(2+) channel function. *Nature communications* **13**, 2033 (2022).

21 Buraei, Z. & Yang, J. The β-subunit of voltage-gated Ca^{2+} channels. *Physiol Rev.* **90**, 1461-1506 (2010).

22 Skinnider, M. A. *et al.* An atlas of protein-protein interactions across mouse tissues. *Cell* **184**, 4073-4089.e4017, doi:10.1016/j.cell.2021.06.003 (2021).

23 Muller, C. S. *et al.* Quantitative proteomics of the Ca_V2 channel nano-environments in the mammalian brain. *Proceedings of the National Academy of Sciences of the United States of America* **107**, 14950-14957, doi:10.1073/pnas.1005940107 (2010).

24 Takahashi, S. X., Miriyala, J., Tay, L. H., Yue, D. T. & Colecraft, H. M. A $Ca_V\beta$ SH3/guanylate kinase domain interaction regulates multiple properties of voltage-gated Ca^{2+} channels. *J.Gen.Physiol* **126**, 365-377 (2005).

25 Gonzalez-Gutierrez, G. *et al.* The guanylate kinase domain of the β-subunit of voltage-gated calcium channels suffices to modulate gating. *Proceedings of the National Academy of Sciences of the United States of America* **105**, 14198-14203, doi:10.1073/pnas.0806558105 (2008).

26 Opatowsky, Y., Chomsky-Hecht, O., Kang, M. G., Campbell, K. P. & Hirsch, J. A. The voltage-dependent calcium channel beta subunit contains two stable interacting domains. *J.Biol.Chem.* **278**, 52323-52332 (2003).

27 Pragnell, M. *et al.* Calcium channel β-subunit binds to a conserved motif in the I-II cytoplasmic linker of the α_1-subunit. *Nature* **368**, 67-70 (1994).

28 Van Petegem, F., Clark, K. A., Chatelain, F. C. & Minor, D. L., Jr. Structure of a complex between a voltage-gated calcium channel β-subunit and an α-subunit domain. *Nature* **429**, 671-675 (2004).

29 Opatowsky, Y., Chen, C. C., Campbell, K. P. & Hirsch, J. A. Structural analysis of the voltage-dependent calcium channel β-subunit functional core and its complex with the α_1-interaction domain. *Neuron* **42**, 387-399 (2004).

30 Chen, Y. H. *et al.* Structural basis of the α_1-β subunit interaction of voltage-gated Ca^{2+} channels. *Nature* **429**, 675-680 (2004).

31 Stölting, G. *et al.* Direct interaction of $Ca_V\beta$ with actin up-regulates L-type calcium currents in HL-1 cardiomyocytes. *The Journal of biological chemistry* **290**, 4561-4572, doi:10.1074/jbc.M114.573956 (2015).

32 Guzman, G. A., Guzman, R. E., Jordan, N. & Hidalgo, P. A Tripartite Interaction Among the Calcium Channel α1- and β-Subunits and F-Actin Increases the Readily Releasable Pool of Vesicles and Its Recovery After Depletion. *Frontiers in cellular neuroscience* **13**, 125, doi:10.3389/fncel.2019.00125 (2019).

33 Conrad, R., Kortzak, D., Guzman, G. A., Miranda-Laferte, E. & Hidalgo, P. Ca(V) β controls the endocytic turnover of Ca(V) 1.2 L-type calcium channel. *Traffic (Copenhagen, Denmark)* **22**, 180-193, doi:10.1111/tra.12788 (2021).

34 Hidalgo, P., Gonzalez-Gutierrez, G., Garcia-Olivares, J. & Neely, A. The α_1-β-subunit interaction that modulates calcium channel activity is reversible and requires a competent α-interaction domain. *J.Biol.Chem.* **281**, 24104-24110 (2006).

35 Rappsilber, J., Mann, M. & Ishihama, Y. Protocol for micro-purification, enrichment, pre-fractionation and storage of peptides for proteomics using StageTips. *Nature protocols* **2**, 1896-1906, doi:10.1038/nprot.2007.261 (2007).

36 Chambers, M. C. *et al.* A cross-platform toolkit for mass spectrometry and proteomics. *Nature biotechnology* **30**, 918-920, doi:10.1038/nbt.2377 (2012).

37 Yılmaz, Ş., Busch, F., Nagaraj, N. & Cox, J. Accurate and Automated High-Coverage Identification of Chemically Cross-Linked Peptides with MaxLynx. *Analytical chemistry* **94**, 1608-1617, doi:10.1021/acs.analchem.1c03688 (2022).

38 Iacobucci, C. *et al.* A cross-linking/mass spectrometry workflow based on MS-cleavable cross-linkers and the MeroX software for studying protein structures and protein-protein interactions. *Nature protocols* **13**, 2864-2889, doi:10.1038/s41596-018-0068-8 (2018).

39 Lu, L. *et al.* Identification of MS-Cleavable and Noncleavable Chemically Cross-Linked Peptides with MetaMorpheus. *Journal of proteome research* **17**, 2370-2376, doi:10.1021/acs.jproteome.8b00141 (2018).

40 van Zundert, G. C. & Bonvin, A. M. DisVis: quantifying and visualizing accessible interaction space of distance-restrained biomolecular complexes. *Bioinformatics* **31**, 3222-3224 (2015).

41 van Zundert, G. C. *et al.* The DisVis and PowerFit Web Servers: Explorative and Integrative Modeling of Biomolecular Complexes. *J Mol Biol* **429**, 399-407, doi:10.1016/j.jmb.2016.11.032 (2017).

42 Findeisen, F. *et al.* Stapled voltage-gated calcium channel (Ca_V) α-Interaction Domain (AID) peptides act as selective protein-protein interaction inhibitors of Ca_V Function. *ACS chemical neuroscience* **8**, 1313-1326, doi:10.1021/acschemneuro.6b00454 (2017).

43 Merino, F. *et al.* Structural transitions of F-actin upon ATP hydrolysis at near-atomic resolution revealed by cryo-EM. *Nature structural & molecular biology* **25**, 528-537, doi:10.1038/s41594-018-0074-0 (2018).

44 van Zundert, G. C. P. *et al.* The HADDOCK2.2 Web Server: User-Friendly Integrative Modeling of Biomolecular Complexes. *J Mol Biol* **428**, 720-725, doi:10.1016/j.jmb.2015.09.014 (2016).

45 Dominguez, C., Boelens, R. & Bonvin, A. M. HADDOCK: a protein-protein docking approach based on biochemical or biophysical information. *Journal of the American Chemical Society* **125**, 1731-1737, doi:10.1021/ja026939x (2003).

46 Orban-Nemeth, Z. *et al.* Structural prediction of protein models using distance restraints derived from cross-linking mass spectrometry data. *Nature protocols* **13**, 478-494, doi:10.1038/nprot.2017.146 (2018).

47 Bonvin, A., Karaca, E., Kastritis, P. L. & Rodrigues, J. Defining distance restraints in HADDOCK. *Nature protocols* **13**, 1503, doi:10.1038/s41596-018-0017-6 (2018).

48 Orbán-Németh, Z. *et al.* Reply to 'Defining distance restraints in HADDOCK'. *Nature protocols* **13**, 1503-1505, doi:10.1038/s41596-018-0018-5 (2018).

49 Hubbard, S. & Thornton, J. *NACCESS, Computer Program* (Department of Biochemistry Molecular Biology, University College London, 1993).

50 de Vries, S. J. & Bonvin, A. M. CPORT: a consensus interface predictor and its performance in prediction-driven docking with HADDOCK. *PloS one* **6**, e17695 (2011).

51 Paudyal, S. *et al.* Combined computational and experimental analysis of a complex of ribonuclease III and the regulatory macrodomain protein, YmdB. *Proteins* **83**, 459-472, doi:10.1002/prot.24751 (2015).

52 Jurrus, E. *et al.* Improvements to the APBS biomolecular solvation software suite. *Protein science : a publication of the Protein Society* **27**, 112-128 (2018).

53 Meireles, L. M., Dömling, A. S. & Camacho, C. J. ANCHOR: a web server and database for analysis of protein-protein interaction binding pockets for drug discovery. *Nucleic Acids Res* **38**, W407-411 (2010).

54 Kortemme, T., Kim, D. E. & Baker, D. Computational alanine scanning of protein-protein interfaces. *Sci STKE* **2004**, pl2, doi:10.1126/stke.2192004pl2 (2004).

55 Wood, C. W. *et al.* BAlaS: fast, interactive and accessible computational alanine-scanning using BudeAlaScan. *Bioinformatics* **36**, 2917-2919, doi:10.1093/bioinformatics/btaa026 (2020).

56 Ibarra, A. A. *et al.* Predicting and Experimentally Validating Hot-Spot Residues at Protein-Protein Interfaces. *ACS chemical biology* **14**, 2252-2263 (2019).

57 Dehouck, Y., Kwasigroch, J. M., Rooman, M. & Gilis, D. BeAtMuSiC: Prediction of changes in protein-protein binding affinity on mutations. *Nucleic Acids Res* **41**, W333-339, doi:10.1093/nar/gkt450 (2013).

58 Zhang, N. *et al.* MutaBind2: Predicting the Impacts of Single and Multiple Mutations on Protein-Protein Interactions. *iScience* **23**, 100939, doi:10.1016/j.isci.2020.100939 (2020).

59 Pahari, S. *et al.* SAAMBE-3D: Predicting Effect of Mutations on Protein-Protein Interactions. *International journal of molecular sciences* **21**, doi:10.3390/ijms21072563 (2020).

60 Schindelin, J. *et al.* Fiji: an open-source platform for biological-image analysis. *Nature methods* **9**, 676-682, doi:10.1038/nmeth.2019 (2012).

61 Miranda-Laferte, E. *et al.* The N-terminal domain tethers the voltage-gated calcium channel β_{2e}-subunit to the plasma membrane via electrostatic and hydrophobic interactions. *The Journal of biological chemistry*, doi:10.1074/jbc.M113.507244 (2014).

62 Gonzalez-Gutierrez, G., Miranda-Laferte, E., Neely, A. & Hidalgo, P. The Src homology 3 domain of the β-subunit of voltage-gated calcium channels promotes endocytosis via dynamin interaction. *The Journal of biological chemistry* **282**, 2156-2162 (2007).

63 Sesti, F. & Goldstein, S. A. Single-channel characteristics of wild-type IKs channels and channels formed with two minK mutants that cause long QT syndrome. *The Journal of general physiology* **112**, 651-663 (1998).

64 Reuter, H., Stevens, C. F., Tsien, R. W. & Yellen, G. Properties of single calcium channels in cardiac cell culture. *Nature* **297**, 502-503 (1982).

65 Handrock, R. *et al.* Single-channel properties of L-type calcium channels from failing human ventricle. *Cardiovascular research* **37**, 445-455, doi:10.1016/s0008-6363(97)00257-5 (1998).

66 Fox, A. P., Nowycky, M. C. & Tsien, R. W. Single-channel recordings of three types of calcium channels in chick sensory neurones. *J.Physiol.(Lond.)* **394**, 173-200 (1987).

67 Efron, B. & J.Tibshirani, R. *An Introduction to the Bootstrap. Monographs on Statistics and Applied Probability. Chapman & Hall/CRC, Boca Raton, Florida, USA.*, (1993).

68 Mintseris, J. & Gygi, S. P. High-density chemical cross-linking for modeling protein interactions. *Proceedings of the National Academy of Sciences of the United States of America* **117**, 93-102, doi:10.1073/pnas.1902931116 (2020).

69 Wang, X. *et al.* Molecular Details Underlying Dynamic Structures and Regulation of the Human 26S Proteasome. *Molecular & cellular proteomics : MCP* **16**, 840-854, doi:10.1074/mcp.M116.065326 (2017).

70 Bullock, J. M. A., Sen, N., Thalassinos, K. & Topf, M. Modeling Protein Complexes Using Restraints from Crosslinking Mass Spectrometry. *Structure (London, England : 1993)* **26**, 1015-1024.e1012, doi:10.1016/j.str.2018.04.016 (2018).

71 Rappsilber, J. The beginning of a beautiful friendship: cross-linking/mass spectrometry and modelling of proteins and multi-protein complexes. *Journal of structural biology* **173**, 530-540, doi:10.1016/j.jsb.2010.10.014 (2011).

72 Heier, J. A., Dickinson, D. J. & Kwiatkowski, A. V. Measuring Protein Binding to F-actin by Co-sedimentation. *Journal of visualized experiments : JoVE* (2017).

73 Kumari, A., Kesarwani, S., Javoor, M. G., Vinothkumar, K. R. & Sirajuddin, M. Structural insights into actin filament recognition by commonly used cellular actin markers. *The EMBO journal* **39**, e104006, doi:10.15252/embj.2019104006 (2020).

74 F., V. P., Duderstadt, K. E., Clark, K. A., Wang, M. & Minor, D. L., Jr. Alanine-scanning mutagenesis defines a conserved energetic hotspot in the CaValpha1 AID-CaVbeta interaction site that is critical for channel modulation. *Structure.* **16**, 280-294 (2008).

75 Lensink, M. F., Méndez, R. & Wodak, S. J. Docking and scoring protein complexes: CAPRI 3rd Edition. *Proteins* **69**, 704-718, doi:10.1002/prot.21804 (2007).

76 Ohmori, I. *et al.* A CACNB4 mutation shows that altered Ca(v)2.1 function may be a genetic modifier of severe myoclonic epilepsy in infancy. *Neurobiology of disease* **32**, 349-354, doi:10.1016/j.nbd.2008.07.017 (2008).

77 Qin, N. *et al.* Unique regulatory properties of the type 2a Ca2+ channel beta subunit caused by palmitoylation. *Proc.Natl.Acad.Sci.USA* **95**, 4690-4695 (1998).

78 Chien, A. J., Carr, K. M., Shirokov, R. E., Rios, E. & Hosey, M. M. Identification of palmitoylation sites within the L-type calcium channel beta2a subunit and effects on channel function. *J.Biol.Chem.* **271**, 26465-26468 (1996).

79 Miranda-Laferte, E., Schmidt, S., Jara, A. C., Neely, A. & Hidalgo, P. A short polybasic segment between the two conserved domains of the beta2a-subunit modulates the rate of inactivation of R-type calcium channel. *The Journal of biological chemistry* **287**, 32588-32597, doi:10.1074/jbc.M112.362509 (2012).

80 Miranda-Laferte, E. *et al.* Homodimerization of the Src homology 3 domain of the calcium channel β-subunit drives dynamin-dependent endocytosis. *J.Biol.Chem.* **286**, 22203-22210 (2011).

81 Noceti, F. *et al.* Effective gating charges per channel in voltage-dependent K+ and Ca2+ channels. *J.Gen.Physiol* **108**, 143-155 (1996).

82 Neely, A., Wei, X., Olcese, R., Birnbaumer, L. & Stefani, E. Potentiation by the β subunit of the ratio of the ionic current to the charge movement in the cardiac calcium channel. *Science (New York, N.Y.)* **262**, 575-578 (1993).

83 Bezanilla, F. & Stefani, E. Gating currents. *Methods Enzymol.* **293**, 331-352 (1998).

84 Alvarez, O., Gonzalez, C. & Latorre, R. Counting channels: a tutorial guide on ion channel fluctuation analysis. *Adv.Physiol Educ.* **26**, 327-341 (2002).

85 Tsien, R. W., Bean, B. P., Lansman, J. B., Nilius, B. & Nowycky, M. C. Mechanisms of calcium channel modulation by β-afrenergic agents and dihydropyridine Ca agonist. *J.Mol.Cell.Cardiol.* **18**, 691-710 (1986).

86 Kostan, J. *et al.* Molecular basis of F-actin regulation and sarcomere assembly via myotilin. *PLoS biology* **19**, e3001148, doi:10.1371/journal.pbio.3001148 (2021).

87 Hess, P., Lansman, J. B. & Tsien, R. W. Different modes of Ca channel gating behaviour favored by dihydropyridine Ca agonist and antagonists. *Nature* **311**, 538-544 (1984).

88 Guia, A., Stern, M. D., Lakatta, E. G. & Josephson, I. R. Ion concentration-dependence of rat cardiac unitary L-type calcium channel conductance. *Biophysical journal* **80**, 2742-2750 (2001).

89 Yue, D. T., Herzig, S. & Marban, E. Beta-adrenergic stimulation of calcium channels occurs by potentiation of high-activity gating modes. *Proc.Natl.Acad.Sci.USA* **87**, 753-757 (1990).

90 Xu, X., Marx, S. O. & Colecraft, H. M. Molecular mechanisms, and selective pharmacological rescue, of Rem-inhibited CaV1.2 channels in heart. *Circulation research* **107**, 620-630 (2010).

91 Costantin, J. *et al.* Facilitation by the beta2a subunit of pore openings in cardiac Ca2+ channels. *J.Physiol.(Lond.)* **507**, 93-103 (1998).

92 Neely, A. *et al.* Dual activation of the cardiac Ca^{2+} channel α_{1C} subunit and the modulation by the β subunit. *Am.J.Physiol.* **268**, C732-C740 (1995).

93 Dzhura, I. & Neely, A. Differential modulation of cardiac Ca2+ channel gating by beta-subunits. *Biophys.J.* **85**, 274-289 (2003).

94 Sardana, R. & Emr, S. D. Membrane Protein Quality Control Mechanisms in the Endo-Lysosome System. *Trends in cell biology* **31**, 269-283, doi:10.1016/j.tcb.2020.11.011 (2021).

95 Apaja, P. M. & Lukacs, G. L. Protein homeostasis at the plasma membrane. *Physiology (Bethesda, Md.)* **29**, 265-277 (2014).

96 Babst, M. Quality control: quality control at the plasma membrane: one mechanism does not fit all. *The Journal of cell biology* **205**, 11-20, doi:10.1083/jcb.201310113 (2014).

97 Conrad, R. *et al.* Rapid Turnover of the Cardiac L-Type $Ca_V1.2$ Channel by Endocytic Recycling Regulates Its Cell Surface Availability. *iScience* **7**, 1-15, doi:10.1016/j.isci.2018.08.012 (2018).

98 Cumberworth, A., Lamour, G., Babu, M. M. & Gsponer, J. Promiscuity as a functional trait: intrinsically disordered regions as central players of interactomes. *The Biochemical journal* **454**, 361-369, doi:10.1042/bj20130545 (2013).

99 Pancsa, R. & Fuxreiter, M. Interactions via intrinsically disordered regions: what kind of motifs? *IUBMB life* **64**, 513-520, doi:10.1002/iub.1034 (2012).

100 Lu, H. *et al.* Recent advances in the development of protein-protein interactions modulators: mechanisms and clinical trials. *Signal transduction and targeted therapy* **5**, 213, doi:10.1038/s41392-020-00315-3 (2020).

101 Murakami, Y., Tripathi, L. P., Prathipati, P. & Mizuguchi, K. Network analysis and in silico prediction of protein-protein interactions with applications in drug discovery. *Current opinion in structural biology* **44**, 134-142, doi:10.1016/j.sbi.2017.02.005 (2017).

102 Jubb, H. C. *et al.* Mutations at protein-protein interfaces: Small changes over big surfaces have large impacts on human health. *Progress in biophysics and molecular biology* **128**, 3-13, doi:10.1016/j.pbiomolbio.2016.10.002 (2017).

103 Wang, X., Ni, D., Liu, Y. & Lu, S. Rational Design of Peptide-Based Inhibitors Disrupting Protein-Protein Interactions. *Frontiers in chemistry* **9**, 682675, doi:10.3389/fchem.2021.682675 (2021).

104 Petta, I., Lievens, S., Libert, C., Tavernier, J. & De Bosscher, K. Modulation of Protein-Protein Interactions for the Development of Novel Therapeutics. *Molecular therapy : the journal of the American Society of Gene Therapy* **24**, 707-718, doi:10.1038/mt.2015.214 (2016).

105 Rusconi, F. *et al.* Peptidomimetic Targeting of $Ca_V\beta 2$ Overcomes Dysregulation of the L-Type Calcium Channel Density and Recovers Cardiac Function. *Circulation* **134**, 534-546, doi:10.1161/circulationaha.116.021347 (2016).

106 Perez-Riverol, Y. *et al.* The PRIDE database resources in 2022: a hub for mass spectrometry-based proteomics evidences. *Nucleic Acids Res* **50**, D543-D552 (2022).

Figure 1

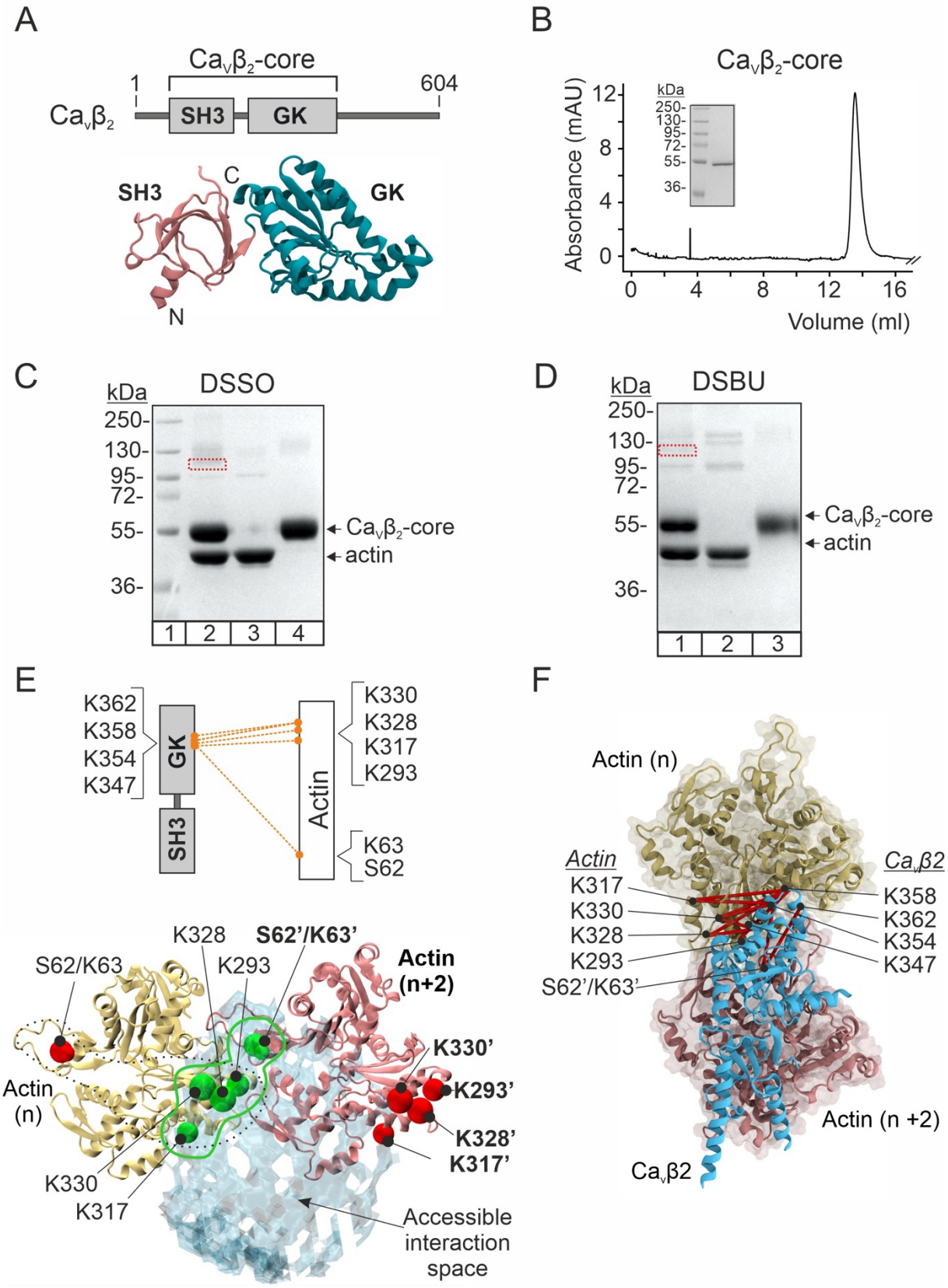
A
Ca$_V$β$_2$-core
1
604
Ca$_V$β$_2$
SH3
GK
C
SH3
GK
N
B
Ca$_V$β$_2$-core
kDa
250-
130-
95-
72-
55-
36-
Absorbance (mAU)
12
8
4
0
0
4
8
12
16
Volume (ml)
C
DSSO
kDa
250-
130-
95-
72-
55-
36-
Ca$_V$β$_2$-core
actin
1
2
3
4
D
DSBU
kDa
250-
130-
95-
72-
55-
36-
Ca$_V$β$_2$-core
actin
1
2
3
E
K362
K358
K354
K347
GK
SH3
Actin
K330
K328
K317
K293
K63
S62
K328
S62'/K63'
S62/K63
K293
Actin
(n+2)
K330'
K293'
K328'
K317'
Actin
(n)
K330
K317
Accessible
interaction
space
F
Actin (n)
Actin
K317
K330
K328
K293
S62'/K63'
Ca$_V$β2
K358
K362
K354
K347
Actin (n +2)
Ca$_V$β2

Figure 2

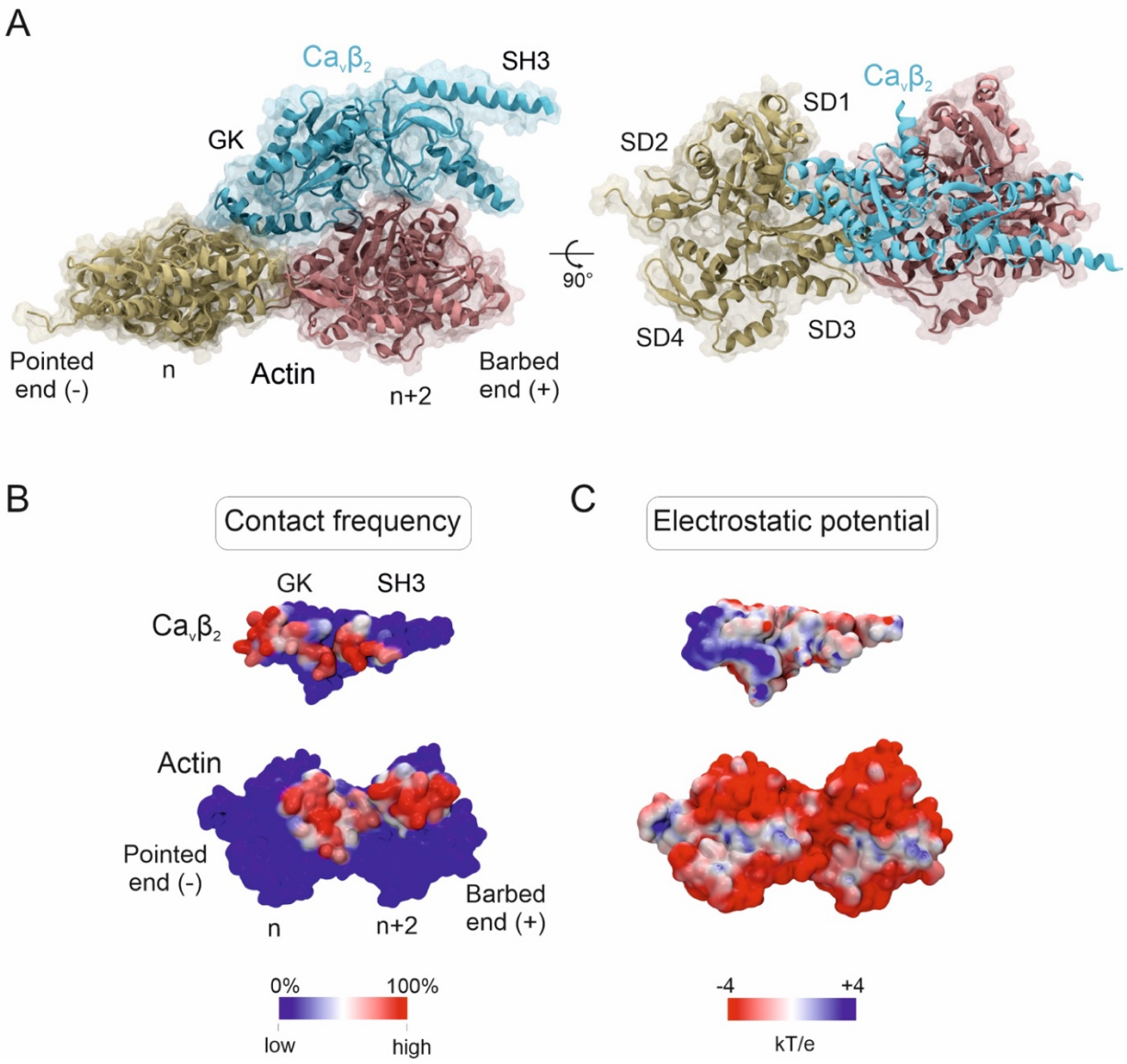
A
$Ca_v\beta_2$
SH3
GK
Pointed end (-)
n
Actin
n+2
Barbed end (+)
90°
$Ca_v\beta_2$
SD1
SD2
SD3
SD4
B
Contact frequency
GK
SH3
$Ca_v\beta_2$
Actin
Pointed end (-)
n
n+2
Barbed end (+)
0%
100%
low
high
C
Electrostatic potential
-4
+4
kT/e

Figure 3

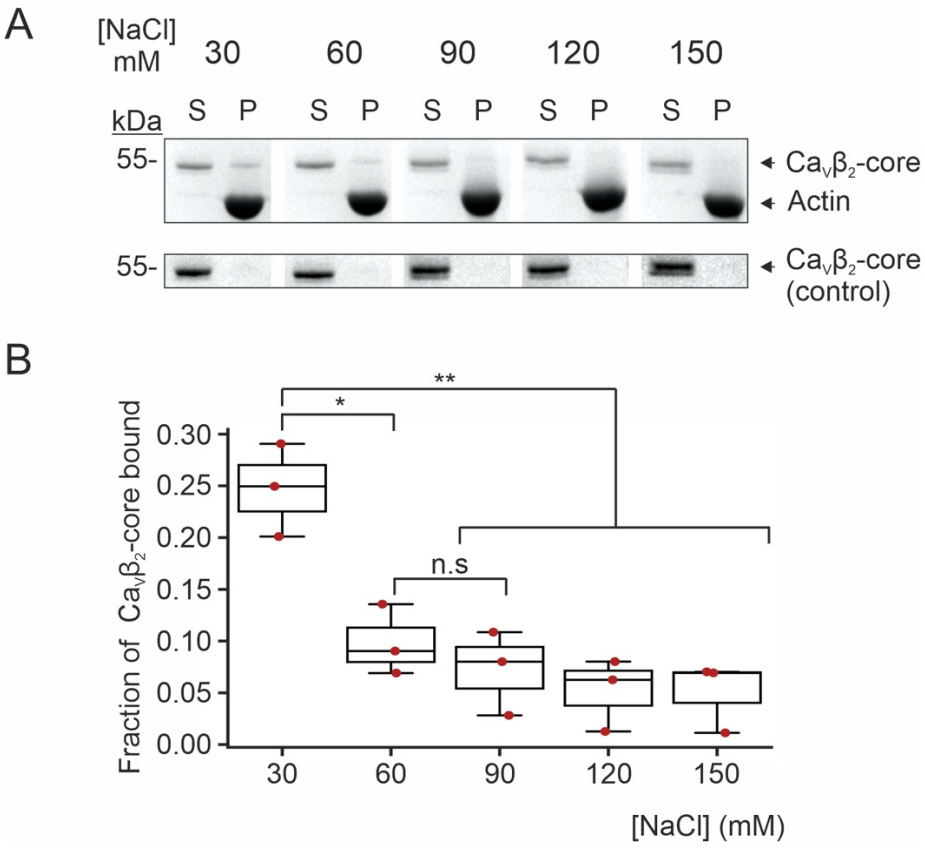
A
[NaCl] mM
30
60
90
120
150
kDa
S P S P S P S P S P
55-
$Ca_V\beta_2$-core
Actin
55-
$Ca_V\beta_2$-core (control)
B
**
*
n.s
Fraction of $Ca_V\beta_2$-core bound
0.30
0.25
0.20
0.15
0.10
0.05
0.00
30
60
90
120
150
[NaCl] (mM)

Figure 4

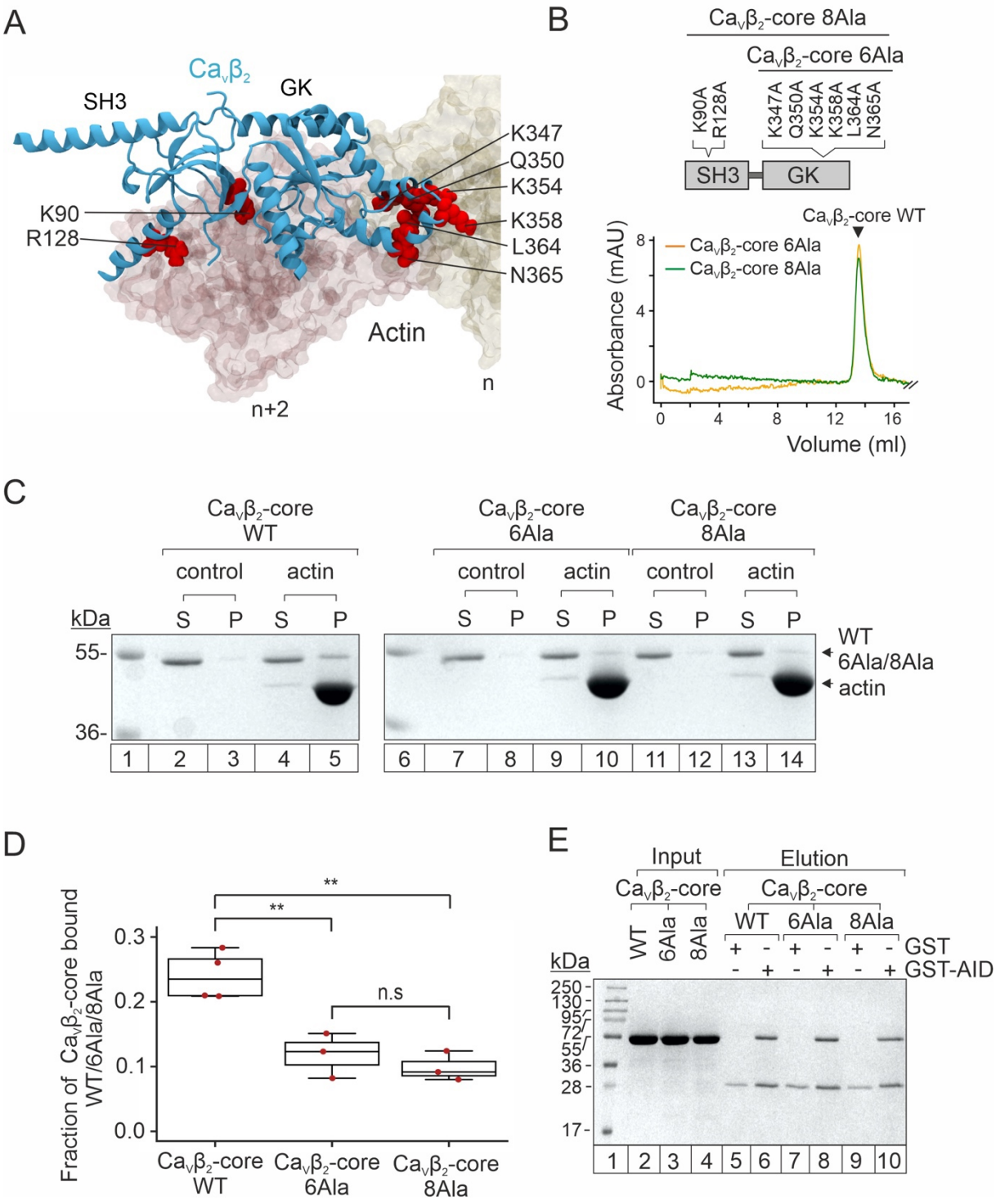
A
CaVβ2
SH3
GK
K90
R128
K347
Q350
K354
K358
L364
N365
Actin
n
n+2
B
CaVβ2-core 8Ala
CaVβ2-core 6Ala
K90A
R128A
K347A
Q350A
K354A
K358A
L364A
N365A
SH3
GK
CaVβ2-core WT
CaVβ2-core 6Ala
CaVβ2-core 8Ala
Absorbance (mAU)
Volume (ml)
C
CaVβ2-core WT
CaVβ2-core 6Ala
CaVβ2-core 8Ala
control
actin
kDa
S
P
55-
36-
WT
6Ala/8Ala
actin
1 2 3 4 5 6 7 8 9 10 11 12 13 14
D
Fraction of CaVβ2-core bound WT/6Ala/8Ala
**
**
n.s
CaVβ2-core WT
CaVβ2-core 6Ala
CaVβ2-core 8Ala
E
Input
Elution
CaVβ2-core
WT
6Ala
8Ala
GST
GST-AID
kDa
250
130
95
72
55
36
28
17
1 2 3 4 5 6 7 8 9 10

Figure 5

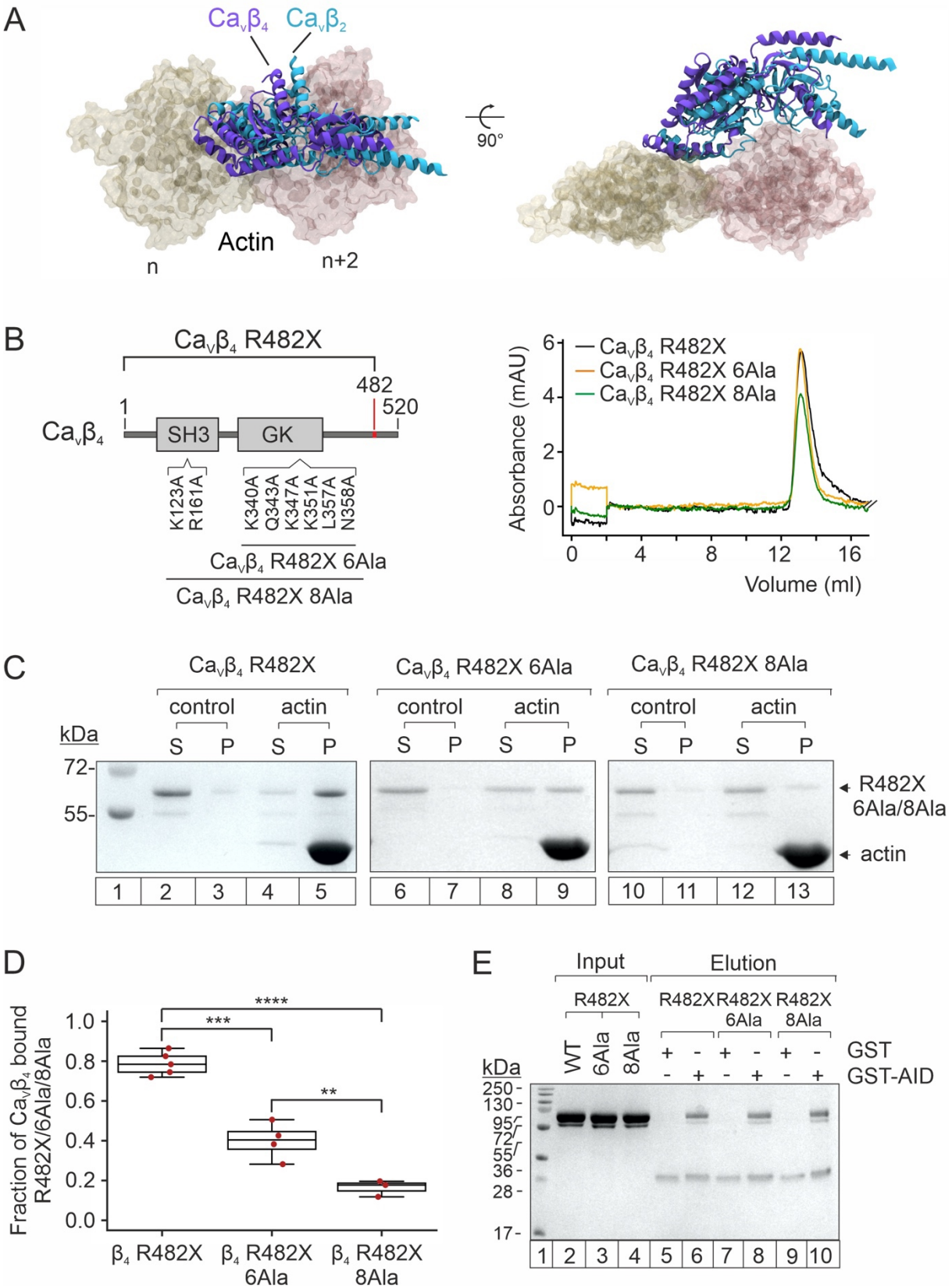
A
CaVβ4
CaVβ2
Actin
n
n+2
90°
B
CaVβ4 R482X
1
482
520
CaVβ4
SH3
GK
K123A
R161A
K340A
Q343A
K347A
K351A
L357A
N358A
CaVβ4 R482X 6Ala
CaVβ4 R482X 8Ala
CaVβ4 R482X
CaVβ4 R482X 6Ala
CaVβ4 R482X 8Ala
Absorbance (mAU)
Volume (ml)
C
CaVβ4 R482X
CaVβ4 R482X 6Ala
CaVβ4 R482X 8Ala
control
actin
S
P
kDa
72-
55-
R482X 6Ala/8Ala
actin
1 2 3 4 5 6 7 8 9 10 11 12 13
D
Fraction of CaVβ4 bound R482X/6Ala/8Ala
****
***
**
β4 R482X
β4 R482X 6Ala
β4 R482X 8Ala
E
Input
Elution
R482X
R482X 6Ala
R482X 8Ala
WT
6Ala
8Ala
GST
GST-AID
kDa
250-
130-
95-
72-
55-
36-
28-
17-
1 2 3 4 5 6 7 8 9 10

Figure 6

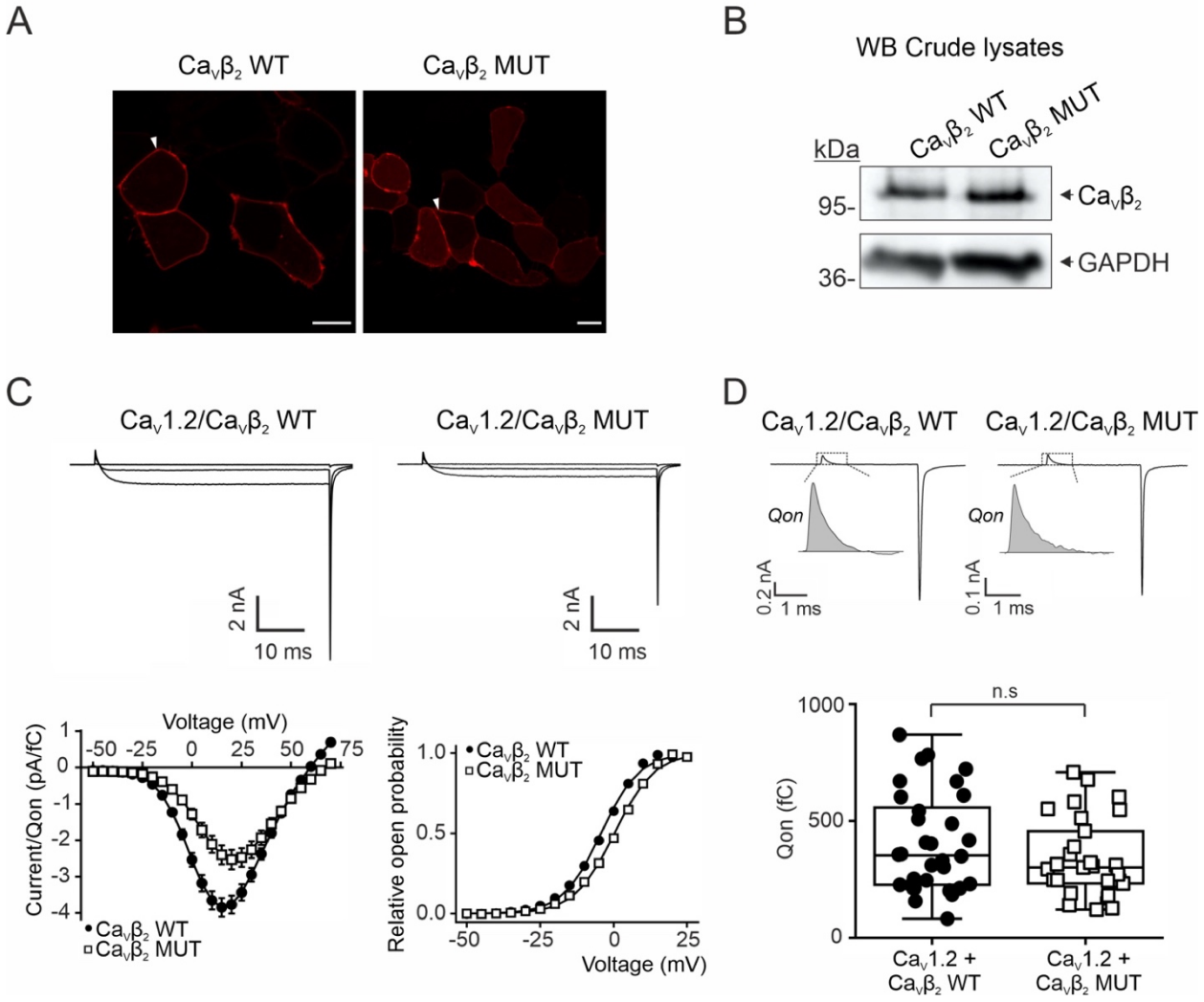
A
$Ca_V\beta_2$ WT
$Ca_V\beta_2$ MUT
B
WB Crude lysates
kDa
$Ca_V\beta_2$ WT
$Ca_V\beta_2$ MUT
95-
$Ca_V\beta_2$
36-
GAPDH
C
$Ca_V1.2/Ca_V\beta_2$ WT
$Ca_V1.2/Ca_V\beta_2$ MUT
2 nA
10 ms
Voltage (mV)
Current/Qon (pA/fC)
$Ca_V\beta_2$ WT
$Ca_V\beta_2$ MUT
Relative open probability
Voltage (mV)
D
$Ca_V1.2/Ca_V\beta_2$ WT
$Ca_V1.2/Ca_V\beta_2$ MUT
Qon
0.2 nA
0.1 nA
1 ms
n.s
Qon (fC)
$Ca_V1.2$ + $Ca_V\beta_2$ WT
$Ca_V1.2$ + $Ca_V\beta_2$ MUT

Figure 7

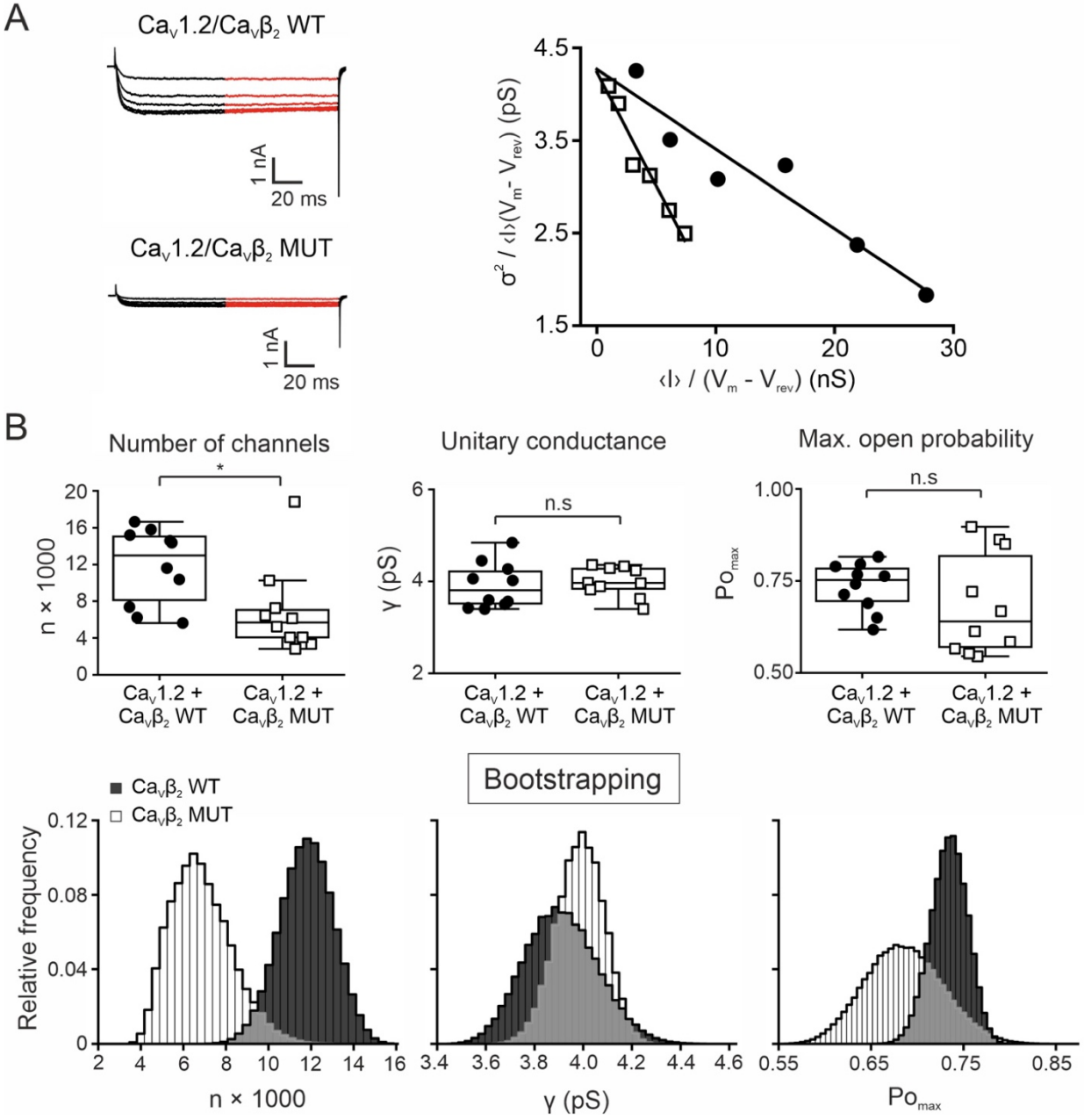
A
Ca$_V$1.2/Ca$_V$β$_2$ WT
1 nA
20 ms
Ca$_V$1.2/Ca$_V$β$_2$ MUT
1 nA
20 ms
σ^2 / ‹I›(V$_m$ - V$_{rev}$) (pS)
‹I› / (V$_m$ - V$_{rev}$) (nS)
B
Number of channels
n × 1000
Ca$_V$1.2 + Ca$_V$β$_2$ WT
Ca$_V$1.2 + Ca$_V$β$_2$ MUT
Unitary conductance
γ (pS)
n.s
Max. open probability
Po$_{max}$
Bootstrapping
Ca$_V$β$_2$ WT
Ca$_V$β$_2$ MUT
Relative frequency
n × 1000
γ (pS)
Po$_{max}$

Figure 8

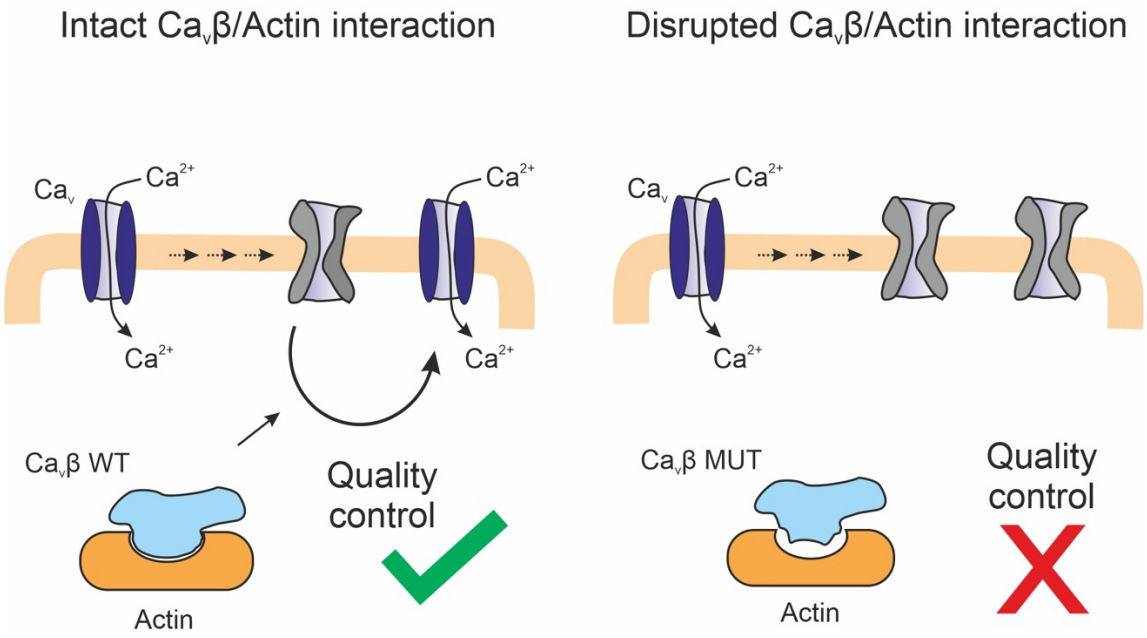
Intact Ca$_v$β/Actin interaction
Disrupted Ca$_v$β/Actin interaction
Ca$_v$
Ca^{2+}
Ca^{2+}
Ca^{2+}
Ca^{2+}
Ca$_v$β WT
Actin
Quality control
Ca$_v$
Ca^{2+}
Ca^{2+}
Ca$_v$β MUT
Actin
Quality control

Supplemental figures

Interaction of $Ca_V\beta$ and actin supports the clearance of functionally defective $Ca_V1.2$ channels

Francisco Castilla, Victor Lugo, Erick Miranda-Laferte, Nadine Jordan, Pitter Huesgen, Beatrix Santiago-Schübel, Mercedes Alfonso-Prieto, Patricia Hidalgo

Supplemental Figure S1. $Ca_V\beta_2$/F-actin model docking data.

Supplemental Figure S2. SDS-PAGE $Ca_V\beta_2$-core/F-actin co-sedimentation assays at different NaCl concentrations.

Supplemental Figure S3. Computational alanine scanning of the $Ca_V\beta_2$/F-actin interface.

Supplemental Figure S4. SDS-PAGE of $Ca_V\beta_2$-core, $Ca_V\beta_2$-core 6Ala and $Ca_V\beta_2$-core 8Ala F-actin co-sedimentation assays and thermal stability of the proteins.

Supplemental Figure S5. Hotspots of $Ca_V\beta_2$ for binding AID site and actin does not overlap and the hotspot mutants bind *in-vitro* to the AID-site.

Supplemental Figure S6. Multiple sequence alignment of $Ca_V\beta_2$ and $Ca_V\beta_4$ showing conservation of residues involved in crosslinks.

Supplemental Figure S7. $Ca_V\beta_4$/F-actin model docking data.

Supplemental Figure S8. Computational alanine scanning of the $Ca_V\beta_4$/F-actin interface.

Supplemental Figure S9. Comparison of F-actin co-sedimentation assays for $Ca_V\beta_4$-core and $Ca_V\beta_4$ R482X and pull down assay of the $Ca_V\beta_4$ R482X hotspots for actin binding, $Ca_V\beta_4$ R482X 6Ala and $Ca_V\beta_4$ R482X 8Ala, with GST-AID.

Supplemental Figure S10. SDS-PAGE of F-actin co-sedimentation assays for $Ca_V\beta_4$ R482X and the mutants $Ca_V\beta_4$ R482X 6Ala and $Ca_V\beta_4$ R482X 8Ala and thermal stability of the proteins.

Supplemental Figure S11. Comparison by Western Blot analysis of the cellular expression levels of wild-type $Ca_V\beta_2$-core and mutant $Ca_V\beta_2$-core 8Ala bearing eight substitutions to alanine in hotspots for actin binding.

Supplemental Figure S1

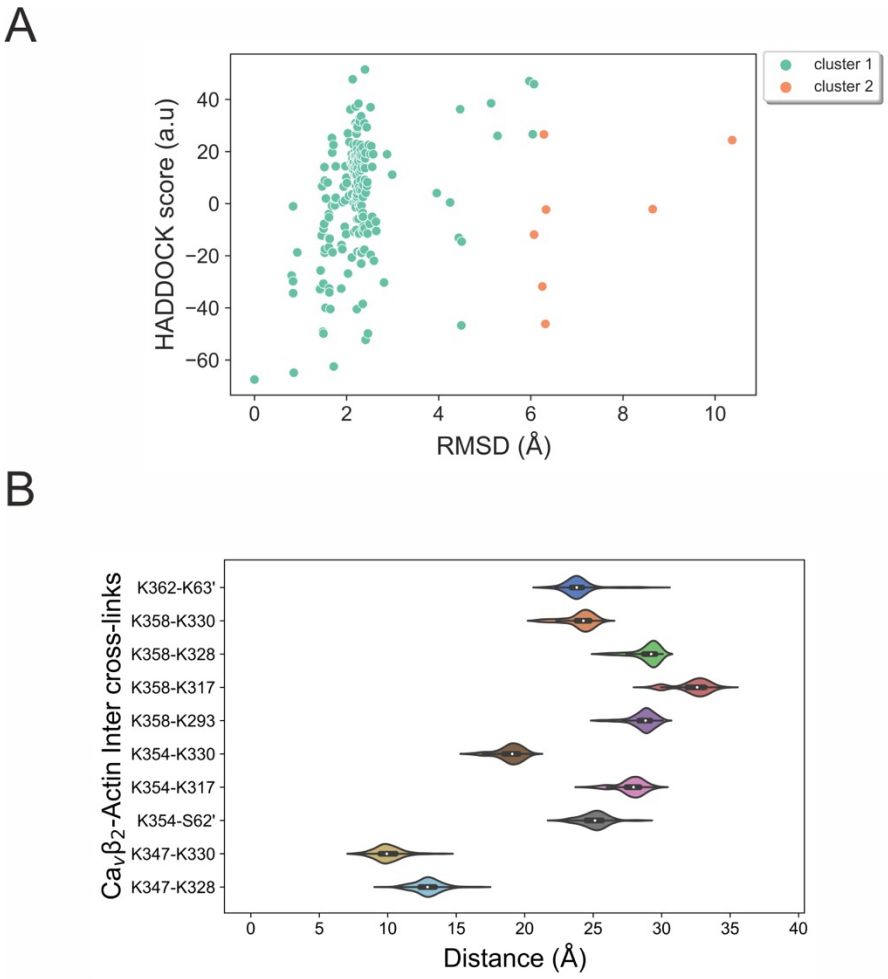

Figure S1. $Ca_V\beta_2$/F-actin model docking data. A, HADDOCK score versus interface RMSD plot. B, Mapped Euclidean C_α-C_α cross-linked pair distance distribution for all the structures belonging to the best cluster generated by HADDOCK 2.4 for $Ca_V\beta_2$/F-actin model.

Supplemental Figure S2

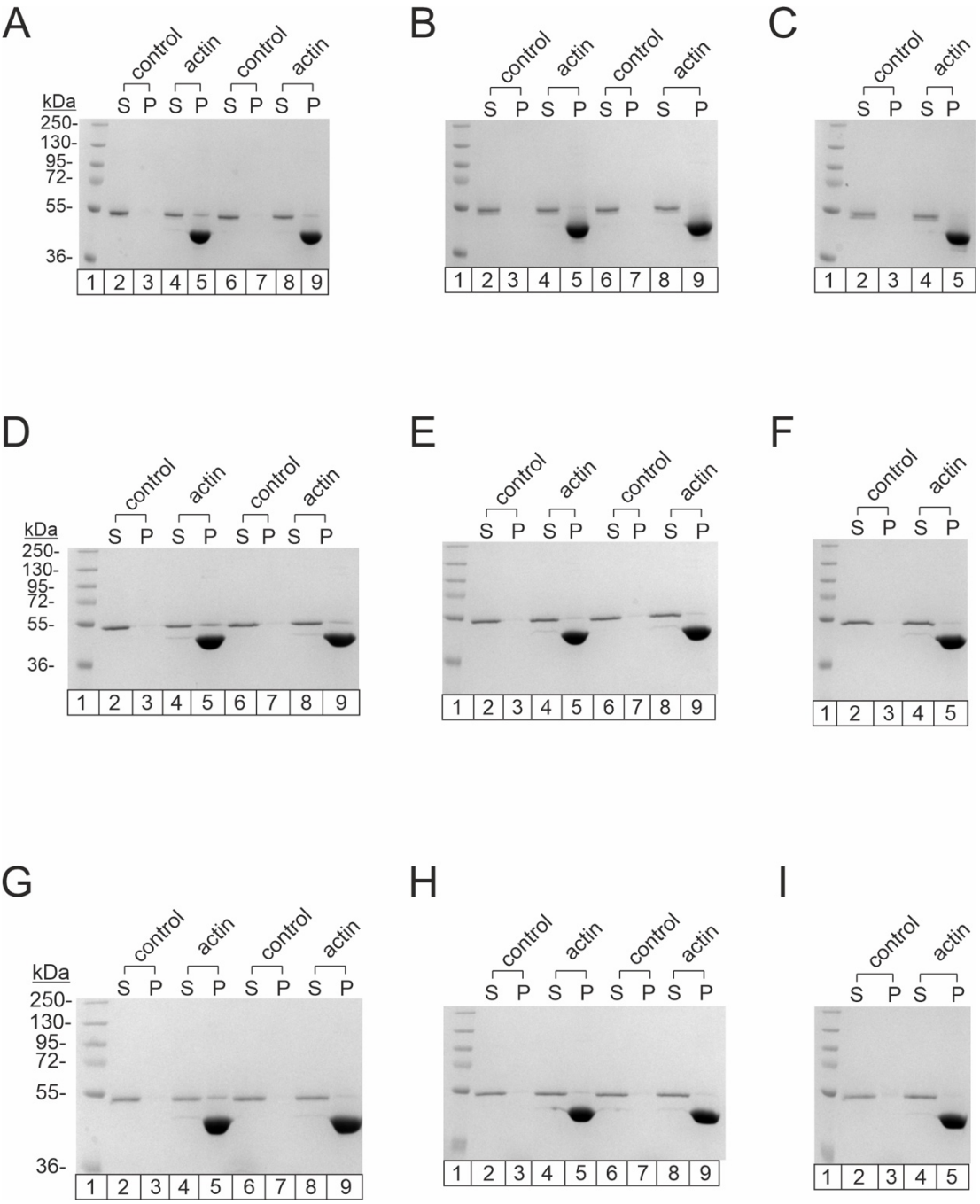

Figure S2. SDS-PAGE gels of Ca_vβ2-core/F-actin co-sedimentation assays at different NaCl concentrations. Analysis of gels: A, lane1: Molecular weight standards; lane 2: Supernatant Ca_vβ2-core 30 mM NaCl; lane 3: Pellet Ca_vβ2-core 30 mM NaCl; lane 4: Supernatant Ca_vβ2-core/F-actin 30 mM NaCl; lane 5: Pellet Ca_vβ2-core/F-actin 30 mM NaCl; lane 6: Supernatant Ca_vβ2-core 60 mM NaCl; lane 7: Pellet Ca_vβ2-core 60 mM NaCl; lane 8: Supernatant Ca_vβ2-core/F-actin 60 mM NaCl; lane 9: Pellet Ca_vβ2-core/F-actin 60 mM NaCl.

B, same scheme applies but for 90 (lanes 2-5) and 120 mM (lanes 6-9) NaCl. C, same scheme applies but for 150 mM NaCl (lanes 2-5). Panels D-F and G-I correspond to replica experiments using the same conditions as panels *A*-*C*.

Supplemental Figure S3

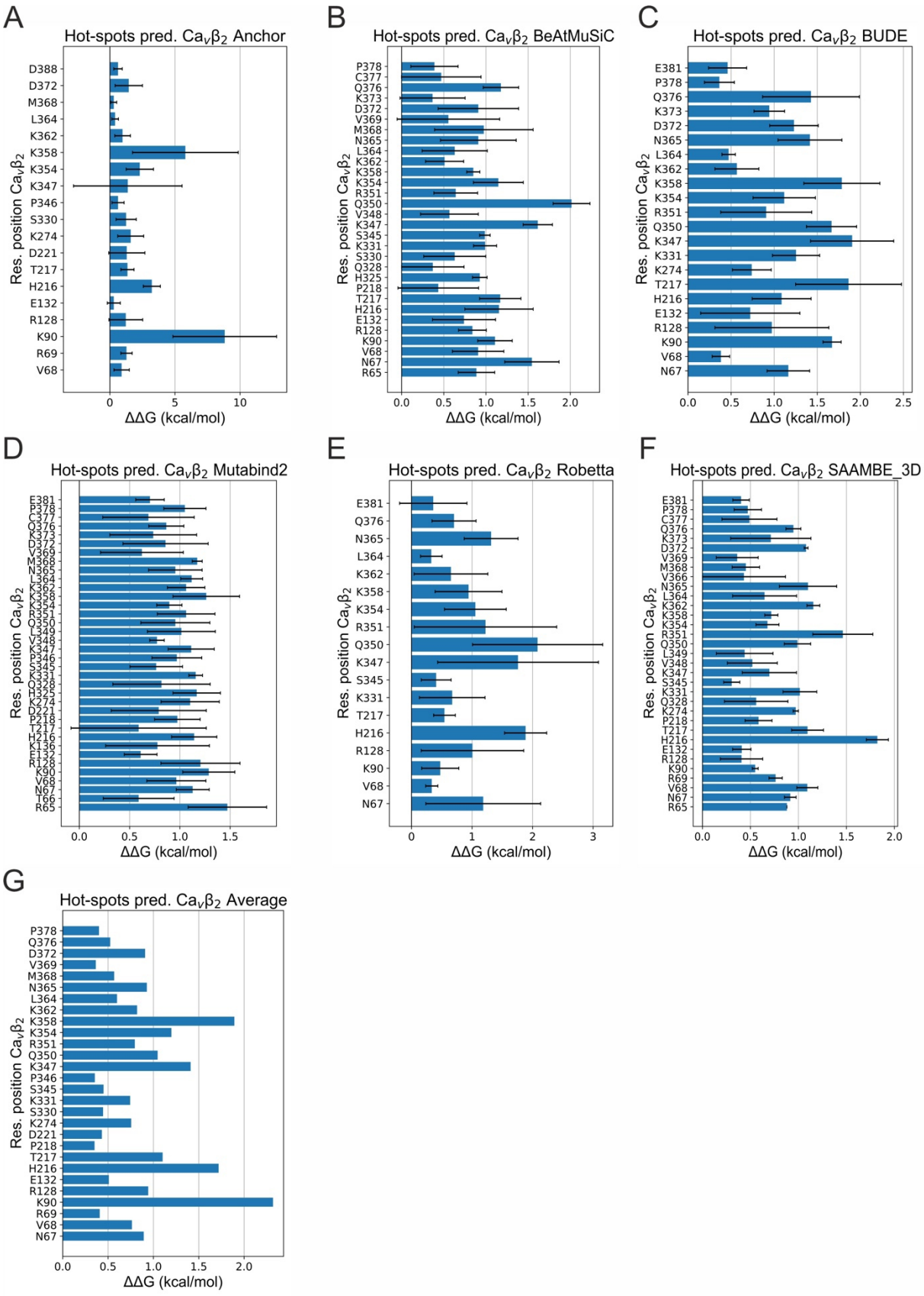

Figure S3. Computational alanine scanning of the $Ca_V\beta_2$/F-actin interface. A set of 6 webservers: Anchor (A), BeAtMuSiC (B), BUDE (C), Mutabind2 (D), Robetta (E) and SAAMBE-3D (F) were used to the predict hot-spots in the $Ca_V\beta_2$/F-actin interface, using the top four structures of the best docking cluster. For each predictor, changes in binding free energy upon Ala mutation of the corresponding $Ca_V\beta_2$ residue (ΔΔG) were averaged over the four docking models. (G) ΔΔG values averaged over all six predictors. Only mutations resulting in a ΔΔG higher than 0.3 kcal/mol are shown. The error bars correspond to the standard deviation.

Supplemental Figure S4

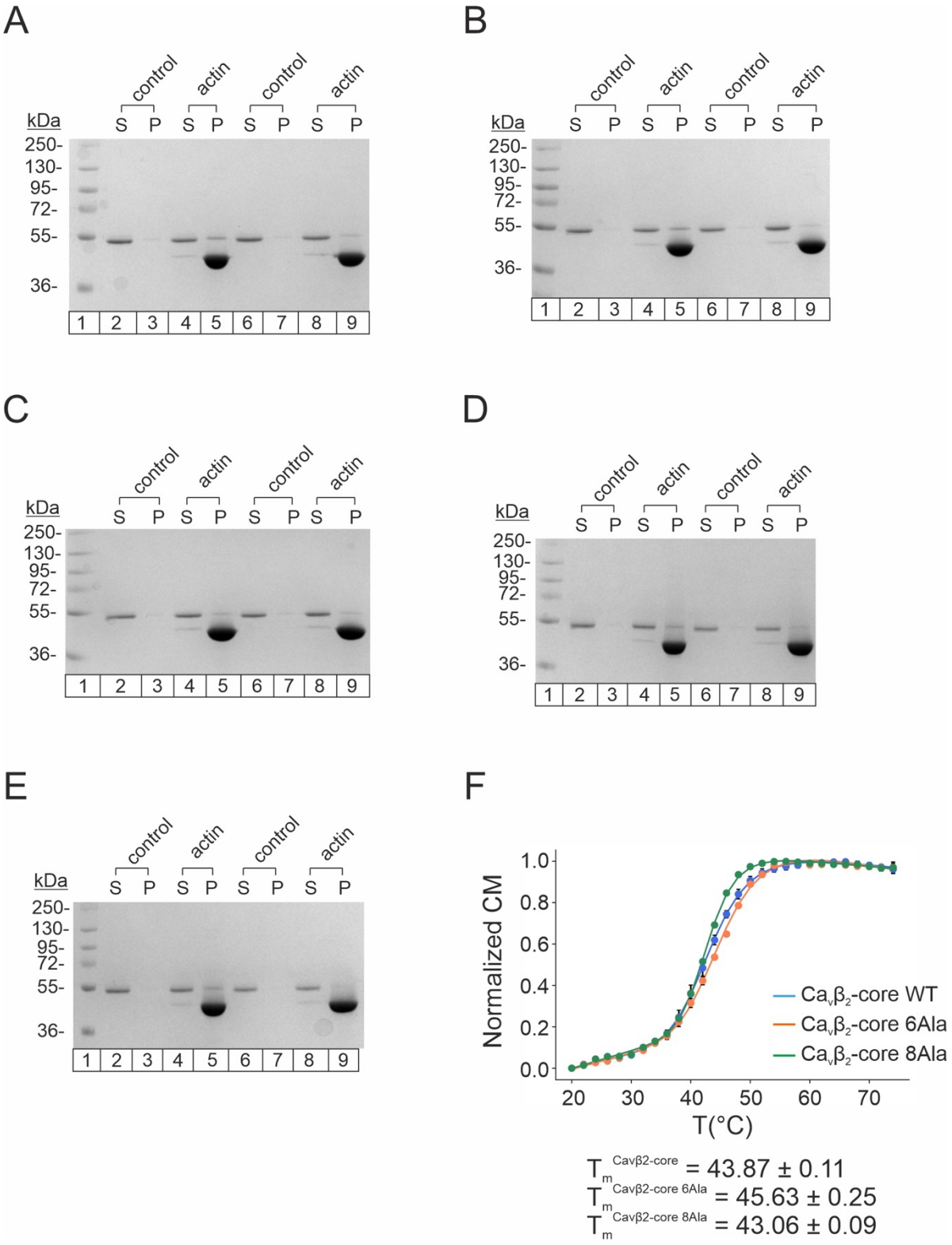

Figure S4. SDS-PAGE of $Ca_v\beta2$-core, $Ca_v\beta2$-core 6Ala and $Ca_v\beta2$-core 8Ala F-actin co-sedimentation assays and thermal stability of the proteins. Analysis of gels: A, lane1:

Molecular weight standards; lane 2: Supernatant $Ca_v\beta2$-core; lane 3: Pellet $Ca_v\beta2$-core; lane 4: Supernatant $Ca_v\beta2$-core/F-actin; lane 5: Pellet $Ca_v\beta2$-core/F-actin; lane 6: Supernatant $Ca_v\beta2$-core 6Ala; lane 7: Pellet $Ca_v\beta2$-core 6Ala; lane 8: Supernatant $Ca_v\beta2$-core/F-actin 6Ala; lane 9: Pellet $Ca_v\beta2$-core/F-actin 6Ala. B, lane1: Molecular weight standards; lane 2: Supernatant $Ca_v\beta2$-core; lane 3: Pellet $Ca_v\beta2$-core; lane 4: Supernatant $Ca_v\beta2$-core/F-actin; lane 5: Pellet $Ca_v\beta2$-core/F-actin; lane 6: Supernatant $Ca_v\beta2$-core 8Ala; lane 7: Pellet $Ca_v\beta2$-core 8Ala; lane 8: Supernatant $Ca_v\beta2$-core/F-actin 8Ala; lane 9: Pellet $Ca_v\beta2$-core/F-actin 8Ala. C, lane1: Molecular weight standards; lane 2: Supernatant $Ca_v\beta2$-core 6Ala; lane 3: Pellet $Ca_v\beta2$-core 6Ala; lane 4: Supernatant $Ca_v\beta2$-core/F-actin 6Ala; lane 5: Pellet $Ca_v\beta2$-core/F-actin 6Ala; lane 6: Supernatant $Ca_v\beta2$-core 8Ala; lane 7: Pellet $Ca_v\beta2$-core 8Ala; lane 8: Supernatant $Ca_v\beta2$-core/F-actin 8Ala; lane 9: Pellet $Ca_v\beta2$-core/F-actin 8Ala. D, same as for *A*. E, same as for *B*. F, Thermal unfolding curves for $Ca_v\beta2$-core, $Ca_v\beta2$-core 6Ala and $Ca_v\beta2$-core 8Ala.

Supplemental Figure S5

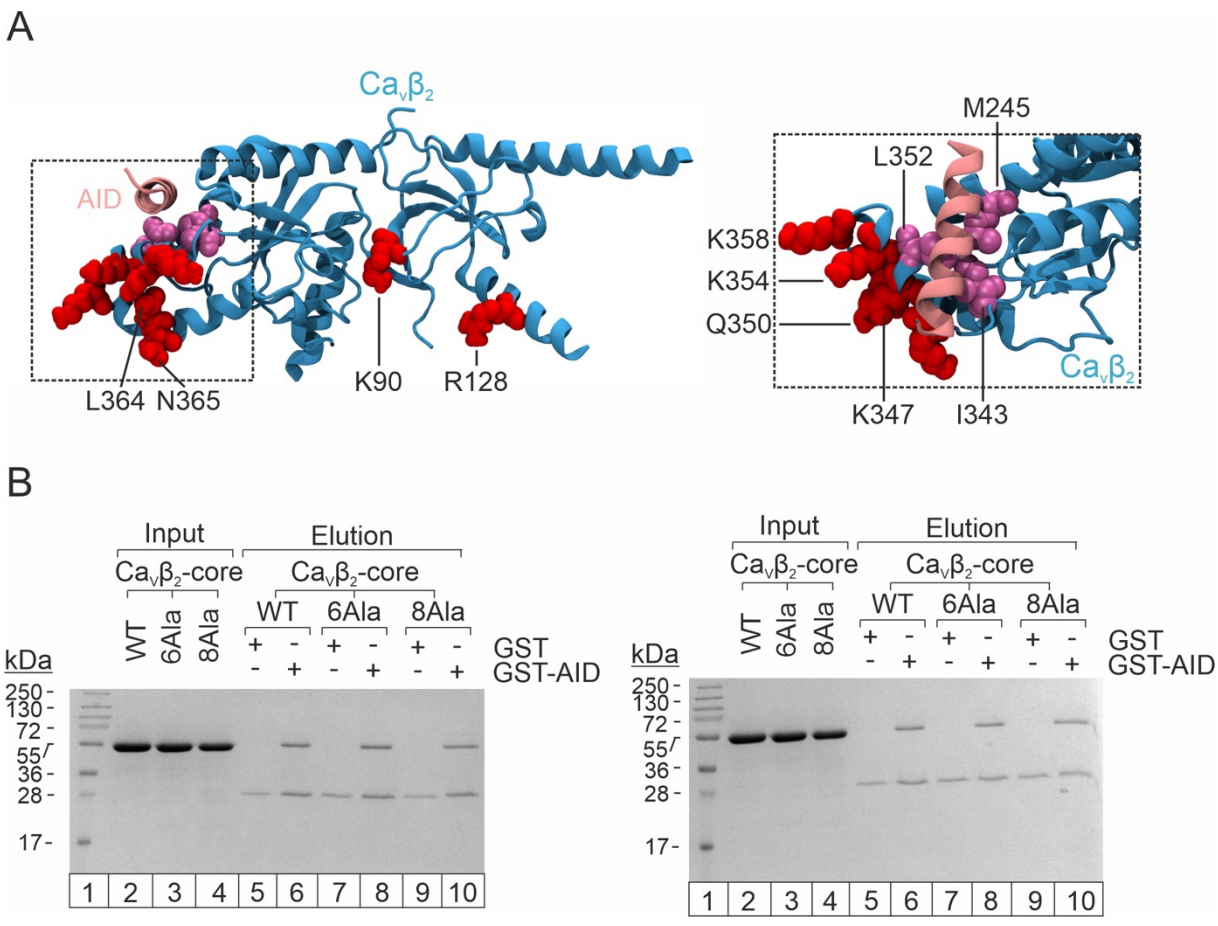

Figure S5. Hotspots of $Ca_V\beta_2$ for binding AID site and actin do not overlap and the hotspot mutants bind *in-vitro* to the AID-site. A, $Ca_V\beta_2$ structure (PDB 5V2P) is depicted as a blue ribbon with the hotspots for actin binding in red van der Waals spheres while AID is depicted as a pink ribbon with their associate hotspots in dark pink. B, SDS-PAGE gels of GST-AID pull down assay of $Ca_V\beta$2-core and the mutants. Analysis: lane 1: Molecular weight standards; lanes 2-4: inputs for $Ca_V\beta$2-core, Cavβ2-core 6Ala and $Ca_V\beta$2-core 8Ala respectively; lane 5: Elution for $Ca_V\beta$2-core/GST; lane 6: Elution for $Ca_V\beta$2-core/GST-AID; lane 7: Elution for $Ca_V\beta$2-core 6Ala/GST; lane 8: Elution for $Ca_V\beta$2-core 6Ala/GST-AID; lane 9: Elution for $Ca_V\beta$2-core 9Ala/GST; lane 10: Elution for $Ca_V\beta$2-core/GST-AID. D, same as for *C*.

Supplemental Figure S6

```
Q8VGC3-2      --------------------------------MQCCGLVHRRRVRVSRGSADSYTSRPS  27
O00305-1      MSSSSYAKNGTADGPHSPTSQVARGTTTRRSRLKRSDGSTTSTSFILRQGSADSYTSRPS  60
                                              :. * .    . : :***********

Q8VGC3-2      DSDVSLEEDREAVRREAERQAQAQLEKAKTKPVAFAVRTNVRYSAAQEDDVPVPGMAISF  87
O00305-1      DSDVSLEEDREAIRQEREQQAAIQLERAKSKPVAFAVKTNVSYCGALDEDVPVPSTAISF  120
              ************:*:* *:**  ***:**:*******:*** *..* ::*****. ****

Q8VGC3-2      EAKDFLHVKEKFNNDWWIGRLVKEGCEIGFIPSPVKLENMRLQHEQRAKQGKFYSSKSGG  147
O00305-1      DAKDFLHIKEKYNNDWWIGRLVKEGCEIGFIPSPLRLENIRIQQEQ--KRGRFHGGKSSG  178
              :******:***:**********************::***:*:*:**  *:*:*:..**.*

Q8VGC3-2      NSSSSLGDIVPSSRKSTPPSSAIDIDATGLDAEENDIPANHRSPKPSANSVTSPHSKEKR  207
O00305-1      NSSSSLGEMVSGTFRATPTSTAK-----------------------------------  201
              *******::* .: ::** *:*

Q8VGC3-2      MPFFKKTEHTPPYDVVPSMRPVVLVGPSLKGYEVTDMMQKALFDFLKHRFEGRISITRVT  267
O00305-1      -QKQKVTEHIPPYDVVPSMRPVVLVGPSLKGYEVTDMMQKALFDFLKHRFDGRISITRVT  260
                  * *** ****************************************:*********

Q8VGC3-2      ADISLAKRSVLNNPSKHAIIERSNTRSSLAEVQSEIERIFELARTLQLVVLDADTINHPA  327
O00305-1      ADISLAKRSVLNNPSKRAIIERSNTRSSLAEVQSEIERIFELARSLQLVVLDADTINHPA  320
              ****************:****************************:***************

                                x     x   x   x
Q8VGC3-2      QLSKTSLAPIIVYVKISSPKVLQRLIKSRGKSQAKHLNVQMVAADKLAQCPPQESFDVIL  387
O00305-1      QLIKTSLAPIIVHVKVSSPKVLQRLIKSRGKSQSKHLNVQLVAADKLAQCPP-EMFDVIL  379
              ** *********:**:*****************:******:********** * *****

Q8VGC3-2      DENQLEDACEHLADYLEAYWKATHPPSSNLPNPLLSRTLATSTLPLSPTLASNSQGSQGD  447
O00305-1      DENQLEDACEHLGEYLEAYWRATHTTSSTPMTPLLGRNLGSTALSPYPTAISGLQSQRMR  439
              ************.:******:***  **.  .***.*.*.:::*   **  *. *..:

Q8VGC3-2      QRTDRSAPRSASQAEEEPCLEPVKKSQHRSSSATHQNHRSGTGRGLSRQETFDSETQESR  507
O00305-1      HS-NHS-------TENS----PIERRSLMTSDENYHNERAR-----KSRNRLSSSSQHS-  481
              :  ::*       :*:.    *::: .  :*. .::*.*:      . :: :.*.:*.*

Q8VGC3-2      DSAYVEPKEDYSHEHVDRYVPHREHNHREESHSSNGHRHREPRHRTRDMGRDQDHNECSK  567
O00305-1      RDHYPLVEEDYPDSYQDTYKPHRNRGSPGGYSH-------DSRHRL--------------  520
               . *   :*** ..: * * ***::.              : ***

Q8VGC3-2      QRSRHKSKDRYCDKEGEVISKRRSEAGEWNRDVYIRQ  604
O00305-1      -----------------------------------  520
```

Figure S6. Multiple sequence aligment of $Ca_V\beta_2$ and $Ca_V\beta_4$ showing conservation of residues involved in crosslinks. $Ca_V\beta_2$ (UniProtKB Q8VGC3-2) and $Ca_V\beta_4$ (UniProtKB O00305.2) sequences were aligned using Clustal Omega. The SH3 and GK domains are shown with bright and dark cyan backgrounds, respectively. The inter-molecular cross-links are indicated with an orange 'X', while the mutated hotspots residues are displayed in red bold font.

Supplemental Figure S7

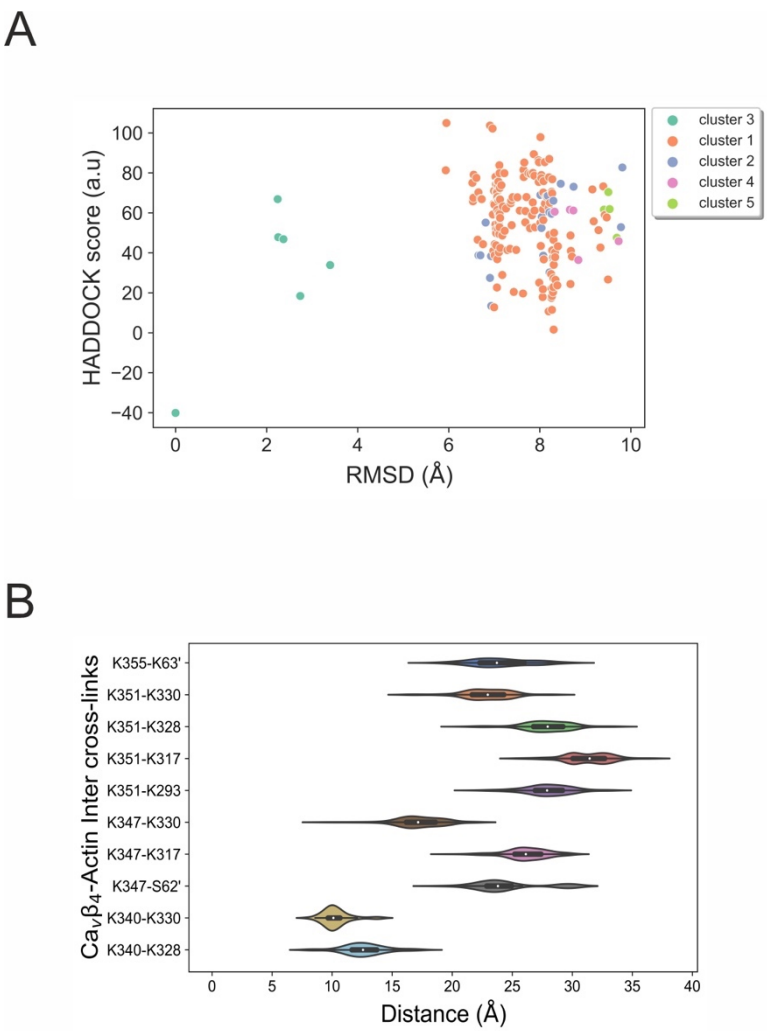

Figure S7. $Ca_V\beta_4$/F-actin model docking data. A, HADDOCK score versus interface RMSD plot. B, Mapped Euclidean C_α-C_α cross-linked pair distance distribution for all the structures belonging to the best cluster generated by HADDOCK 2.4 for $Ca_V\beta_4$/F-actin model.

Supplemental Figure S8

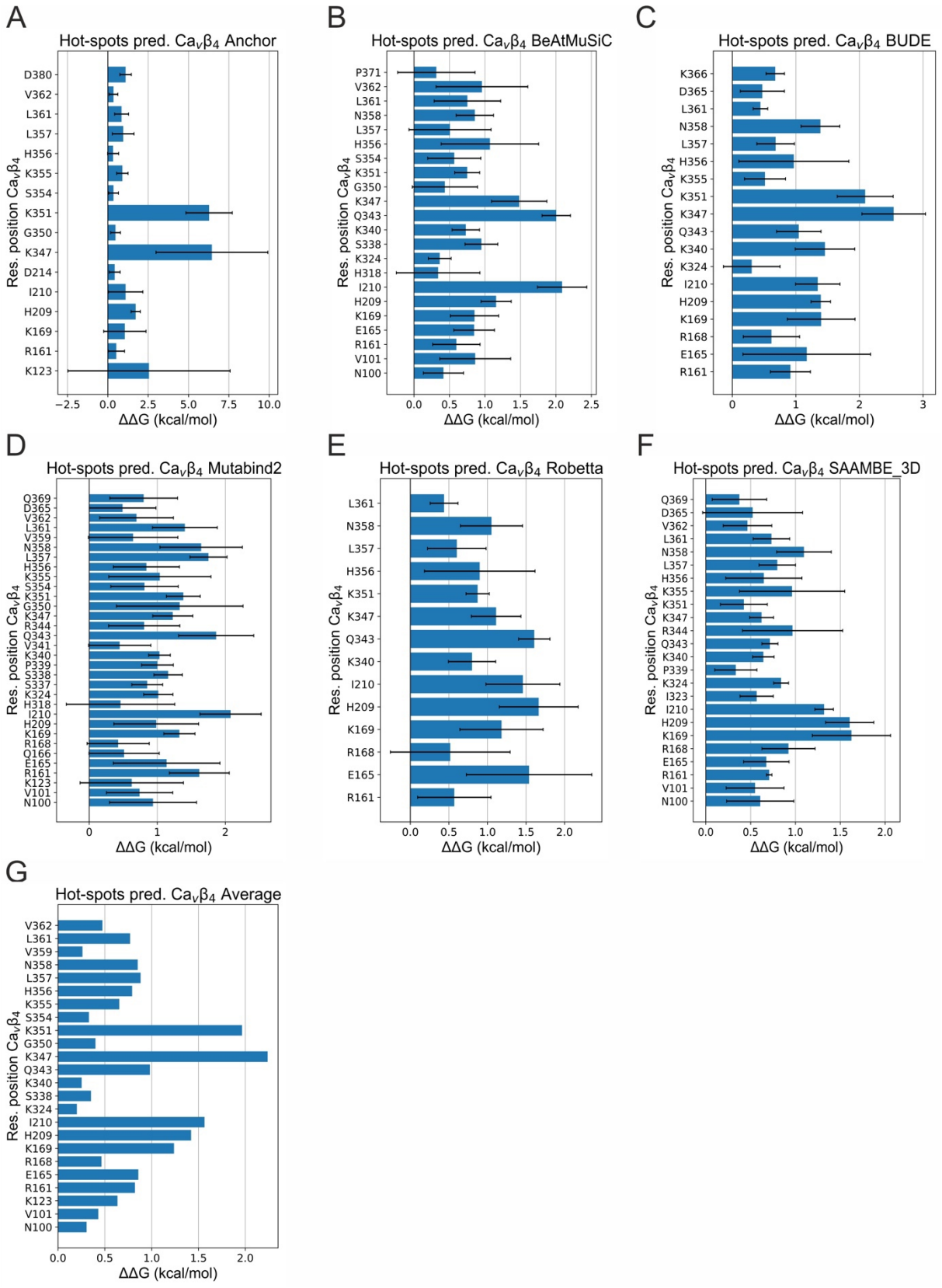

Figure S8. Computational alanine scanning of the $Ca_V\beta_4$/F-actin interface. A set of 6 programs: Anchor (A), BeAtMuSiC (B), BUDE (C), Mutabind2 (D), Robetta (E) and SAAMBE_3D (F) were used to the predict hotspots in the $Ca_V\beta_4$/F-actin interface using the top four structures of the best docking cluster. For each predictor, changes in binding free energy upon Ala mutation of the corresponding $Ca_V\beta_4$ residue (ΔΔG) were averaged over the four docking models. (G) ΔΔG values averaged over all six predictors. Only mutations resulting in a ΔΔG change higher than 0.3 kcal/mol are shown. The error bars correspond to the standard deviation.

Supplemental Figure S9

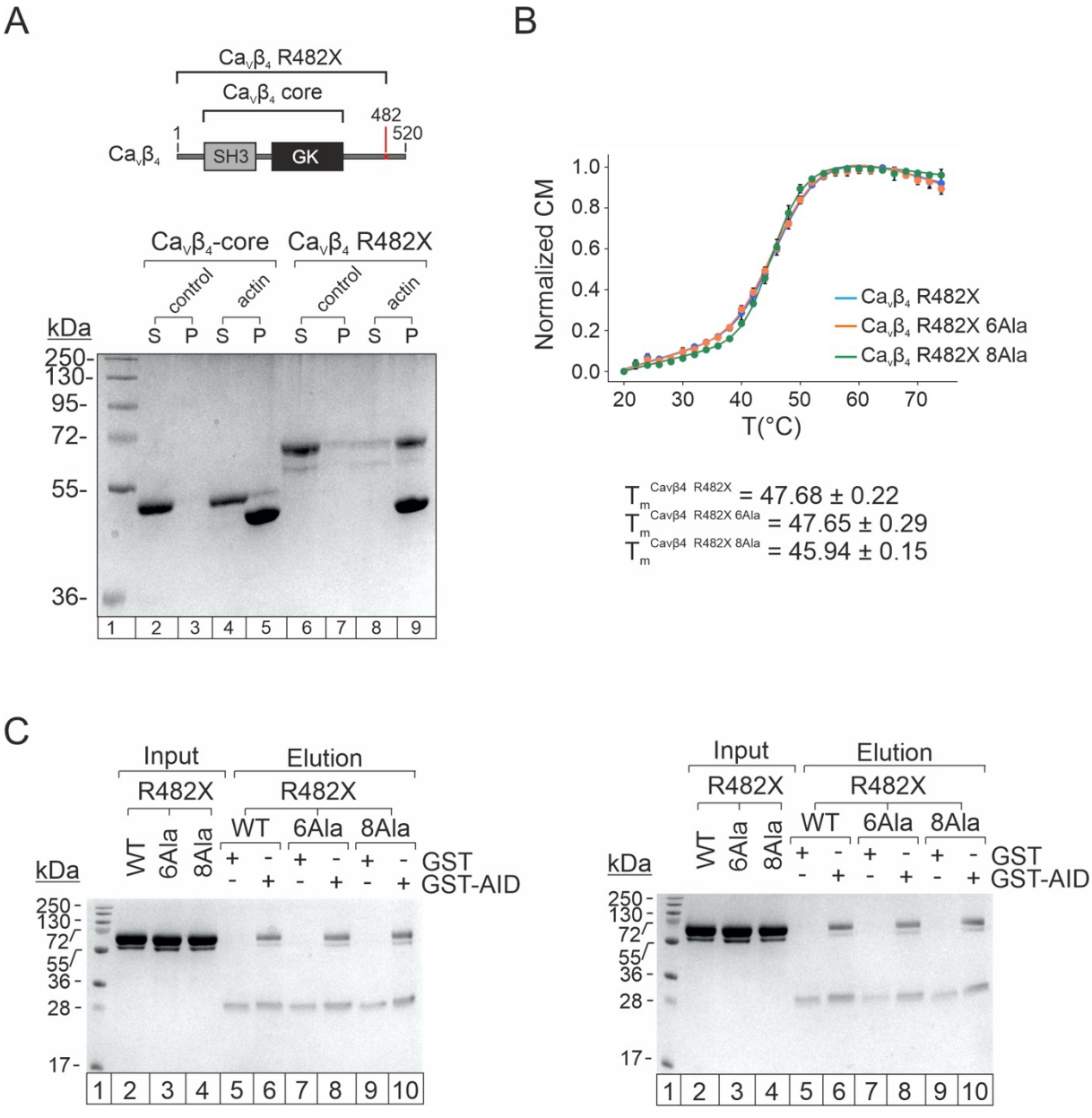

Figure S9. Comparison of F-actin co-sedimentation assays for $Ca_V\beta_4$-core and $Ca_V\beta_4$ R482X and pull down assay of the $Ca_V\beta_4$ R482X hotspots for F-actin binding, $Ca_V\beta_4$ R482X 6Ala and $Ca_V\beta_4$ R482X 8Ala, with GST-AID. A, Schematic linear representation of the domain architecture of $Ca_V\beta_4$ (UniProtKB O00305.2). SDS-PAGE of $Ca_v\beta_4$-core and $Ca_v\beta_4$ R482X actin cosedimentation assays. Analysis of gels: A, lane 1: Molecular weight standards; lane 2: Supernatant $Ca_v\beta_4$-core; lane 3: Pellet $Ca_v\beta_4$-core; lane 4: Supernatant $Ca_v\beta_4$-core/F-actin; lane 5: Pellet $Ca_v\beta_4$-core/F-actin; lane 6: Supernatant $Ca_V\beta_4$ R482X; lane 7: Pellet $Ca_V\beta_4$ R482X; lane 8: Supernatant $Ca_V\beta_4$ R482X/F-actin; lane 9: Pellet $Ca_V\beta_4$ R482X/F-actin. B, Thermal unfolding curves for $Ca_V\beta_4$ R482X, $Ca_V\beta_4$ R482X 6Ala and $Ca_V\beta_4$ R482X 8Ala. C, SDS-PAGE gels of GST-AID pull down assay of $Ca_V\beta_4$ R482X and the mutants. Analysis: lane 1: Molecular weight standards; lanes 2-4: inputs for $Ca_V\beta_4$ R482X, $Ca_V\beta_4$ R482X 6Ala and $Ca_V\beta_4$ R482X 8Ala respectively; lane 5: Elution for $Ca_V\beta_4$ R482X/GST; lane 6: Elution for $Ca_V\beta_4$ R482X/GST-AID; lane 7: Elution for $Ca_V\beta_4$ R482X 6Ala/GST; lane 8: Elution for $Ca_V\beta_4$ R482X 6Ala/GST-AID; lane 9: Elution for $Ca_V\beta_4$ R482X 9Ala/GST; lane 10: Elution for $Ca_V\beta_4$ R482X/GST-AID.

Supplemental Figure S10

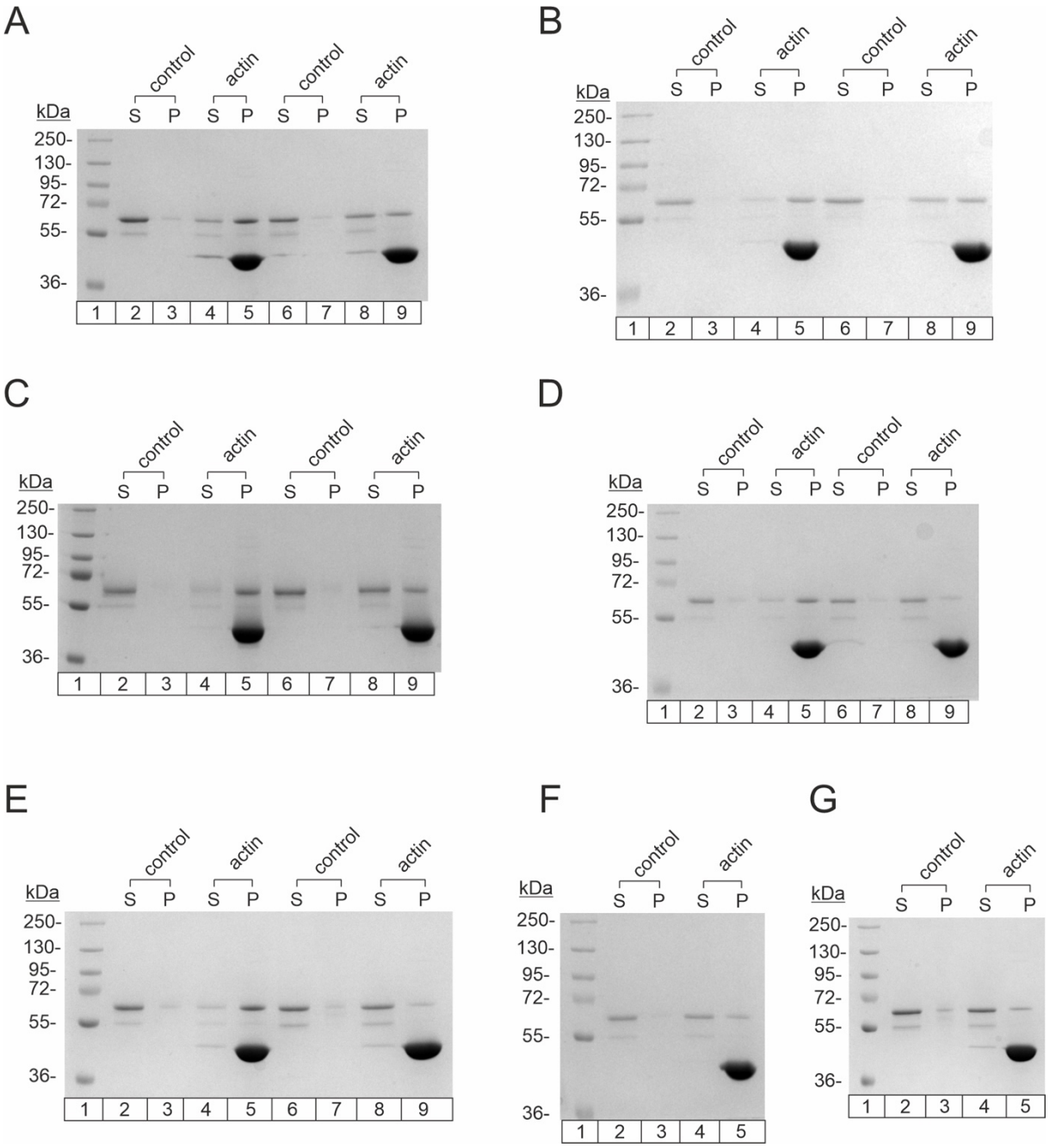

Figure S10. SDS-PAGE gels of $Ca_V\beta_4$ R482X, $Ca_V\beta_4$ R482X 6Ala and $Ca_V\beta_4$ R482X 8Ala F-actin co-sedimentation assays. Analysis of gels: A, lane 1: Molecular weight standards; lane 2: Supernatant $Ca_V\beta_4$ R482X; lane 3: Pellet $Ca_V\beta_4$ R482X; lane 4: Supernatant $Ca_V\beta_4$ R482X/F-actin; lane 5: Pellet $Ca_V\beta_4$ R482X/F-actin; lane 6: Supernatant $Ca_V\beta_4$ R482X 6Ala; lane 7: Pellet $Ca_V\beta_4$ R482X 6Ala; lane 8: Supernatant $Ca_V\beta_4$ R482X 6Ala/F-actin; lane 9: Pellet $Ca_V\beta_4$ R482X 6Ala/F-actin. B and C, same as for *A*. D, lane 1: Molecular weight standards; lane 2: Supernatant $Ca_V\beta_4$ R482X; lane 3: Pellet $Ca_V\beta_4$ R482X; lane 4: Supernatant

$Ca_V\beta_4$ R482X/F-actin; lane 5: Pellet $Ca_V\beta_4$ R482X/F-actin; lane 6: Supernatant $Ca_V\beta_4$ R482X 8Ala; lane 7: Pellet $Ca_V\beta_4$ R482X 8Ala; lane 8: Supernatant $Ca_V\beta_4$ R482X 8Ala/F-actin; lane 9: Pellet $Ca_V\beta_4$ R482X 8Ala/F-actin. E, same as for *D*. F, lane 1: Molecular weight standards; lane 2: Supernatant $Ca_V\beta_4$ R482X 6Ala; lane 3: Pellet $Ca_V\beta_4$ R482X 6Ala; lane 4: Supernatant $Ca_V\beta_4$ R482X 6Ala/F-actin; lane 5: Pellet $Ca_V\beta_4$ R482X 6Ala/F-actin. G, same as *F* but for $Ca_V\beta_4$ R482X 8Ala.

Supplemental Figure S11

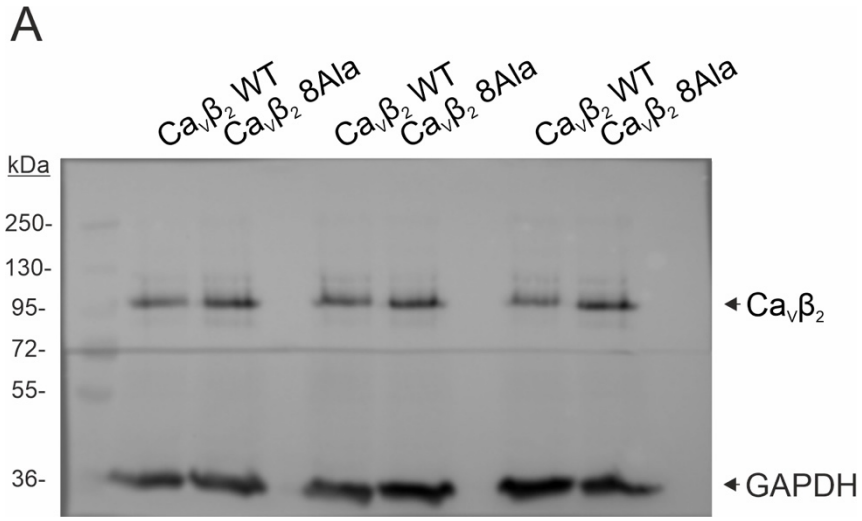

Figure S11. Comparison by Western Blot analysis of the cellular expression levels of wild-type $Ca_V\beta_2$ and mutant $Ca_V\beta_2$ 8Ala bearing eight substitutions to alanine in hotspots for actin binding. A, Triplicate whole cell lysate of $Ca_V\beta_2$ WT and $Ca_V\beta_2$ 8Ala using GAPDH as loading control.

Supplemental Tables

Interaction of $Ca_V\beta$ and actin supports the clearance of functionally defective $Ca_V1.2$ channels

Francisco Castilla, Victor Lugo, Erick Miranda-Laferte, Nadine Jordan, Pitter Huesgen, Beatrix Santiago-Schübel, Mercedes Alfonso-Prieto, Patricia Hidalgo

Supplemental Table S1. Total number of inter molecular cross-links identified with DSSO and DSBU crosslinkers.

Supplemental Table S2. Data-consistency and violation analysis of XL-MS data performed with DisVis.

Supplemental Table S3. HADDOCK docking data and statistics for $Ca_V\beta_2$/F-actin and $Ca_V\beta_4$/F-actin model docking data.

Supplemental Table S1

XL-pair ID	Precursor m/z	charge (z+)	Crosslinker	Type	Sequence Actin	Position	Sequence CaVβ2	Position in recombinant protein ß2-core	Corresponding position Uniprot Q8VGC3-2	Merox	MaxLynx	Metamorpheus
1	577.097	4	DSBU	inter	I**K**IIAPPER	330	VTADISLA**K**R	284	274	2	2	2;3
2	565.595	4	DSBU	inter	I**K**IIAPPER	330	ISSP**K**VLQR	357	347	1;3	1;2;3	1;2;3;4
3	462.792	4	DSBU	inter	I**K**IIAPPER	330	LI**K**SR	364	354	1	-	1;3
4	661.131	4	DSBU	inter	EITALAPSTM**K**IK	328	ISSP**K**VLQR	357	347	1	-	1;3
5	453.271	4	DSSO	inter	I**K**IIAPPER	330	ILI**K**SR	364	354	12;13;14;15	13;15	12;13;14;15;16
6	453.756	4	DSSO	inter	I**K**IIAPPERK	330	G**K**SQAK	368	358	12;	-	12;13;15
7	549.292	4	DSSO	inter	EITALAPSTM**K**IK	328	GKSQAK	368	358	12;	12;15	12;15
8	585.308	4	DSSO	inter	MQ**K**EITALAPSTMK	317	LI**K**SR	364	354	12;	12;13;15	12;13;15;16
9	523.764	4	DSSO	inter	DSYVGDEAQS**K**R	63	LI**K**SR	364	354	12;	12;13;15	12;13;15
10	741.095	3	DSSO	inter	I**K**IIAPPER	330	ISSP**K**VLQR	357	347	13	13	13
11	792.623	4	DSSO	inter	DSYVGDEAQS**K**R	63	SQA**K**HLNVQMVAADK	372	362	-	12	12
12	796.119	4	DSSO	inter	KDLYANNVMSGGTTMYPGIADR	293	G**K**SQAK	368	358	-	12	12
13	703.044	3	DSSO	inter	EITALAPSTM**K**IK	328	A**K**QGK	146	136	-	12	12
14	589.794	4	DSSO	inter	MQ**K**EITALAPSTMK	317	G**K**SQAK	368	358	-	12;15	12;15
15	544.808	4	DSSO	inter	EITALAPSTM**K**IK	328	LI**K**SR	364	354	-	12;15	12;13;15
16	757.046	3	DSSO	inter	MQ**K**EITALAPSTMK	317	A**K**QGK	146	136	-	12	12
17	710.665	3	DSSO	inter	DSYVGDEAQS**K**R	63	G**K**SQAK	368	358	-	-	12;15;16
18	681.654	3	DSSO	inter	DSYVGDEAQS**K**R	63	A**K**QGK	146	136	-	-	12;15
19	789.873	4	DSSO	inter	HQGVMVGMGQ**K**DSYVGDEAQSK	52	LI**K**SR	364	354	-	-	12;13;15
20	692.111	4	DSSO	inter	MQ**K**EITALAPSTMK	317	ISSP**K**VLQR	357	347	-	-	12;13
21	651.611	4	DSSO	inter	EITALAPSTM**K**IK	328	ISSP**K**VLQR	357	347	-	-	12
22	632.492	5	DSSO	inter	HQGVMVGMGQ**K**DSYVGDEAQSK	52	G**K**SQAK	368	358	-	-	12
23	768.603	4	DSSO	inter	HQGVMVGMGQ**K**DSYVGDEAQSK	52	A**K**QGK	146	136	-	-	12
24	663.111	4	DSSO	inter	EITALAPSTM**K**IK	328	VTADISLA**K**R	284	274	-	-	16
25	847.089	3	DSSO	inter	DSYVGDEAQS**K**R	63	ISSP**K**VLQR	357	347	-	-	12;15
26	464.023	3	DSSO	inter	I**K**IIAPPER	330	A**K**QGK	146	136	-	-	12;13;15
27	681.654	3	DSSO	inter	DSYVGDEAQS**K**R	63	A**K**QGK	146	136	-	-	12;15
28	759.606	4	DSSO	inter	DSYVGDEAQS**K**R	63	SPKPSANSVTSPHSK	202	192	-	-	12
29	714.342	5	DSSO	inter	HQGVMVGMGQ**K**DSYVGDEAQSK	52	ISSP**K**VLQR	357	347	-	-	13
30	664.565	4	DSSO	inter	DSYVGDEAQS**K**R	63	ISSP**K**VLQR	357	347	-	-	12;15

Supplemental Table S1. Total number of inter molecular cross-links identified with DSSO and DSBU cross-linkers. This table reports the confident cross-links and its corresponding data. Only cross-links that matched the default scores of the XL-programs were considered.

Supplemental Table S2

#	Restraint	Average violated fraction	Standard deviation	Z-score
1	K328 - K358	0.17	0.23	-0.73
2	K330 - K354	0.18	0.23	-0.68
3	K330 - K358	0.18	0.22	-0.66
4	K293 - K358	0.2	0.22	-0.58
5	K317 - K354	0.23	0.2	-0.42
6	K317 - K358	0.24	0.2	-0.34
7	K328 - K347	0.26	0.23	-0.24
8	K330 - K347	0.28	0.23	-0.13
9	S62' - K354	0.37	0.23	0.38
10	K63' - K362	0.39	0.23	0.48

Supplemental Table S2. Data-consistency and violation analysis of XL-MS data performed with DisVis. Table listing the information for the consistent restraints with Z-scores larger than 1.0. Note that the restraints are defined in this caption as fixed chain/scanning chain (F-actin/$Ca_V\beta_2$), i.e. swapped ordering compared to the main text.

Supplemental Table S3

$Ca_V\beta_2$/Actin

Cluster	HADDOCK score*(a.u)	Cluster size	RMSD (Å)	Van der Waals energy (E_{vdw}) (kcal mol^{-1})	Electrostatic energy (E_{elec}) (kcal mol^{-1})	Desolvation energy (E_{desol}) (kcal mol^{-1})	Restraints violation energy (kcal mol^{-1})	Buried Surface Area (Å^2)	Z-Score
#1	-61.8 ± 5.8	190	1.2 ± 0.9	-82.9 ± 5.6	-468.8 ± 35.6	37.5 ± 2.4	774.2 ± 59.79	3275.4 ± 160.6	-1.0
#2	-23.0 ± 17.1	7	6.2 ± 0.1	-56.7 ± 4.9	-466.3 ± 33.2	28.9 ± 4.1	980.8 ± 53.26	2729.3 ± 113.1	1.0

$Ca_V\beta_4$/Actin

Cluster	HADDOCK score* (a.u)	Cluster size	RMSD (Å)	Van der Waals energy (E_{vdw}) (kcal mol^{-1})	Electrostatic energy (E_{elec}) (kcal mol^{-1})	Desolvation energy (E_{desol}) (kcal mol^{-1})	Restraints violation energy (kcal mol^{-1})	Buried Surface Area (Å^2)	Z-Score
#1	9.1 ± 4.4	157	7.9 ± 0.5	-64.7 ± 4.8	-301.7 ± 45.1	12.7 ± 12.4	1214.3 ± 98.57	2601.2 ± 146.1	-1.2
#3	14.7 ± 33.2	6	2.1 ± 1.3	-66.2 ± 21.4	-403.6 ± 93.3	32.7 ± 2.5	1290.0 ± 87.90	2629.4 ± 547.4	-0.9
#2	27.4 ± 9.0	19	7.2 ± 0.6	-64.7 ± 6.7	-276.9 ± 24.1	27.2 ± 5.8	1201.7 ± 131.07	2605.7 ± 36.6	-0.3
#4	51.0 ± 10.4	5	8.9 ± 0.5	-51.9 ± 7.3	-355.2 ± 75.5	10.5 ± 8.4	1634.2 ± 116.25	2150.8 ± 101.2	0.9
#5	60.4 ± 8.2	4	9.5 ± 0.1	-51.8 ± 2.9	-244.6 ± 23.2	16.7 ± 2.2	1444.4 ± 60.92	2094.6 ± 75.5	1.4

Supplemental Table S3. HADDOCK docking data and statistics for $Ca_V\beta_2$/F-actin and $Ca_V\beta_4$/F-actin model docking data. Results for the $Ca_V\beta_2$/F-actin protein-protein docking performed with HADDOCK 2.4. Clusters are ranked by the average Haddock score of the top four structures.

3.2 Molecular basis of $Ca_V\beta$ dimerization

3.2.1 Deriving structural information on $Ca_V\beta_2$ dimers by XL-MS

Chemical cross-linking and mass spectrometry (XL-MS) was performed to derive structural information to guide a modeling of $Ca_V\beta_2$ dimeric complex. Conventional XL-MS approaches fail to distinguish inter from intra molecular cross-links in dimeric complexes, as both peptides belong to the same protein. To circumvent this limitation, a workflow that involves the stable isotope-labeling of the protein is applied[103]. Such protocol involves mixing two populations of 'light' (^{14}N) and 'heavy' (^{15}N) monomers, so that a hetero dimer (light/heavy) can be formed. Analysis of the homodimer is then carried out with specialized XL-MS software, allowing the identification of 'light' and 'heavy' peptides and thus the discrimination between intra and inter cross-links of a dimeric complex. Here, I have adapted such protocol to achieve the stable isotope-labeling of $Ca_V\beta_2$ with ^{15}N to study the structural characteristics of $Ca_V\beta_2$ dimers.

As shown in previous studies[50] and in the section 3.1 of this thesis, the core of $Ca_V\beta_2$ ($Ca_V\beta_2$-core) is amenable to be recombinantly expressed and purified. Furthermore, $Ca_V\beta_2$-core forms oligomers *in vitro* as demonstrated by BN-PAGE (Figure 3.1A). In order to study $Ca_V\beta_2$ dimerization by XL-MS, $Ca_V\beta_2$-core was stably labeled with ^{15}N. ^{15}N-$Ca_V\beta_2$-core was expressed recombinantly in *E. coli* in minimal medium supplemented with ^{15}N-NH_4Cl and purified by affinity and size exclusion chromatography (SEC).

In order to confirm the proper stable labeling, ^{14}N-$Ca_V\beta_2$-core and ^{15}N-$Ca_V\beta_2$-core experimental masses were determined by MS in a Q-TOF spectrometer. Masses of 48207 ± 4 Da and 48810 ± 2.7 Da were estimated for ^{14}N-$Ca_V\beta_2$-core and ^{15}N-$Ca_V\beta_2$-core respectively (Figure S3.1, Table S3.1 and Table S3.2). This difference in mass is consistent with the 613 nitrogens present in $Ca_V\beta_2$-core, indicating a high labeling efficiency.

To ensure a proper mix and formation of heterodimers (light/heavy), ^{14}N-$Ca_V\beta_2$-core and ^{15}N-$Ca_V\beta_2$-core were incubated together in a denaturing buffer and then refolded by sequential dialysis. $Ca_V\beta_2$-core dimers were then chemically cross-linked using DSS and resolved by denaturing SDS-PAGE. Although the reaction efficiency was low, a sufficient cross-linked dimeric band was obtained (Figure 3.1B).

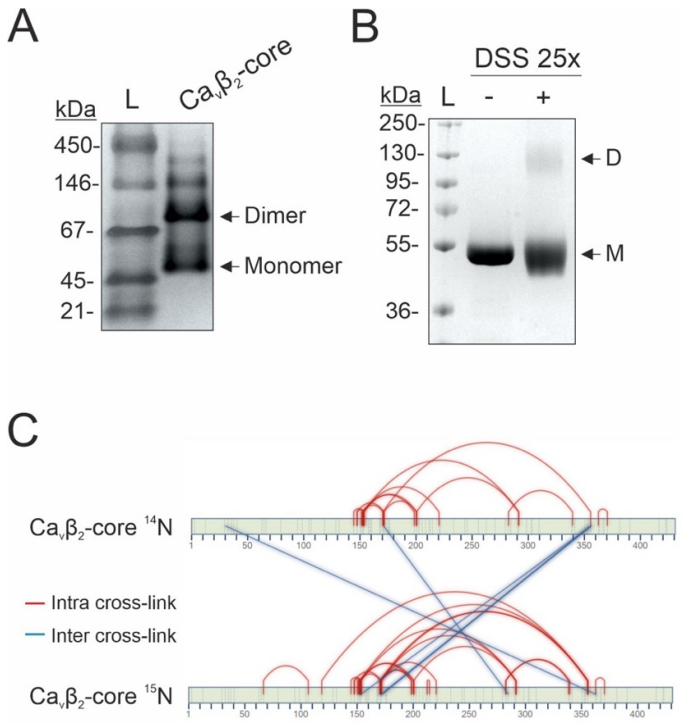

Figure 3.1. $Ca_V\beta_2$-core chemical cross-linking. A) BN-PAGE of $Ca_V\beta_2$-core shows a clear oligomerization pattern. Monomeric and dimeric bands are properly separated. **B)** SDS-PAGE of DSS chemically cross-linked samples of a heavy/light mix of $Ca_V\beta_2$-core. M: monomer; D: dimer. A dimeric cross-linked band was identified, which was subsequently excised, processed, and analyzed by MS. **C)** Heavy/light $Ca_V\beta_2$-core cross-linking map after SIM-XL analysis. Intra and inter cross-links are depicted as red and blue lines respectively. The inter cross-link arrangement is indicative of a head-to-tail dimeric conformation.

The identified dimeric band was excised, processed, and analyzed by LC-MS/MS. Mass spectra were analyzed with the software SIM-XL[70] using the homodimer analysis feature (Figure 3.1C). Cross-link hits were filtered firstly according to its score. Only those intra and inter cross-links with scores higher that 2 and 3, respectively, were manually inspected. Interestingly, inter cross-link arrangement within the protein map shows closer interactions between distant regions of each monomer (blue lines in Figure 3.1C). This inter cross-link disposition thus seems to be indicative of a head-to-tail dimeric conformation.

Unfortunately, in the four identified inter cross-links, one cross-linked residue lies in a non-resolved region of $Ca_V\beta_2$ three-dimensional structure (PDB 5V2P). Hence, the definition of distance restraints to guide a protein-protein docking is not possible. However, the head-to-tail

dimeric conformation evidence derived from XL-MS is a valuable piece of information that can be used to discriminate between high scored clusters generated in a bioinformatic-driven protein-protein docking (see next section).

3.2.2 $Ca_V\beta_2$ dimeric model

$Ca_V\beta_2$ dimeric interaction was modeled by protein-protein docking in HADDOCK 2.4[71,82] using bioinformatically predicted interfacial residues by CPORT[78], as well as non-crystallographic symmetry restraints and a C2 symmetry restraint. I would like to note here that the two aforementioned symmetry restraints enforce dimer formation, but do not impose any particular conformation, either head-to-head or head-to-tail. The resulting models were clustered using their i-RMSD and ranked according to their HADDOCK score. A total of 392 structures were grouped in nine clusters (Table S3.3).

In order to evaluate the dimeric conformation (e.g. head-to-head or head-to-tail) of the docked structures, the distance between the center of mass (COM) of $Ca_V\beta_2$ SH3 domain of one molecule and the GK domain of its partner was measured in all the structures. Since $Ca_V\beta_2$ has only two domains, a head-to-head conformation would involve interactions between the same domain of each monomer (e.g. SH3/SH3 and GK/GK) and thus a longer SH3-GK distance. On the other hand, a head-to-tail conformation would involve interactions between the SH3 of one monomer and the GK domain of its partner and thus a shorter distance between their center of mass (Figure 3.2A). Besides, the consistency with the XL-MS data with DSS was checked by monitoring the distance between the identified DSS inter cross-linked residues (or the nearest residue for amino acids not present in the structured regions) (see Figure 3.2A).

Interestingly, the structures with a head-to-tail conformation (low COM_{SH3} /COM_{GK} values, i.e. clusters 1, 3, 4, 6, 7 and 8) have a clear tendency to display lower inter cross-link distances compared to those structures with head-to-head conformation (high COM_{SH3} /COM_{GK} values, i.e. clusters 2 and 9) (in Figure 3.2A). This result is in agreement with the MS-derived inter cross-link arrangement in $Ca_V\beta_2$ dimers being compatible with a head-to-tail conformation.

In order to select the cluster more compatible with our experimental information, the dimeric conformation was evaluated for the top scored clusters. Clusters 1 and 2 possess the most favorable HADDOCK scores and their representatives overlap in the HADDOCK score vs i-

RMSD plot (Table S3.3 and Figure S3.2A). Although both clusters represent the best solutions, only cluster 1 displays a head-to-tail dimeric conformation. Interestingly, when inspecting the protein-protein interface of the top four cluster 1 representative structures, the proximity of the C113 residues of each monomer is compatible with the formation of a disulphide bridge between the two monomers, even though these cysteines were modelled as thiol groups. Sulphur-sulphur (S-S) distance (i.e. between 2.05-3 Å), S-H thiol distance (i.e. 1.34 Å) and side chain flexibility were considered to determine a cutoff distance for disulphide bridging of 4.68 Å. Miranda-Laferte et al. (2011)[31] demonstrated the importance of C113 disulphide bridge for homodimerization of $Ca_v\beta_2$ SH3 domains through site-directed mutagenesis and cellular assays. The possibility of forming this disulphide bridge seems to be a characteristic of most of head-to-tail clusters since they all show lower C113/C113' sulphur-sulphur distances compared to head-to-head clusters (Figure S3.2C). In essence, the favourable HADDOCK score, together with the agreement with the experimental data (both MS spectra recorded here and previous mutagenesis studies) indicate that cluster 1 is the most likely model of $Ca_v\beta_2$ homodimer.

The cluster 1 structures were further analysed by calculating the contact frequency of $Ca_v\beta_2$ residues at the interface between both monomers. Such analysis highlights a patch distributed along one $Ca_v\beta_2$ face that includes both GK and SH3 domains (Figure S3.2B). This is in line with C113 mutation being able to abolish dimerization in isolated SH3 domains, but not in the full-length (SH3+GK) protein. In the head-to-tail homodimer model, most of the protein-protein contacts are established between SH3 and GK of the different partner molecules (Figure 3.2B). However, a discrete, smaller interacting region between both SH3 domains of the partners is also observed which is mostly governed by a disulphide bridge between the C113 and C113'.

It is also noticeable the role of the SH3 domain α_2 helix in mediating the interaction with the GK domain in the dimeric complex. Interestingly, an extension of the α_2 helix, the so-called HOOK, would clearly occlude the α_1 interaction domain (AID) binding site in $Ca_v\beta_2$ dimers (Figure S3.2C). Although the end of this helix and the HOOK are not resolved in $Ca_v\beta_2$ three-dimensional structure, this model already anticipates a steric clash between the $Ca_v\beta_2$ HOOK loop and the $Ca_v\alpha_1$ AID. The overlap between the interaction surfaces evidences that $Ca_v\beta_2$ interaction with itself and $Ca_v\alpha_1$ are mutually exclusive. The incompatibility of $Ca_v\beta$ dimerization and $Ca_v\beta/Ca_v\alpha_1$ interaction suggested by the homodimer structural model obtained

here is in line with FRET experiments indicating that the presence of $Ca_v\alpha_1$ AID impairs $Ca_v\beta_2$ dimerization[31].

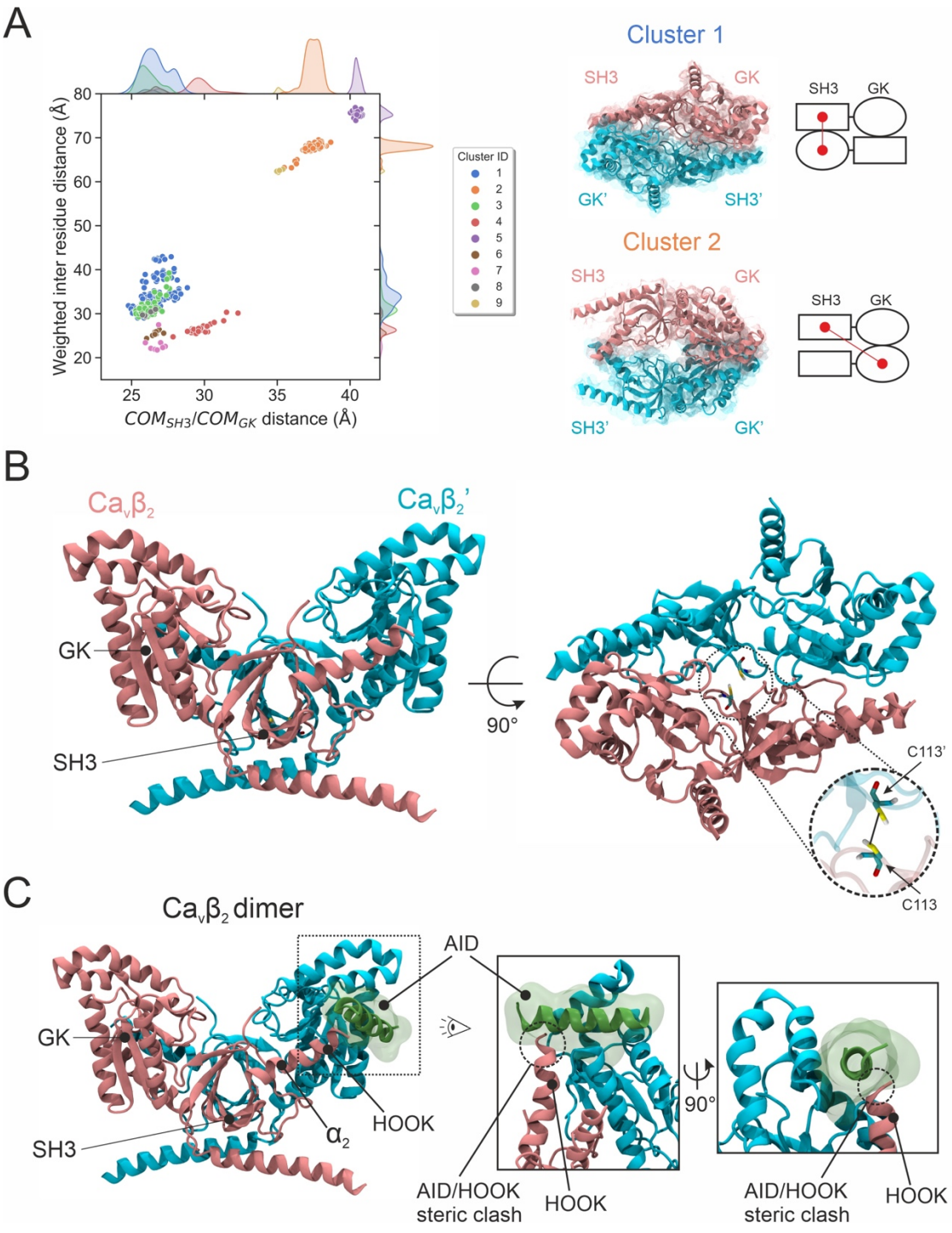

Figure 3.2. Protein-protein docking of $Ca_v\beta_2$ dimers in HADDOCK 2.4. A) Weighted inter residue versus COM_{SH3}/COM_{GK} distances plot. Both distances were measured for all the structures of the HADDOCK homodimer docking. Each point represents a HADDOCK solution structure,

which is coloured according to the HADDOCK cluster ID (left panel). Two representative structures belonging to the top four of the best HADDOCK scored clusters (i.e., cluster 1 and 2) are represented in a cartoon and surface model in cyan and pink colours for each monomer. COM_{SH3}/COM_{GK} distances are indicated as a red line on a schematised representation of both homodimers (right panel). **B)** Representative cluster 1 $Ca_V\beta_2$ dimer model highlighting the C113 disulphide bridge that was previously described in reference [31]; the same colour code as in panel (A) was used for the two monomers ($Ca_V\beta_2$ numbering according to UniProtKB Q8VGC3-2). **C)** $Ca_v\alpha_1$ AID helix (from PDB code 5V2P) was structurally superimposed on $Ca_V\beta_2$ dimeric model using a $Ca_V\beta_2$ model as template. AID is represented in a cartoon and surface green model. AID superimposition on $Ca_V\beta_2$ dimeric model anticipates a HOOK/AID steric clash.

3.2.3 Identification and validation of hotspots residues at the dimeric interface

A computational alanine scanning (CAS) involving seven predictors (Anchor, Robetta, BUDE, BeAtMuSiC, Mutabind2, SAAMBE-3D and mCSM-PPI2)[88–94] was performed to identify the residues at the $Ca_v\beta_2$ dimeric interface contributing the most to the binding energy of the protein-protein complex, the so-called hotspots (see sections 2.4 and 2.6.11). The top four scored HADDOCK structures in cluster 1 (see section 3.2.2) compatible with the formation of the C113/C113' disulphide bridge (i.e., sulphur-sulphur distance lower than 4.68 Å) were selected for CAS analysis. The change in ΔΔG upon alanine mutation was computed for each of the aforementioned predictors over these four structures to get a consensus prediction that accounted for both the protein flexibility and the different (physics- or machine learning-based) nature of each predictor (Figure S3.3). Such consensus prediction revealed several hotspots candidates at the dimeric interface that were subsequently manually inspected to evaluate if the effect of a possible alanine mutation could be counteracted by a neighboring residue (Table S3.4). As a result, a set of six residues was selected for experimental alanine mutation (C113, H131, R134, D388, D394 and Y402).

These six residues are distributed in three different patches at $Ca_v\beta_2$ dimeric interface (Figure 3.3A). H131, R134, D388 and D394 are located at the GK/SH3 α_2 interface and establish two salt bridges across the monomer-monomer interface (R134-D388' and H131-D394' and vice versa). C113 forms a unique disulphide bridge located in the narrow SH3/SH3 interface, as previously suggested by *in vitro* and *in cellulo* experiments[31]. Finally, Y402 can form a

hydrogen bond or cation-pi interaction, depending on the side chain orientation, with R69 and is located at the GK/SH3 dimeric interface.

Site-directed mutagenesis was performed to introduce these six substitutions to alanine in the $Ca_v\beta_2$-core (see section 2.6.12). The $Ca_v\beta_2$-core protein bearing these six point mutations (hereinafter $Ca_v\beta_2$-core 6A) was expressed in *E. coli* and purified through Ni-NTA affinity and size-exclusion chromatography (SEC; see section 2.6.13). Analytical SEC profiles of $Ca_v\beta_2$-core 6A show that it elutes as a monodisperse peak with no signs of aggregation (Figure S3.4A). To further investigate whether the six-point mutations affect the stability of $Ca_v\beta_2$-core 6A, GST-AID based pull-down assays and intrinsic tryptophan fluorescence measurements were carried out (see sections 2.6.14 and 2.6.15, respectively).

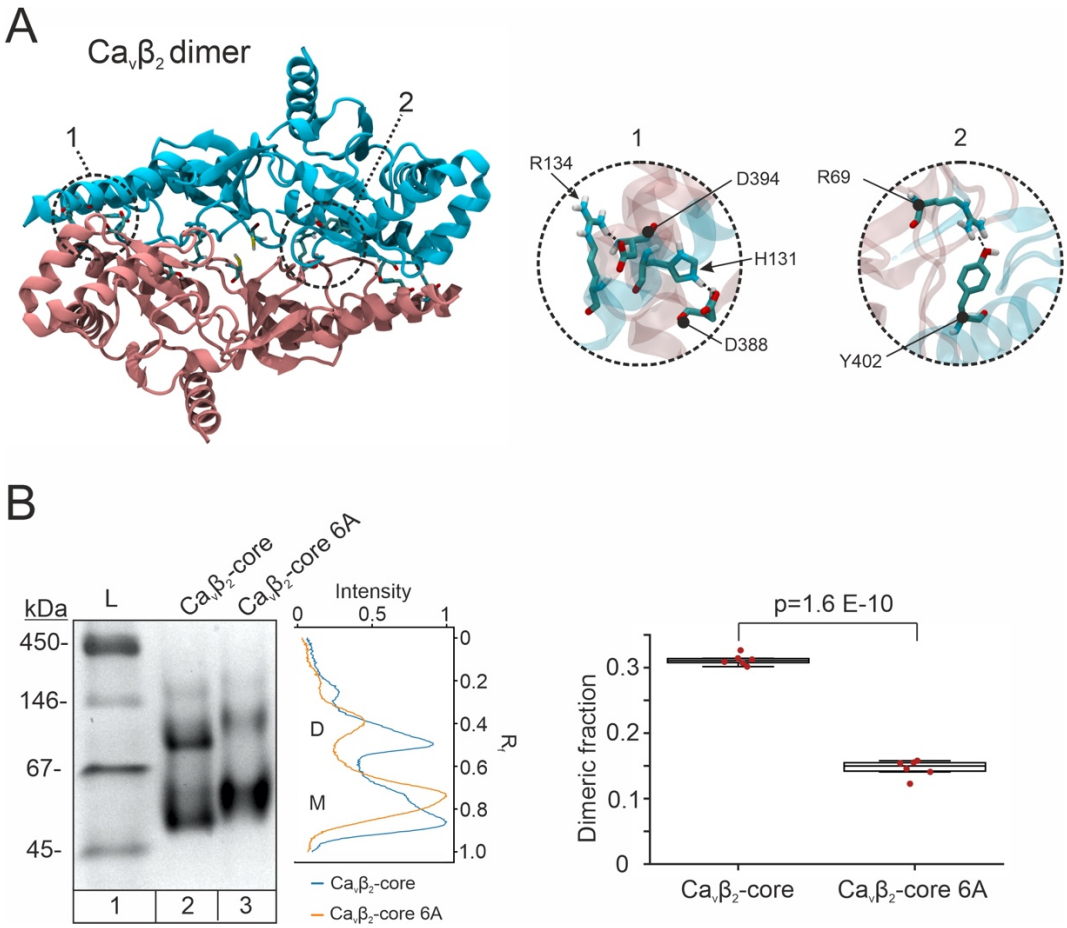

Figure 3.3. Computational alanine scanning (CAS) identifies hotspots at the $Ca_v\beta_2$ dimeric interface. A) Top view of $Ca_v\beta_2$ dimeric model. CAS resulted in the identification of several key residues at the dimeric interface that are shown in zoom captions on the right part of the panel. Residues are represented in a stick model. ($Ca_V\beta_2$ numbering according to UniProtKB Q8VGC3-

2). **B)** Left panel: BN-PAGE of a $Ca_v\beta_2$-core wild-type protein and bearing the six hotspot candidate point mutations ($Ca_v\beta_2$-core 6A, i.e. C113/H131/R134/D388/D394/Y402) and densitometry plots for the corresponding gel. M: monomer; D: dimer. Right panel: densitometric analysis shows a decrease in dimeric fraction for the $Ca_v\beta_2$-core 6A mutant compared to WT. Significance calculated with a Student t test (n=6).

Pull down assays were designed using the AID coupled to a GST fusion protein as bait. GST alone was used as a negative control. $Ca_v\beta_2$-core WT and $Ca_v\beta_2$-core 6A coelute with GST-AID but are not present in the GST control (Figure S3.4C). Such results demonstrate that $Ca_v\beta_2$-core 6A preserve its ability to bind AID and thus that its stability remains unaltered.

Furthermore, the intrinsic fluorescence of $Ca_v\beta_2$-core WT and $Ca_v\beta_2$-core 6A over a range of temperatures from 20 ºC to 75 ºC was also studied (Figure S3.4B). $Ca_v\beta_2$-core WT unfolded following a two-state transition with a T_m of 46.08 ± 0.27 ºC, comparable with the previous measurements shown in section 3.1 and previous studies[104]. In contrast, $Ca_v\beta_2$-core 6A unfolded following a three-state transition with a T_{m1} of 34.88 ± 1.54 ºC and a T_{m2} of 55.46 ± 0.8 ºC. Although, the overall stability does not seem to be affected upon 6Ala mutation, a decoupling of two kinetic events during $Ca_v\beta_2$-core 6A unfolding occurs, which might correspond to the denaturation of the dimeric and monomeric populations (T_{m1} and T_{m2}, respectively)[105]. These results indicate that $Ca_v\beta_2$-core homodimerization equilibrium is altered upon 6Ala mutation.

In order to study changes in the $Ca_v\beta_2$-core 6A dimerization pattern, BN-PAGE was used. $Ca_v\beta_2$-core WT and $Ca_v\beta_2$-core 6A samples were separated in a native gradient gel and scanned to perform a densitometric analysis of the resulting bands (Figure 3.3B). $Ca_v\beta_2$-core WT displays a double migration pattern compatible with a monomeric and dimeric band and comparable intensities by eye inspection. On the other hand, although $Ca_v\beta_2$-core 6A pattern also presents two bands, the dimeric band is drastically reduced. Both $Ca_v\beta_2$-core WT and $Ca_v\beta_2$-core 6A dimeric fractions were calculated as the ratio of the dimeric band adjusted intensity over the total intensity (i.e., monomeric plus dimeric band intensities). $Ca_v\beta_2$-core 6A dimeric fraction is significantly reduced when compared to its WT counterpart ($p = 1.6\ 10^{-10}$ in a Student t test). Such decrease further proves that the mutated residues, predicted to be hotspots located at the $Ca_v\beta_2$ dimeric interface contribute to the monomer-monomer interaction, thus providing an *in vitro* validation of the proposed $Ca_v\beta_2$ dimerization model.

During the writing of this thesis, the hotspots mutations were incorporated in the background of a $Ca_V\beta_2$ full length containing the N- and C-terminal fragments that $Ca_V\beta_2$-core is lacking. The dimerization pattern, also assessed by BN-PAGE, did not differ between $Ca_V\beta_2$ WT and $Ca_V\beta_2$ 6A full length proteins. We hypothesize that the variable segments contribute to the dimerization by partially compensating the substitution of the hotspot residues in the mutant protein. Further experiments are needed to elucidate the contribution of the N and C termini to $Ca_V\beta$ dimerization.

3.2.4 $Ca_V\beta_2$ dimerization supplemental data

3.2.4.1 Supplemental figures

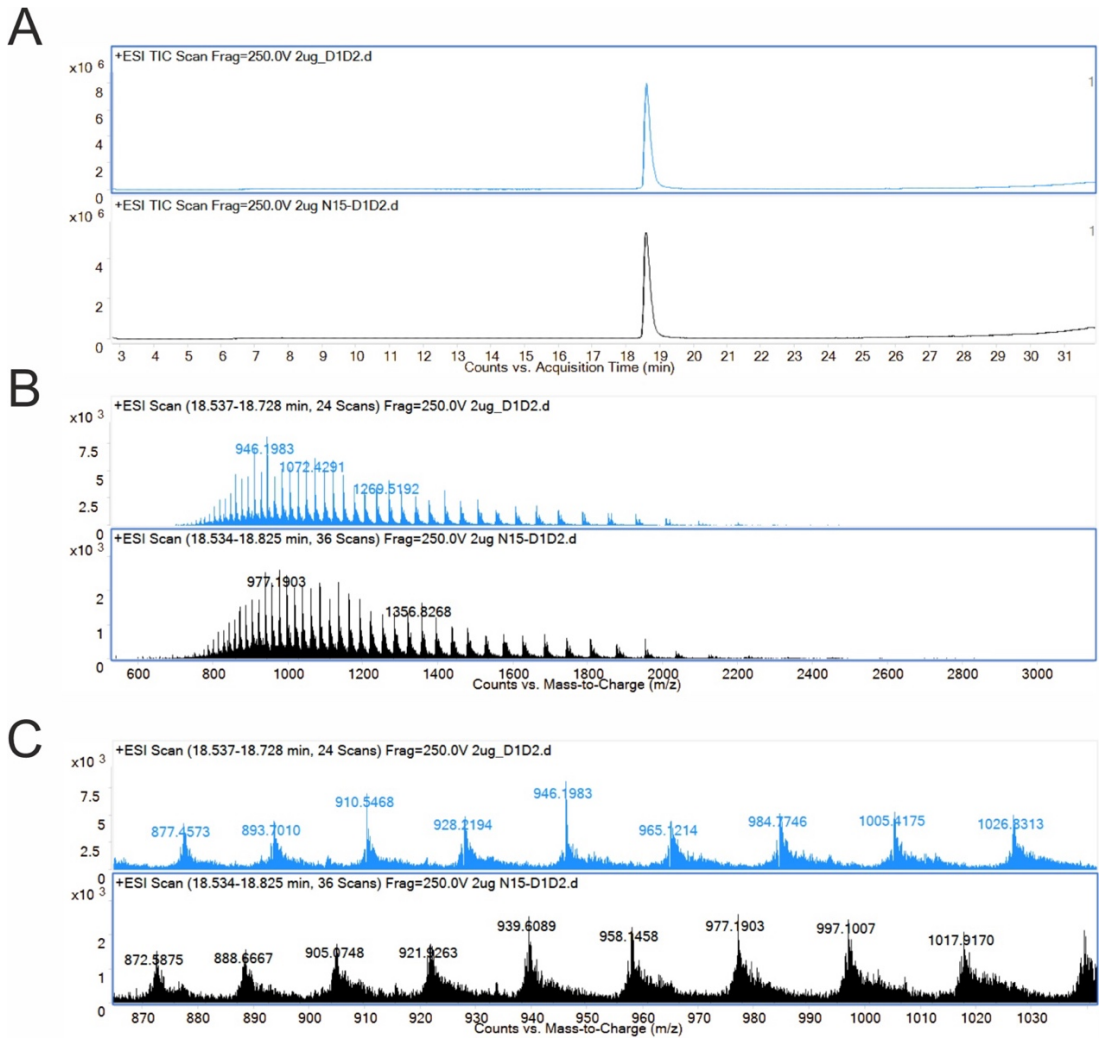

Figure S3.1. ^{14}N-$Ca_V\beta_2$-core and ^{15}N-$Ca_V\beta_2$-core molecular weight (MW) determination. A) Elution profile of ^{14}N-$Ca_V\beta_2$-core (top, blue) and ^{15}N-$Ca_V\beta_2$-core (bottom, black) after reverse

chromatography. **B)** ESI mass spectra of ^{14}N-Ca$_V\beta_2$-core (top, blue) and ^{15}N-Ca$_V\beta_2$-core (bottom, black). **C)** Subrange of the mass spectra used for molecular weight determination; ^{14}N-Ca$_V\beta_2$-core (top, blue) and ^{15}N-Ca$_V\beta_2$-core (bottom, black).

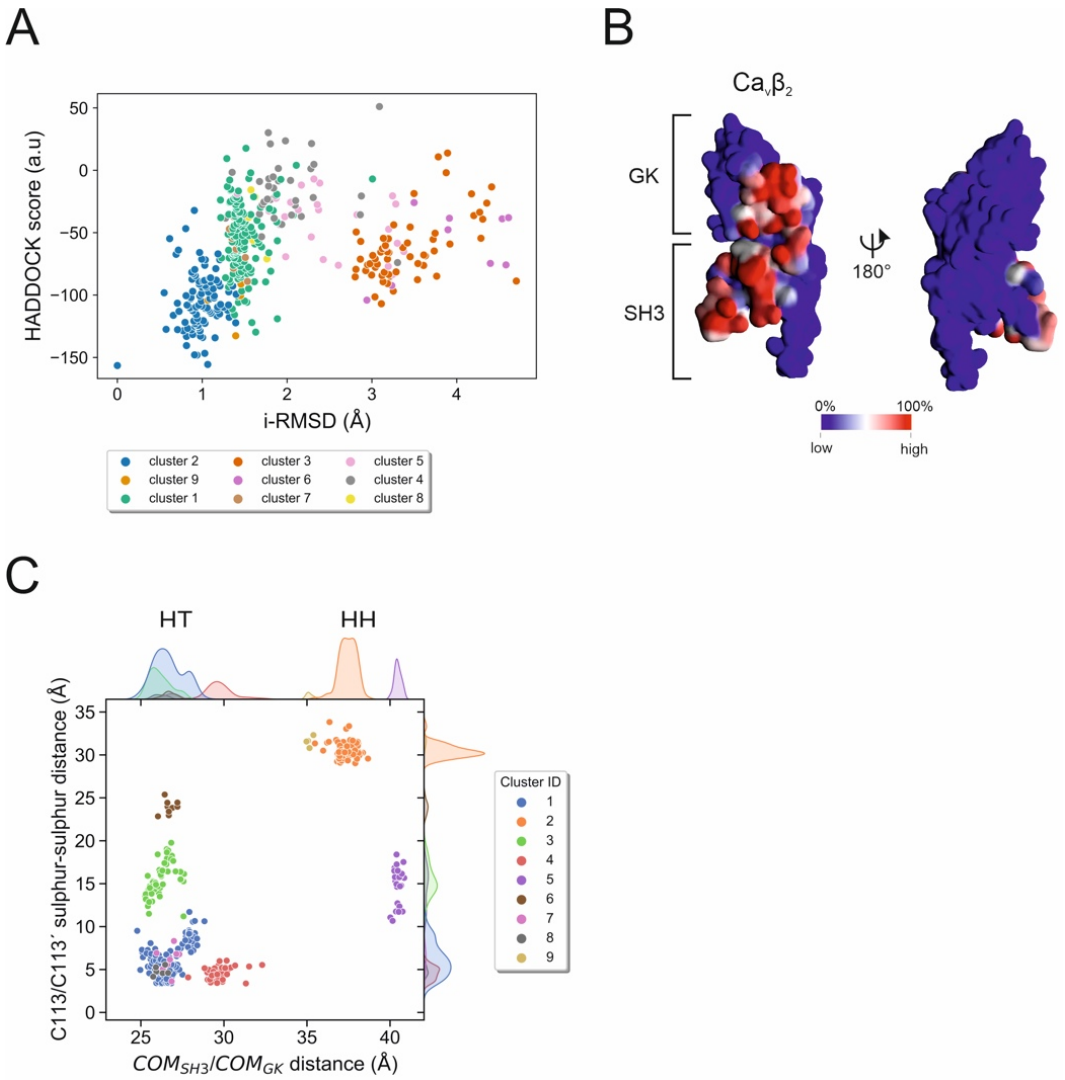

Figure S3.2. Ca$_v\beta$2 dimeric interface. A) HADDOCK score versus i-RMSD plot from Ca$_v\beta_2$ dimers docking. **B)** Surface model of Ca$_v\beta_2$ (based on PDB code 5V2P) showing the contact frequency of each residue in the 134 docked structures belonging to cluster 1. High-to-low contact frequency is indicated with red-to-blue colours. **C)** C113/C113' sulphur-sulphur distance versus inter domain center of mass distance.

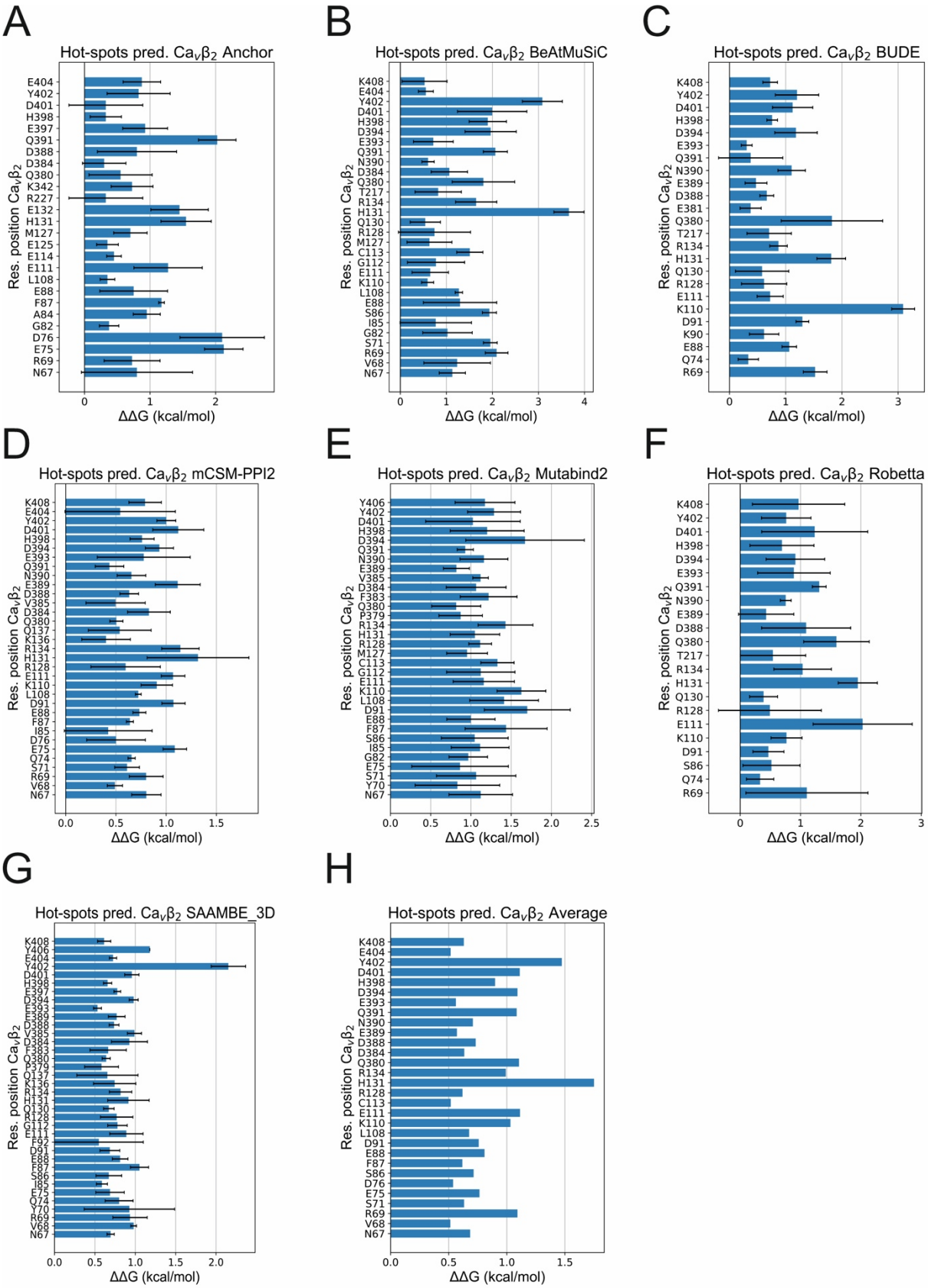

Figure S3.3. Computational alanine scanning of $Ca_v\beta_2$ dimeric interface. Change in protein-protein binding free energy (ΔΔG) predicted by Anchor (**A**), BeAtMuSiC (**B**), BUDE (**C**),

mCSM-PPI2 (**D**), Mutabind2 (**E**), Robetta (**F**) and SAAMBE-3D (**G**). Values were averaged over the top four HADDOCK scored structures of cluster 1 whose C113/C113' sulphur/sulphur distance allowed the formation of the disulphide bridge (see section 3.2.3). The consensus prediction averaged over all seven predictors is displayed in (**H**). Only mutations resulting in a ΔΔG higher than 0.3 kcal/mol are shown. ($Ca_V\beta_2$ numbering according to UniProtKB Q8VGC3-2).

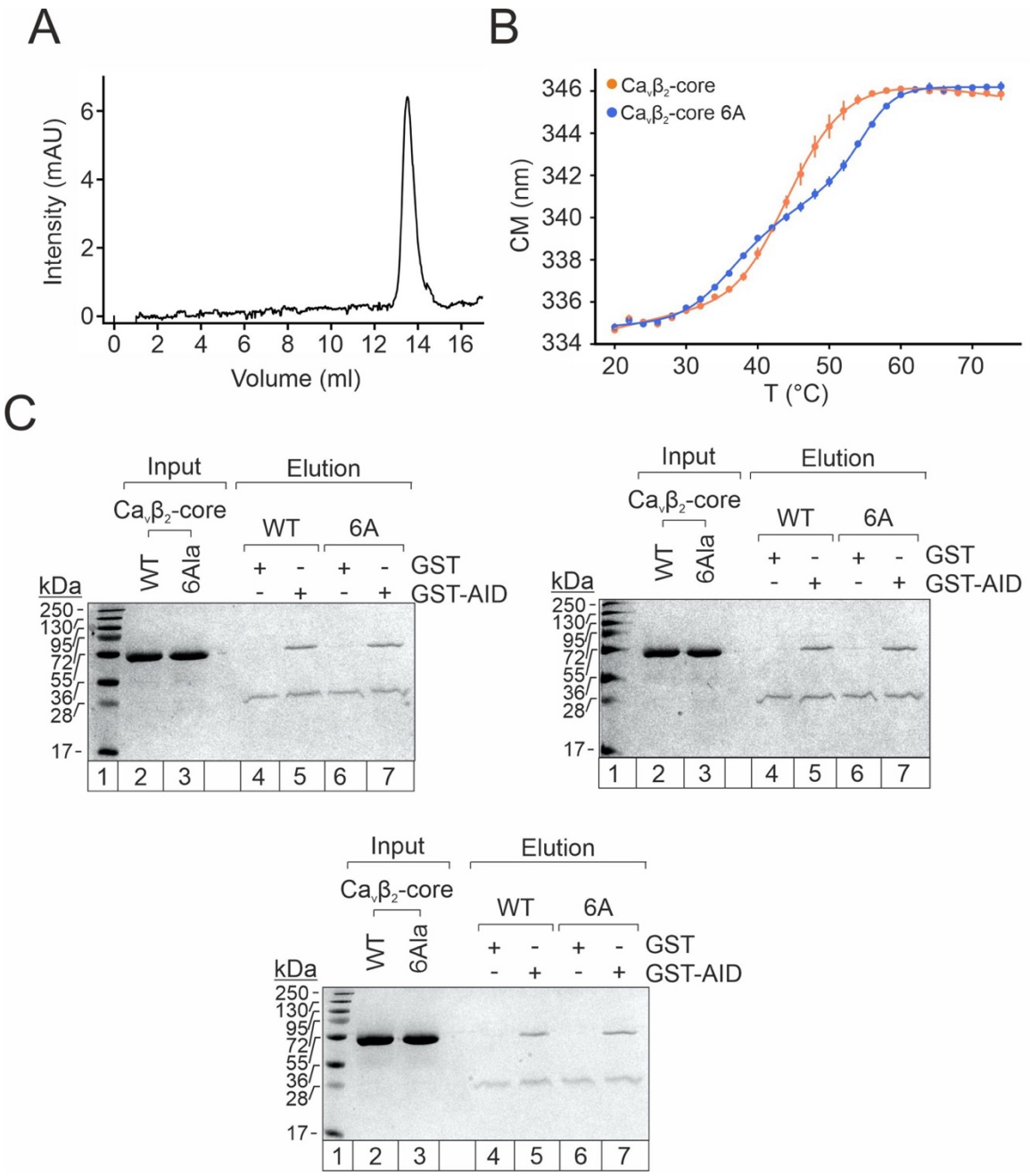

Figure S3.4. Functional characterisation of $Ca_v\beta_2$-core 6A. A) Size-exclusion chromatography profile of $Ca_V\beta_2$-core 6A in GF-300 buffer containing; 20 mM Sodium phosphate, 300 mM NaCl, pH 8.0. **B)** Thermal unfolding curves for $Ca_v\beta_2$-core (orange) and $Ca_v\beta_2$-core 6A (blue). Each point corresponds to the average of three independent measurements. **C)** SDS-PAGE gels of GST-AID pull down assays for $Ca_v\beta_2$-core and $Ca_v\beta_2$-core 6A.

3.2.4.2 Supplemental Tables

Table S3.1. Molecular weight estimation with ESIprot for ^{14}N-Ca$_V\beta_2$-core.

m/z	charge	MW [Da]	Error [Da]
910.54	53+	48,205.228254735	-2.3384785502494
928.21	52+	48,214.535646155	6.9689128698519
946.19	51+	48,204.313037575	-3.2536957100456
965.12	50+	48,205.630428995	-1.9363042899495
984.77	49+	48,204.367820415	-3.1989128698551
1005.41	48+	48,211.325211835	3.7584785502549

Deconvoluted MW [Da]	48,207.5667
Standard deviation [Da]	4.3064

Table S3.2. Molecular weight estimation with ESIprot for ^{15}N-Ca$_V\beta_2$-core.

m/z	charge	MW [Da]	Error [Da]
921.92	53+	48,808.368254735	-1.2884785502611
939.6	52+	48,806.815646155	-2.841087130153
958.14	51+	48,813.763037575	4.1063042899405
977.19	50+	48,809.130428995	-0.52630428996054
997.1	49+	48,808.537820415	-1.1189128698607
1017.91	48+	48,811.325211835	1.6684785502439

Deconvoluted MW [Da]	48,809.6567
Standard deviation [Da]	2.4862

Table S3.3. Statistics for the $Ca_v\beta_2$ dimerization docking data. Results for the $Ca_v\beta_2$ protein-protein docking performed with HADDOCK 2.4. Clusters are ranked by the average HADDOCK score of the top four structures.

	1	2	3	4	5	6	7	8	9
HADDOCK score (a.u)	-121.7 ± 5.2	-152.1 ± 4.0	-99.1 ± 5.9	-52.3 ± 13.6	-77.1 ± 4.3	-86.8 ± 12.2	-75.2 ± 9.7	-47.0 ± 18.1	-107.2 ± 15.5
Cluster size	134	104	58	35	25	9	8	6	4
RMSD from the overall lowest-energy structure (Å)	28.2 ± 1.7	0.8 ± 0.5	31.3 ± 0.1	27.1 ± 0.8	10.6 ± 1.0	27.4 ± 0.2	30.0 ± 0.3	30.3 ± 0.0	5.4 ± 0.1
Van der Waals energy (kcal mol^{-1})	-93.2 ± 26.7	-90.9 ± 5.7	-85.8 ± 15.2	-77.8 ± 8.8	-82.2 ± 14.0	-90.9 ± 14.2	-102.2 ± 16.6	-82.8 ± 18.1	-89.5 ± 8.2
Electrostatic energy (kcal mol^{-1})	-656.8 ± 184.5	-813.2 ± 94.9	-591.5 ± 72.8	-446.6 ± 100.1	-562.5 ± 32.2	-605.7 ± 57.8	-380.4 ± 90.2	-393.9 ± 69.9	-570.3 ± 54.5
Desolvation energy (kcal mol^{-1})	25.3 ± 16.8	23.3 ± 4.5	16.9 ± 8.5	36.3 ± 7.7	27.5 ± 6.0	20.7 ± 5.6	14.7 ± 10.8	14.1 ± 8.7	23.4 ± 4.7
Restraints violation energy (kcal mol^{-1})	771.8 ± 66.2	778.6 ± 97.2	878.3 ± 40.4	781.7 ± 102.3	898.2 ± 62.0	1042.4 ± 91.9	880.5 ± 26.6	999.2 ± 90.4	726.1 ± 67.8
Buried Surface Area (Å)	3783.7 ± 112.6	3708.6 ± 130.3	3526.5 ± 242.0	3147.1 ± 172.0	3556.3 ± 329.6	3872.3 ± 107.7	3723.4 ± 119.9	3259.5 ± 325.0	3539.8 ± 106.2
Z-Score	-1.0	-1.9	-0.3	1.2	0.4	0.1	0.5	1.4	-0.5

Table S3.4. Top residues identified by CAS. Only those residues whose ΔΔG is higher than 1 kcal mol^{-1} are shown. Partner residues of the previous group that were mutated have been incorporated as well.

Residue	ΔΔG (kcal mol^{-1})	Partner residue	Interaction type
H131	1.75	D388	salt bridge
Y402	1.47	R69	cation-pi / hydrogen bond
E111	1.11	S266	hydrogen bond
D401	1.11	Q74/E75	hydrogen bond
Q380	1.1	P218	hydrogen bond
D394	1.09	R134	salt bridge
R69	1.09	Y402	cation-pi
Q391	1.09	R131	hydrophobic/hydrogen bond/pi-pi stacking
K110	1.03	D91	salt bridge
R134	0.99	D394	salt bridge
D388	0.73	H182	salt bridge
C113	0.52	C113	disulphide bridge

Table S3.5. Parameters obtained for the $Ca_v\beta_2$-core unfolding curve after fitting to a two-state transition. (Equation 2.5 in section 2.6.15). Note that temperatures values are shown in Celsius (ºC).

	Value	Standard dev.
A_n	333.09562	0.27762
B_n	0.08162	0.01043
A_d	350.4979	0.89893
B_d	-0.06299	0.01258
DT	16.81601	0.91202
T_m	46.08503	0.27384

Table S3.6. Overall statistics for $Ca_v\beta_2$-core two-state transition unfolding curve fitting.

Parameter	Value
Number of Points	28
Degrees of Freedom	22
Reduced Chi-Sqr	0.01439
Residual Sum of Squares	0.31668

R-Square (COD)	0.99947
Adj. R-Square	0.99935
Fit Status	Succeeded(100)

Table S3.7. Parameters obtained for the $Ca_V\beta_2$-core 6A unfolding curve after fitting to a three-state transition. (Equation 2.6 in section 2.6.15). Note that temperatures values are shown in Kelvin (K).

	Value	Standard dev.
A_n	328.27269	9.68055
B_n	0.02249	0.03294
A_d	346.90011	4.13749
B_d	-0.00208	0.01205
A_i	288.17528	26.73336
B_i	0.16453	0.0833
T_{m1}	308.03692	1.54277
T_{m2}	328.61624	0.78956
DT1	13.46257	2.75158
DT2	9.46718	1.56738

Table S3.8. Overall statistics for $Ca_V\beta_2$-core 6A three-state transition unfolding curve fitting.

Parameter	Value
Number of Points	28
Degrees of Freedom	18
Reduced Chi-Sqr	0.00672
Residual Sum of Squares	0.12098
R-Square (COD)	0.99977
Adj. R-Square	0.99965
Fit Status	Succeeded(100)

Chapter 4. Discussion

4.1 Interaction of $Ca_V\beta$ and actin supports the clearance of functionally defective $Ca_V1.2$ channels

$Ca_v\beta$/F-actin interaction appeared to be functionally relevant in different cellular contexts with varied outcomes. However, the lack of structural data on the $Ca_v\beta$/F-actin complex only allowed for a comprehension of its cellular function by applying pharmacological treatments that involved the disruption of the actin cytoskeleton. Here, XL-MS and protein-protein docking were used to generate a $Ca_v\beta$/F-actin model, derive structural and functional information and specifically target this interaction.

The results presented in this thesis have shown that both $Ca_v\beta_2$ and $Ca_v\beta_4$ present homologous binding interfaces on actin, a characteristic that can be extended to all $Ca_v\beta$s due to its high sequence and structural conservation. Moreover, $Ca_v\beta$/F-actin model illustrates how $Ca_v\beta$ binds on a region between actin subdomains (SD) 1 and 3 of one monomer and SD2 and SD1 of the neighbouring monomer. Two interesting aspects emerge from the description of this protein interaction region:

First, other actin binding proteins have been found to bind to the same interface, such as Myosin, Myosin binding protein C[106] or Utrophin[107]. Hence, a significant competition for actin binding may arise that restricts $Ca_v\beta$/F-actin interaction to certain molecular contexts. Second, such interfaces and that of $Ca_v\beta$ are characterised for encompassing the actin Dnase (D)-loop region. The D-loop is a loop located at SD2 that has been extensively studied because of undergoing significant conformational transitions[108–111]. Actin binding proteins are believed to sense actin overall conformation through changes in the D-loop[111]. Therefore, it is tentative to suggest that $Ca_v\beta$ GK domain, located in the proximity of the D-loop in the model of the $Ca_v\beta$/F-actin complex, could sense different actin conformations and that way modulate $Ca_v\beta$/F-actin interaction.

CAS together with site-directed mutagenesis were applied to experimentally validate the $Ca_v\beta$/F-actin model I obtained in this thesis. The introduction of eight-point mutations in two

different $Ca_v\beta$ protein backgrounds, a $Ca_v\beta_2$-core and a longer $Ca_v\beta_4$ with a C terminal deletion ($Ca_v\beta_4$ R482X), has shown a clear decreased affinity of $Ca_v\beta$s mutants for F-actin, thus validating the XL-MS derived docking model. This rationally designed mutant ($Ca_v\beta$ 8Ala) was used to study the outcomes of $Ca_v\beta$/F-actin interaction disruption in HEK cells by electrophysiological measurements. Interestingly, whole cell currents from cells coexpressing $Ca_V1.2$ L-type subunit and $Ca_v\beta_2$ 8Ala showed a significantly decreased ionic current magnitude compared to those of $Ca_v\beta_2$ WT. The study of PPI in such heterologous system may pose some limitations coming from its non-native expression environment. Even though, the HEK expression system was a valuable tool to obtain initial data, further experiments should be carried out in cardiomyocytes or neurons to determine the contribution of the $Ca_v\beta$/F-actin interaction in a native environment.

In order to discern which parameter of the function describing the magnitude of the macroscopic ionic current was responsible for this decrease, the total number of calcium channels was determined by recording $Ca_v1.2$ gating currents. Gating currents were not significant decreased upon co-transfection with $Ca_v\beta_2$ 8Ala, indicating that the total number of calcium channels at the cellular membrane remained unaltered. To further discern the contribution of other parameters (number of conductive channels, open probability and unitary conductance) to the macroscopic ionic current, a stationary noise analysis was performed. This analysis showed that, whereas the channel open probability and unitary conductance of the remaining channels did not vary, the number of conductive calcium channels was significantly decreased.

The combination in this study of gating currents recordings and stationary noise analysis constitutes an innovative methodological approach to discriminate between conductive and total number of channels present at the cellular membrane. The observed differences in the estimations of the number of channels can be explained by the presence of non-conductive calcium channels in the cellular membrane that indeed contribute to the overall gating currents recordings but do not conduct calcium. These results point out a direct implication of $Ca_v\beta$/F-actin interaction in the regulation of calcium channel quality control at the cell surface.

In essence, this strategy allowed us to define a new function of the $Ca_v\beta$/F-actin interaction in supporting the clearance of functionally defective channels. To my knowledge, a direct implication of $Ca_v\beta$/F-actin interaction in the regulation of calcium channels quality control at the cell surface has not yet been considered. Dysregulation of this process can be associated

with the accumulation of defective channels, a consequent damage to the cell membrane integrity and altered proteostasis. Finally, such cellular changes can manifest in altered physiological states like cardiac affections, neurological dysfunctions and cancer[112,113].

This section contains a discussion about selected topics of $Ca_v\beta$/F-actin interaction, for discussion on other points check section 3.1.

4.2 Molecular basis of $Ca_v\beta$ dimerization

$Ca_v\beta$ oligomerization was firstly described by Lao et al. (2010)[53]. Since that study, several followed-up works further contributed to the understanding of $Ca_v\beta$ dimerization, see references [17,30,31,54]. The mentioned studies, although significant, lacked a molecular model that completed our understanding of the structure and function of $Ca_v\beta$ dimerization.

In order to derive relevant structural information of $Ca_v\beta_2$ dimers by XL-MS, a protocol that involved the stable isotope labelling of $Ca_v\beta_2$ with ^{15}N was applied[103]. This protocol was also successfully used for other proteins such as apolipoprotein A-IV[114], Guanylyl Cyclase [115] or GCAP-2[116].

The discrimination between intra and inter cross-links pointed out a head-to-tail overall $Ca_v\beta_2$ dimeric conformation. In this conformation, interactions between the SH3 domain of one chain and the GK domain of its partner are formed. Interestingly, another member of the MAGUK family, the MPP5-PSG protein, was shown to dimerize following a head-to-tail conformation[55]. In this conformation, the MPP5-PSG SH3 and GK domains encompass all the interactions contributing to the dimeric interface but the PDZ domain, a third domain present in other MAGUKs but missing in $Ca_v\beta$s, is excluded from the dimeric interaction. This fact explains why $Ca_v\beta$s, despite missing the PDZ domain, have maintained its dimerization ability.

$Ca_v\beta_2$ dimeric interaction was then modeled by protein-protein docking using the HADDOCK 2.4 webserver[71,82]. Among the top HADDOCK scored clusters, cluster 1, which presents a head-to-tail conformation and is compatible with XL-MS data was chosen for further experimental validation (Figure 3.2B). $Ca_v\beta_2$ dimeric model has three main inter domain interfaces, namely two SH3/GK interfaces and one SH3/SH3 interface. Interestingly, the SH3/SH3 interaction interface is mostly governed by a disulphide bride between cysteines 113 of each monomer, as

anticipated by Miranda-Laferte et al. (2011)[31] in a study on $Ca_v\beta$ SH3 domains. On the other hand, the presence of two SH3/GK interfaces agrees with results by Page et al. (2010)[54], showing that $Ca_v\beta$ SH3 and GK domains can interact in yeast two hybrid assays. Moreover, the extensive contacts between SH3 and GK domains of adjacent monomers explains why the mutation C113A, introduced to avoid the formation of the disulphide bridge between SH3 domains, did not completely disrupt $Ca_v\beta$ full length dimerization as shown in Miranda-Laferte et al. (2011)[31].

The $Ca_v\beta_2$ dimeric model created in this thesis shows that the SH3 α_2 helix contributed to the interaction with the GK domain. An extension of the α_2 helix, the so-called HOOK, is shown to occlude the AID binding site in $Ca_v\beta_2$ dimers, thus excluding the simultaneous interaction of $Ca_v\beta_2$ with another $Ca_v\beta_2$ subunit and $Ca_v\alpha_1$ (Figure 3.2C). Such structural observation might explain why $Ca_v\beta$ binding with the AID peptide prevents $Ca_v\beta$ dimerization as shown in FRET experiments[31].

In order to validate the homodimer model and design mutants with a decreased $Ca_v\beta$ dimerization ability, CAS followed by rational site-directed mutagenesis was performed. Hotspots residues were identified by CAS and located on three major patches on $Ca_v\beta_2$ dimeric interface (Figure 3.3A). Such mutations (H131A, R134A, D388A, D394A and Y402A), together with the C113A mutation, were introduced by site-directed mutagenesis in $Ca_v\beta_2$-core. $Ca_v\beta_2$-core 6A stability was proved by analytical SEC, thermal unfolding and GST-AID based pull-down assays (Figure S3.4). Interestingly, a change in the unfolding transition mode from two-state ($Ca_v\beta_2$-core WT) to three-state for $Ca_v\beta_2$-core 6A was detected. A weakening of the $Ca_v\beta_2$-core dimeric interface upon Ala mutation might result in the decoupling of two kinetic events during $Ca_v\beta_2$-core unfolding, possibly corresponding to the denaturation of dimeric and monomeric populations, respectively, as shown for other dimeric proteins[105].

$Ca_v\beta_2$-core WT and $Ca_v\beta_2$-core 6A dimerization patterns were studied by BN-PAGE and the dimeric fraction estimated with densitometric analysis (Figure 3.3B). $Ca_v\beta_2$-core 6A showed a significantly decreased dimeric fraction, further supporting that the six mutated residues are indeed responsible for relevant interactions at the $Ca_v\beta_2$ dimeric interface. These *in vitro* results constitute an experimental validation of the $Ca_v\beta_2$ dimeric model proposed in this thesis and set the basis for future studies on $Ca_v\beta$ dimerization roles in the cellular context. Moreover, *in*

cellulo studies will be needed to study $Ca_v\beta$ dimerization and its relationship with dynamin binding, where the hotspots identified here are expected to have a crucial role.

4.3 $Ca_V\beta$-actin interaction and $Ca_V\beta$ dimerization: two interactions regulating voltage-gated calcium channels availability at the cellular membrane.

$Ca_v\beta$ is a multiregulatory protein that can interact with a plethora of partners[33]. In this thesis, $Ca_v\beta$/F-actin interaction and $Ca_v\beta$ dimerization have been studied and the interaction interfaces described (Figure 4.1A). Notably, these two interactions involve clearly defined different $Ca_v\beta$ interfaces. This evidence suggests that mutations within one interface should not affect the corresponding function of the other and vice versa. Recent experimental data collected during the writing of this thesis support this hypothesis. These findings reveal that the actin binding deficient mutant ($Ca_v\beta_2$ 8Ala) retains its dimerization ability assessed by BN-PAGE.

Structural alignments of the protein-protein complex models obtained in this thesis evidence steric clashes incompatible with simultaneous interactions of $Ca_v\beta$ with F-actin and another $Ca_v\beta$ subunit (Figure 4.1B). This observation indicates that $Ca_v\beta$/F-actin interaction and $Ca_v\beta$ dimerization are structurally exclusive interactions. Although rigid-body complexes structures have been used for this structural alignment, a conformational change in the $Ca_v\beta$ dimeric complex that could enable actin binding and justify a simultaneous interaction is not plausible.

$Ca_v\beta$ was shown to form a tripartite interaction with calcium channels and F-actin[50]. Structural data generated in this thesis further supports on the possibility of forming such triple interaction, as the F-actin binding interface of $Ca_v\beta$, does not overlap the AID binding pocket. On the other hand, the results shown in this thesis indicate that $Ca_v\beta$ dimerization and $Ca_v\beta$ binding to calcium channels seem to be exclusive processes, as the HOOK region of $Ca_v\beta$ and the AID would incur in a steric clash if $Ca_v\beta$ dimerized and bound AID at the same time. It is interesting to highlight that, according to these observations, monomeric $Ca_v\beta$ can bind both F-actin and AID while $Ca_v\beta$ dimerization is incompatible with such hetero-interactions.

The aforementioned pieces of evidence may explain why $Ca_v\beta$/F-actin and $Ca_v\beta$/$Ca_v\beta$ interactions have different functional outcomes on VGCC fate. As a monomer, $Ca_v\beta$ can interact with F-actin and supports the clearance of defective calcium channels at the cell surface, while as a dimer, $Ca_v\beta$ interacts with dynamin and decreases it by channel internalization[30,31]. In essence, calcium channels availability at the cellular membrane is critically controlled by these two PPI and the different $Ca_v\beta$ oligomerization states (Figure 4.2).

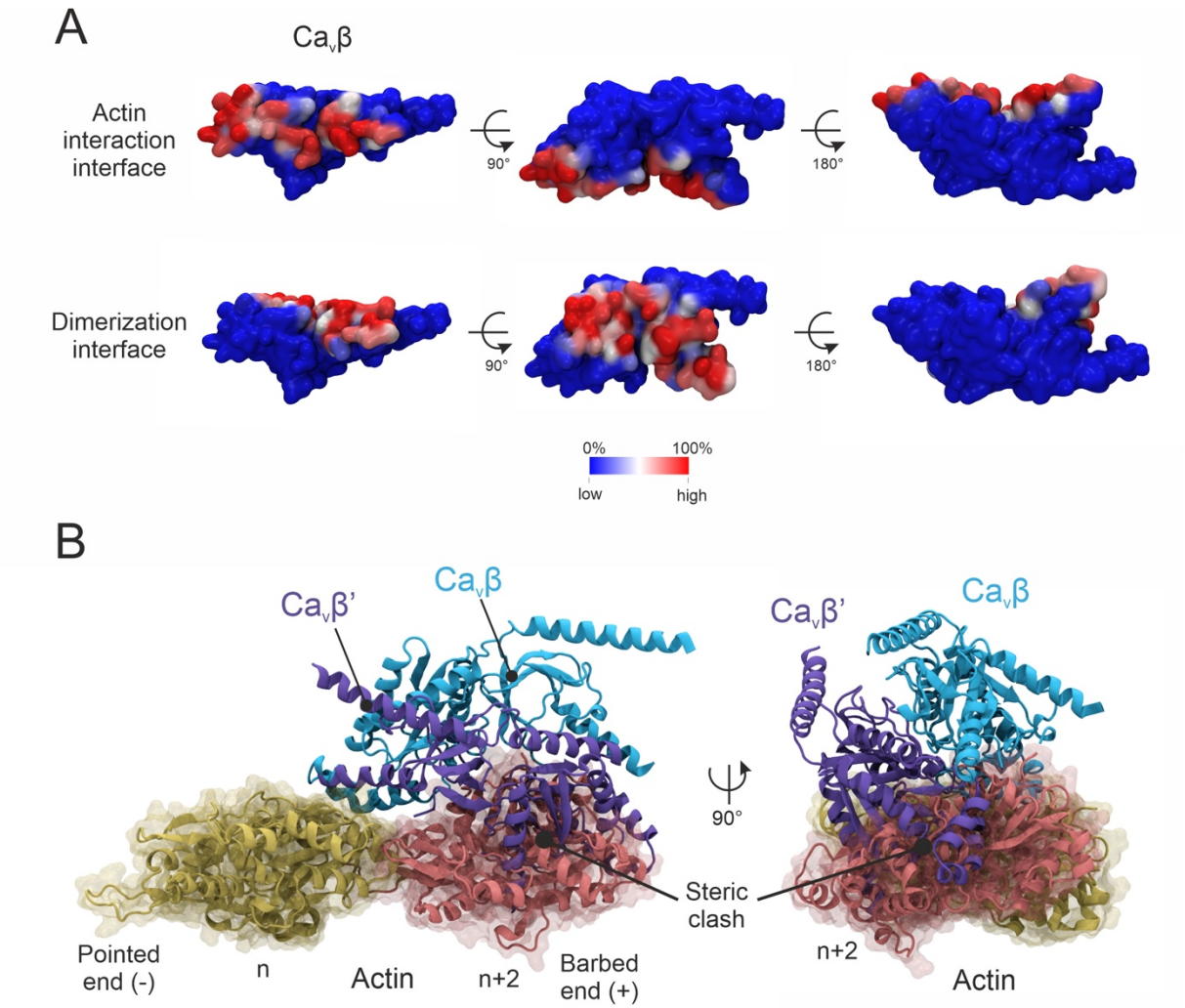

Figure 4.1. $Ca_v\beta$ is an interactive module. **A**) Actin interface and the dimerization interface are illustrated as contact frequencies on a surface representation of $Ca_v\beta$ poses. **B)** $Ca_v\beta$/Actin interaction and $Ca_v\beta$ dimerization are structurally exclusive interactions. Structural superimposition of $Ca_v\beta$/Actin and $Ca_v\beta$/$Ca_v\beta$ models shows abundant steric clashes. Dimeric actin is represented as cartoon and transparent surface, with the two adjacent monomers in pink

and golden colour while $Ca_v\beta$ (originally belonging to $Ca_v\beta$/Actin model) in cartoon cyan and $Ca_v\beta$' (dimeric counterpart) in purple cartoon.

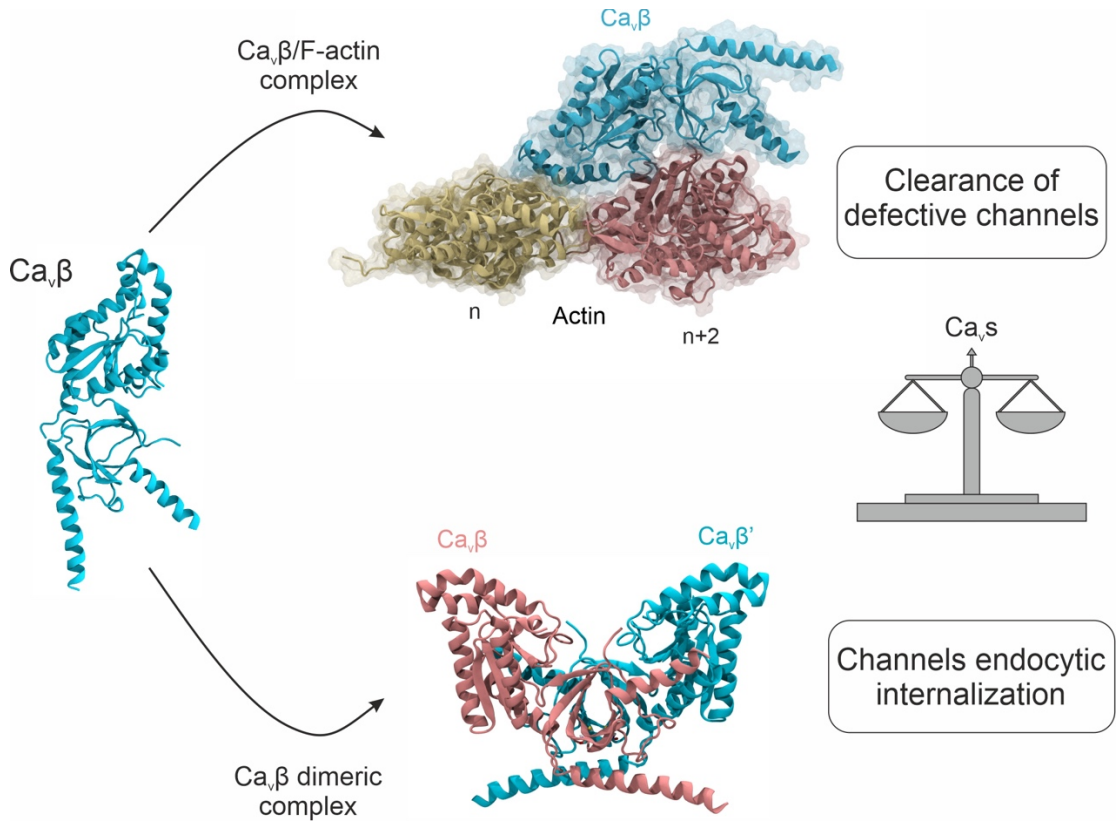

Figure 4.2. $Ca_v\beta$ interactors determine VGCC cell surface availability. $Ca_v\beta$ can bind F-actin and clear defective calcium channels from the cellular membrane. In contrast, dimeric $Ca_v\beta$ can interact with dynamin (not shown) and promote calcium channel internalization.

Chapter 5. Conclusions

In this thesis I first determine $Ca_v\beta$/F-actin interaction by means of XL-MS and protein-protein docking. $Ca_v\beta_2$ binds to a region between two adjacent monomers of actin that could be shared with other actin binding proteins. Interestingly, $Ca_v\beta$/F-actin interaction interface presents electrostatic complementarity, a feature that was experimentally demonstrated by its sensitivity to an increased ionic strength. Both $Ca_v\beta$ domains, SH3 and GK are involved in the interaction. Consequently, $Ca_v\beta_4$ was shown to have a comparable binding mode to $Ca_v\beta_2$.

Hotspots located at $Ca_v\beta$/F-actin interaction interface were predicted by CAS and experimentally validated in $Ca_v\beta_2$-core and $Ca_v\beta_4$ R482X backgrounds using co-sedimenation assays. A total of eight residues were found to be crucial for $Ca_v\beta$/F-actin binding. Whole cell currents from cells co-expressing a $Ca_v1.2$ and either a $Ca_v\beta_2$ or $Ca_v\beta_2$ bearing Ala mutations in the identified hotspots showed a significantly decreased amplitude of the ionic current peak. Such observation was due to a proportionally reduced number of conductive channels at the cellular membrane as demonstrated by stationary noise analysis. In summary, impeding $Ca_v\beta$/F-actin interaction subsequently altered VGCCs quality control and the clearance of defective channels at the cell surface.

In the second part of my thesis, I modelled $Ca_v\beta$ dimerization by protein-protein docking and filtering based on experimental data derived by XL-MS. $Ca_v\beta$ dimerizes in a head-to-tail conformation. This dimeric conformation is *condicio sine qua non* for the formation of a double disulphide bridge involving C113. Interestingly, the $Ca_v\beta$ dimeric model is incompatible with AID binding, indicating that $Ca_v\beta$ dimerization and $Ca_v\beta$ binding to Ca_vs are exclusive interactions. CAS followed by site-directed mutagenesis allowed the identification of six hotspots at the $Ca_v\beta$ dimeric surface. Ala mutation of these hotspots decreased $Ca_v\beta$ dimeric fraction assessed by BN-PAGE. This dimerization impaired $Ca_v\beta$ mutant could be used in further studies to continue deciphering $Ca_v\beta$ dimerization roles *in vivo*.

Third, I performed a comparative analysis of the $Ca_v\beta$/F-actin complex and $Ca_v\beta$ dimer, showing that both interactions are mutually exclusive. Such exclusiveness makes physiological sense when considering that both interactions would have different functional outcomes on

calcium channels cell surface availability. As a monomer, $Ca_v\beta$ interacts with F-actin and supports the clearance of defective calcium channels at the cellular membrane, while as a dimer $Ca_v\beta$ can interact with dynamin and promote their internalization.

Finally, through XL-MS, I obtained structural and functional information on two different non-amenable PPIs. The structural models generated in this thesis provide new druggable protein-proteins interfaces that could be used to intervene in crucial physiological processes such as muscle contraction, hormonal secretion, or synaptic transmission.

Publications

1. Castilla, F; Lugo, V; Miranda-Laferte, E; Jordan, N; Huesgen, P; Santiago-Schübel, B; Alfonso-Prieto, M; Hidalgo, P. Unveiling the molecular interface of $Ca_V\beta$-actin complex that regulates expression of functional $Ca_V1.2$ channels. (To be submitted)

   Contribution: I designed and performed the cloning of cDNA constructs encoding $Ca_v\beta$ used in this study and carried out the expression and purification of the proteins, *in vitro* cross-linking, analysed and collected all data for mass spectrometry, protein-protein docking, binding assays, western blots, laser scanning confocal microscopy, except for the electrophysiological data; prepared the figures and contributed to writing the manuscript.

2. Castilla, F; Marcus, K; Barkovits, K; P; Santiago-Schübel, B; Alfonso-Prieto, M; Hidalgo, P. Molecular characterisation of $Ca_V\beta$ dimerization. (Manuscript in preparation)

   Contribution: I performed cloning of DNA constructs, site-directed mutagenesis, optimization and purification of the proteins, stable isotopic labelling of proteins, pull-down assays and fluorescence spectroscopy, BN-PAGE, cross-linking experiments, protein-protein docking in HADDOCK, CAS, design of experiments, figures preparation and contributed to writing the manuscript.

Abbreviations

VGCC	Voltage-gated calcium channel
VSD	Voltage-sensing domain
$Ca_v\alpha_1$	Calcium channel α_1 subunit
$Ca_v\beta$	Calcium channel β auxiliary subunit
SH3	Src homology 3
GK	Guanylate kinase
XL-MS	Cross-linking mass spectrometry
ER	Endoplasmic reticulum
$[Ca^{2+}]_i$	Intracellular calcium concentration
LVACC	Low voltage-activated calcium channel
HVACC	High voltage-activated calcium channel
$Ca_v\gamma$	Calcium channel γ subunit
$Ca_v\alpha_2\delta$	Calcium channel α_2 and δ subunits
DHP	Dihydropyridine
AID	α_1 interaction domain
CTD	Carboxyterminal domain
PD	Pore domain
MAGUKs	Membrane-associated guanylate kinases
PDZ	PSD-95/DLG/ZO-1
ATP	Adenosine triphosphate
GMP	Guanosine monophosphate
VDA	Voltage-dependent activation
VDI	Voltage-dependent inactivation
SD	Subdomain
ABP	Actin binding protein
G-actin	Globular actin
F-actin	Filamentous actin
FRET	Fluorescence resonance energy transfer
RRP	Ready-realisable pool
SV	Synaptic vesicles

SEC	Size-exclusion chromatography
MS	Mass spectrometry
ESI	Electrospray ionization
MALDI	Matrix-assisted laser desorption/ionization
ToF	Time of flight
MS/MS	Tandem mass spectrometry
NMR	Nuclear magnetic resonance
Cryo-EM	Cryo-electron microscopy
DSS	Disuccinimidyl suberate
DSBU	Disuccinimidyl dibutyric urea
DSSO	Disuccinimidyl sulfoxide
NHS	N-hydroxysuccinimidyl
EDC	Carbodiimide hydrochloride
DHSO	Dihydrazide sulfoxide
PIRs	Protein interaction-reporters
CDI	N,N'-Carbonyldiimidazole
HADDOCK	High Ambiguity Driven biomolecular DOCKing
AIRs	Ambiguous Interaction Restraints
CPORT	Consensus Prediction Of interface Residues in Transient complexes
DMSO	Dimethyl sulfoxide
CAS	Computational alanine scanning
WT	Wild-type
ML	Machine Learning
IPTG	Isopropyl-D-thiogalactopyranoside
DTT	Dithiothreitol
HCD	Higher-energy C-trap dissociation
PDB	Protein Data Bank
NCS	NonCrystallographic symmetry
MD	Molecular dynamics
GST	Glutathione S-transferase
CM	Spectral center of mass
BN-PAGE	Blue-native gel electrophoresis

Acknowledgments

I hereby express my gratitude to the Board of Directors from Jülich Research Center (Forschungszentrum Jülich) for the funding of the project titled 'Multidisciplinary approach for mapping protein-protein interactions surfaces: From mass spectrometry to computational and cell biology' within the 'Networking doctoral candidates' ('Vernetzungsdoktoranden') program.

I also thank the directors of the institute areas where I conducted my research: Prof. Dr. Christoph Fahlke (Institute of Biological Information Processing – Molecular and Cellular Physiology (IBI-1)), Prof. Dr. Paolo Carloni (Institute for Advanced Simulation – Computational Biomedicine and Institute for Neuroscience and Medicine (IAS-5/INM-9) and Dr. Stephan Küppers (Central Institute of Engineering, Electronics and Analytics (ZEA-3)).

I thank the proteomics groups of Prof. Dr. Pitter Huesgen, Marcus Krüger and Andreas Schmidt from CECAD/CMMC Proteomics facility - University of Cologne and Prof. Dr. Katrin Marcus, Dr. Katalin Barkovits and Kathy Pfeiffer from the Medical-Proteome Center – Ruhr-University Bochum for the performance of LC-MS/MS measurements.

Although a few written words may not be enough to express my gratitude to all those people who have helped during the long and tough way to complete my thesis, I hope that together with some spoken words, I could make up for it.

I here thank my current and former IBI-1, ZEA-3 and IAS-5 colleagues: Claudia, Yulia, Juan, Bettina, Miriam, Andrei, Natasha, Bart, Felix, Piersilvio, Carène, Víctor, Bassam, Markus, Assalla, Joel, Cansu, Ignacio, Albert, Alexander, Maithy, Michelle, Henrique, Steffi, Thomas, Erick. I also thank Arne, Meike, Anita and Sia and sincerely and specially Nadine.

A special mention must go to my three PhD supervisors: Patty, Mercedes and Bea, from whom I have learnt scientific, but more importantly personal lessons, that will accompany me for good.

The only way to be able to thank you for your support these years, Katia, would involve rivers of ink. For that reason, I hope that a solely glance and time are enough.

Y finalmente no podía acabar estas páginas de mi vida sin agradecer a aquellas personas que me llevan apoyando desde el comienzo: amigos y familia. Abuelos, Abuelas, Mamá, Papá y Hermana mía.

A todos os dedico mi trabajo.

Bibliography

1. Clapham, D. E. Calcium Signaling. *Cell* **131**, 1047–1058 (2007).
2. Westheimer, F. H. *Why Nature Chose Phosphates*. *Science* **235** (4793), 1173-1178 (1987).
3. Berridge, M. J. , L. P. , & B. M. D. The versality and universality of calcium signalling. *Nat Rev Mol Cell Biol* **1**, 11–21 (2000).
4. Burgoyne, R. D. Neuronal calcium sensor proteins: Generating diversity in neuronal Ca 2+ signalling. *Nature Reviews Neuroscience* **8,** 182–193 (2007).
5. Schmitz, E. A., Takahashi, H. & Karakas, E. Structural basis for activation and gating of IP3 receptors. *Nat Commun* **13**, (2022).
6. Neely, A. & Hidalgo, P. Structure-function of proteins interacting with the α1 pore-forming subunit of high-voltage-activated calcium channels. *Front Physiol* **5**, (2014).
7. Hofmann, F., Flockerzi, V., Kahl, S. & Wegener, J. W. L-type CaV1. 2 calcium channels: from in vitro findings to in vivo function. *Physiol Rev* **94**, 303–326 (2014).
8. Marie, A., Yunker, R. & Mcenery, M. W. Low-Voltage-Activated ('T-Type') Calcium Channels in Review. *Journal of Bioenergetics and Biomembranes* **35** (2003).
9. Curtis, B. M. & Catterall, W. A. Purification of the calcium antagonist receptor of the voltage-sensitive calcium channel from skeletal muscle transverse tubules. *Biochemistry*, **23**(10), 2113-2118 (1984).
10. Campiglio, M. & Flucher, B. E. The Role of Auxiliary Subunits for the Functional Diversity of Voltage-Gated Calcium Channels. *Journal of Cellular Physiology* **230**, 2019–2031 (2015).
11. Klugbauer, N., Dai, S., Specht, V., Lacinová, L., Marais, E., Bohn, G., & Hofmann, F.. A family of γ-like calcium channel subunits. *FEBS letters* **470**(2), 189-197 (2000).
12. Buraei, Z. & Yang, J. The β subunit of voltage-gated Ca2+ channels. *Physiological Reviews*. **90**, 1461–1506 (2010).
13. Wu, J. *et al.* Structure of the voltage-gated calcium channel Cav1.1 at 3.6 Å resolution. *Nature* **537**, 191–196 (2016).
14. Catterall, W. A. Voltage-gated calcium channels. *Cold Spring Harb Perspect Biol* **3**, 1–23 (2011).

15. Catterall, W. A., Perez-Reyes, E., Snutch, T. P. & Striessnig, J. International Union of Pharmacology. XLVIII. Nomenclature and structure-function relationships of voltage-gated calcium channels. *Pharmacological Reviews* **57**, 411–425 (2005).
16. Zamponi, G. W., Striessnig, J., Koschak, A. & Dolphin, A. C. The physiology, pathology, and pharmacology of voltage-gated calcium channels and their future therapeutic potential. *Pharmacol Rev* **67**, 821–870 (2015).
17. Dolphin, A. C. Calcium channel auxiliary α 2 δ and β subunits: Trafficking and one step beyond. *Nature Reviews Neuroscience* **13**, 542–555 (2012).
18. Embden, J. D. A. V *et al.* Primary Structure of the i Subunit of the DHP-Sensitive Calcium Channel from Skeletal Muscle. *J. Immunol* **17**, (1987).
19. Rima, M. *et al.* Protein partners of the calcium channel β subunit highlight new cellular functions. *Biochemical Journal* **473**, 1831–1844 (2016).
20. Van Petegem, F., Clark, K. A., Chatelain, F. C. & Minor, D. L. Structure of a complex between a voltage-gated calcium channel β-subunit and an α-subunit domain. *Nature* **429**, 671–675 (2004).
21. Opatowsky, Y. & Hirsch, J. A. Structural Analysis of the Voltage-Dependent Calcium Channel β Subunit Functional Core and Its Complex with the α1 Interaction Domain. *Neuron* **42**, 387–399 (2004).
22. Chen, Y. H. , & Yang, J. Structural basis of the α1–β subunit interaction of voltage-gated Ca2+ channels. . *Nature* **429**, 675–680 (2004).
23. Zhu, J., Shang, Y., Chen, J. & Zhang, M. Structure and function of the guanylate kinase-like domain of the MAGUK family scaffold proteins. *Frontiers in Biology* **7**, 379–396 (2012).
24. Shin, H., Hsueh, Y.-P., Yang, F.-C., Kim, E. & Sheng, M. An intramolecular interaction between Src homology 3 domain and guanylate kinase-like domain required for channel clustering by postsynaptic density-95/SAP90. *Journal of Neuroscience*, **20**(10), 3580-3587. (2000).
25. Maximov, A., Südhof, T. C. & Bezprozvanny, I. Association of neuronal calcium channels with modular adaptor proteins. *Journal of Biological Chemistry* **274**, 24453–24456 (1999).
26. Garcia, E. P. *et al.* SAP90 Binds and Clusters Kainate Receptors Causing Incomplete Desensitization. *Neuron* **21**, (1998).
27. Li, Y., Zhang, Y. & Yan, H. Kinetic and thermodynamic characterizations of yeast guanylate kinase. *Journal of Biological Chemistry*, **271**(45), 28038-28044 (1996).

28. Zhu, J., Shang, Y. & Zhang, M. Mechanistic basis of MAGUK-organized complexes in synaptic development and signalling. *Nature Reviews Neuroscience* **17**, 209–223 (2016).
29. Schredelseker, J., Dayal, A., Schwerte, T., Franzini-Armstrong, C. & Grabner, M. Proper restoration of excitation-contraction coupling in the dihydropyridine receptor β 1-null zebrafish relaxed is an exclusive function of the β 1a subunit. *Journal of Biological Chemistry* **284**, 1242–1251 (2009).
30. Gonzalez-Gutierrez, G., Miranda-Laferte, E., Neely, A. & Hidalgo, P. The Src homology 3 domain of the β-subunit of voltage-gated calcium channels promotes endocytosis via dynamin interaction. *Journal of Biological Chemistry* **282**, 2156–2162 (2007).
31. Miranda-Laferte, E. *et al.* Homodimerization of the Src homology 3 domain of the calcium channel β-subunit drives dynamin-dependent endocytosis. *Journal of Biological Chemistry* **286**, 22203–22210 (2011).
32. Tadmouri, A. *et al.* Cacnb4 directly couples electrical activity to gene expression, a process defective in juvenile epilepsy. *EMBO Journal* **31**, 3730–3744 (2012).
33. Cruz-Garcia, Y. *et al.* Nanoenviroments of the β-Subunit of L-Type Voltage-Gated Calcium Channels in Adult Cardiomyocytes. *Front Cell Dev Biol* **9**, (2022).
34. Bichet, D. *et al.* The I-II Loop of the Ca 2 Channel 1 Subunit Contains an Endoplasmic Reticulum Retention Signal Antagonized by the Subunit A switch in channel state from silent to. *Neuron* **25**, (2000).
35. Cornet, V. *et al.* Multiple determinants in voltage-dependent P/Q calcium channels control their retention in the endoplasmic reticulum. *European Journal of Neuroscience* **16**, 883–895 (2002).
36. Altier, C. *et al.* The Cavβ subunit prevents RFP2-mediated ubiquitination and proteasomal degradation of L-type channels. *Nature Neuroscience* **14**, 173–182 (2011).
37. Canti, C., Bogdanov, Y. & Dolphin, A. C. Interaction between G proteins and accessory β subunits in the regulation of α1B calcium channels in Xenopus oocytes. *Journal of Physiology* **527**, 419–432 (2000).
38. De Waard, M. & Campbell, K. P. Subunit regulation of the neuronal alpha 1A Ca2+ channel expressed in Xenopus oocytes. *J Physiol* **485**, 619–634 (1995).
39. Neely, A., Garcia-Olivares, J., Voswinkel, S., Horstkott, H. & Hidalgo, P. Folding of active calcium channel β1b-subunit by size-exclusion chromatography and its role on channel function. *Journal of Biological Chemistry* **279**, 21689–21694 (2004).
40. Josephson, I. R. & Varadi, G. The β subunit increases Ca2+ currents and gating charge movements of human cardiac L-type Ca2+ channels. *Biophys J* **70**, 1285–1293 (1996).

41. Pollard, T. D. Actin and actin-binding proteins. *Cold Spring Harb Perspect Biol* **8**, (2016).
42. Reynolds, M. J., Hachicho, C., Carl, A. G., Gong, R. & Alushin, G. M. Bending forces and nucleotide state jointly regulate F-actin structure. *Nature* **611**, 380–386 (2022).
43. Rottner, K., Faix, J., Bogdan, S., Linder, S. & Kerkhoff, E. Actin assembly mechanisms at a glance. *J Cell Sci* **130**, 3427–3435 (2017).
44. Bezanilla, M., Gladfelter, A. S., Kovar, D. R. & Lee, W. L. Cytoskeletal dynamics: A view from the membrane. *Journal of Cell Biology* **209**, 329–337 (2015).
45. Virtanen, J. A. & Vartiainen, M. K. Diverse functions for different forms of nuclear actin. *Current Opinion in Cell Biology* **46**, 33–38 (2017).
46. Plessner, M., Melak, M., Chinchilla, P., Baarlink, C. & Grosse, R. Nuclear F-actin formation and reorganization upon cell spreading. *Journal of Biological Chemistry* **290**, 11209–11216 (2015).
47. Caridi, C. P. *et al.* Nuclear F-actin and myosins drive relocalization of heterochromatic breaks. *Nature* **559**, 54–60 (2018).
48. Baarlink, C. *et al.* A transient pool of nuclear F-actin at mitotic exit controls chromatin organization. *Nat Cell Biol* **19**, 1389–1399 (2017).
49. Stölting, G. *et al.* Direct interaction of CaVβ with actin up-regulates l-type calcium currents in HL-1 cardiomyocytes. *Journal of Biological Chemistry* **290**, 4561–4572 (2015).
50. Guzman, G. A., Guzman, R. E., Jordan, N. & Hidalgo, P. A tripartite interaction among the calcium channel α1- and β-subunits and f-actin increases the readily releasable pool of vesicles and its recovery after depletion. *Front Cell Neurosci* **13**, (2019).
51. Conrad, R. *et al.* Rapid Turnover of the Cardiac L-Type CaV1.2 Channel by Endocytic Recycling Regulates Its Cell Surface Availability. *iScience* **7**, 1–15 (2018).
52. Conrad, R., Kortzak, D., Guzman, G. A., Miranda-Laferte, E. & Hidalgo, P. CaVβ controls the endocytic turnover of CaV1.2 L-type calcium channel. *Traffic* **22**, 180–193 (2021).
53. Lao, Q. Z., Kobrinsky, E., Liu, Z. & Soldatov, N. M. Oligomerization of Ca v β subunits is an essential correlate of Ca 2+ channel activity . *The FASEB Journal* **24**, 5013–5023 (2010).
54. Page, K. M. *et al.* N terminus is key to the dominant negative suppression of CaV2 calcium channels: Implications for episodic ataxia type 2. *Journal of Biological Chemistry* **285**, 835–844 (2010).

55. Li, Y. *et al.* Structure of Crumbs tail in complex with the PALS1 PDZ-SH3-GK tandem reveals a highly specific assembly mechanism for the apical Crumbs complex. *Proc Natl Acad Sci U S A* **111**, 17444–17449 (2014).
56. Domon, B. & Aebersold, R. Mass spectrometry and protein analysis. *Science*, **312** (5771), 212-217 (2006).
57. Glish, G. L. & Vachet, R. W. The basics of mass spectrometry in the twenty-first century. *Nature Reviews Drug Discovery* **2**, 140–150 (2003).
58. Prabhu, G. R. D., Williams, E. R., Wilm, M. & Urban, P. L. Mass spectrometry using electrospray ionization. *Nature Reviews Methods Primers* **3**, (2023).
59. Yu, C. & Huang, L. Cross-Linking Mass Spectrometry: An Emerging Technology for Interactomics and Structural Biology. *Analytical Chemistry* **90**, 144–165 (2018).
60. O'Reilly, F. J. & Rappsilber, J. Cross-linking mass spectrometry: methods and applications in structural, molecular and systems biology. *Nature Structural and Molecular Biology* **25**, 1000–1008 (2018).
61. Gutierrez, C. B. *et al.* Developing an acidic residue reactive and sulfoxide-containing MS-cleavable homobifunctional cross-linker for probing protein-protein interactions. *Anal Chem* **88**, 8315–8322 (2016).
62. Piotrowski, C., Ihling, C. H. & Sinz, A. Extending the cross-linking/mass spectrometry strategy: Facile incorporation of photo-activatable amino acids into the model protein calmodulin in Escherichia coli cells. *Methods* **89**, 121–127 (2015).
63. Iacobucci, C. & Sinz, A. To Be or Not to Be? Five Guidelines to Avoid Misassignments in Cross-Linking/Mass Spectrometry. *Anal Chem* **89**, 7832–7835 (2017).
64. Holding, A. N. XL-MS: Protein cross-linking coupled with mass spectrometry. *Methods* **89**, 54–63 (2015).
65. Iacobucci, C. *et al.* A cross-linking/mass spectrometry workflow based on MS-cleavable cross-linkers and the MeroX software for studying protein structures and protein–protein interactions. *Nat Protoc* **13**, 2864–2889 (2018).
66. Chambers, M. C. *et al.* A cross-platform toolkit for mass spectrometry and proteomics. *Nature Biotechnology* **30**, 918–920 (2012).
67. Cox, J. & Mann, M. MaxQuant enables high peptide identification rates, individualized p.p.b.-range mass accuracies and proteome-wide protein quantification. *Nat Biotechnol* **26**, 1367–1372 (2008).

68. Yllmaz, Ş., Busch, F., Nagaraj, N. & Cox, J. Accurate and Automated High-Coverage Identification of Chemically Cross-Linked Peptides with MaxLynx. *Anal Chem* **94**, 1608–1617 (2022).
69. Lu, L. *et al.* Identification of MS-Cleavable and Noncleavable Chemically Cross-Linked Peptides with MetaMorpheus. *J Proteome Res* **17**, 2370–2376 (2018).
70. Lima, D. B. *et al.* SIM-XL: A powerful and user-friendly tool for peptide cross-linking analysis. *J Proteomics* **129**, 51–55 (2014).
71. De Vries, S. J., Van Dijk, M. & Bonvin, A. M. J. J. The HADDOCK web server for data-driven biomolecular docking. *Nat Protoc* **5**, 883–897 (2010).
72. Orbán-Németh, Z. *et al.* Structural prediction of protein models using distance restraints derived from cross-linking mass spectrometry data. *Nat Protoc* **13**, 478–494 (2018).
73. Graziadei, A. & Rappsilber, J. Leveraging crosslinking mass spectrometry in structural and cell biology. *Structure* **30**, 37–54 (2022).
74. Klykov, O. *et al.* Efficient and robust proteome-wide approaches for cross-linking mass spectrometry. *Nat Protoc* **13**, 2964–2990 (2018).
75. Bonvin Lab. HADDOCK tutorial for the use of MS crosslink data to guide docking. https://www.bonvinlab.org/education/HADDOCK-Xlinks/.
76. Bonvin, A. M. J. J., Karaca, E., Kastritis, P. L. & Rodrigues, J. P. G. L. M. Defining distance restraints in HADDOCK. *Nature Protocols* **13**, 1503 (2018).
77. Bonvin Lab. HADDOCK2.4 manual - Ambiguous Interaction Restraints (AIRs). https://www.bonvinlab.org/software/haddock2.4/airs/.
78. de Vries, S. J. & Bonvin, A. M. J. J. Cport: A consensus interface predictor and its performance in prediction-driven docking with HADDOCK. *PLoS One* **6**, (2011).
79. Van Zundert, G. C. P. & Bonvin, A. M. J. J. DisVis: Quantifying and visualizing accessible interaction space of distance-restrained biomolecular complexes. *Bioinformatics* **31**, 3222–3224 (2015).
80. van Zundert, G. C. P. *et al.* The DisVis and PowerFit Web Servers: Explorative and Integrative Modeling of Biomolecular Complexes. *J Mol Biol* **429**, 399–407 (2017).
81. Bonvin Lab. DisVis web server Tutorial. https://www.bonvinlab.org/education/Others/disvis-webserver/.
82. Van Zundert, G. C. P. *et al.* The HADDOCK2.2 Web Server: User-Friendly Integrative Modeling of Biomolecular Complexes. *J Mol Biol* **428**, 720–725 (2016).
83. S. Hubbard and J. Thornton. 1993. NACCESS, Computer Program. Department of Biochemistry Molecular Biology, University College London.

84. G. van Rossum, Python tutorial, Technical Report CS-R9526, Centrum voor Wiskunde en Informatica (CWI), Amsterdam, May 1995.

85. Humphrey, W., Dalke, A., & Schulten, K.. VMD: visual molecular dynamics. *Journal of molecular graphics*, **14**(1), 33-38 (1996).

86. Clackson, T., & Wells, J. A.. A hot spot of binding energy in a hormone-receptor interface. *Science*, **267**(5196), 383-386 (1995).

87. Kortemme, T., Kim, D. E. & Baker, D. Computational alanine scanning of protein-protein interfaces. *Sci STKE* **2004**, (2004).

88. Dehouck, Y., Kwasigroch, J. M., Rooman, M. & Gilis, D. BeAtMuSiC: Prediction of changes in protein-protein binding affinity on mutations. *Nucleic Acids Res* **41**, (2013).

89. Pahari, S. *et al.* SAAMBE-3D: Predicting effect of mutations on protein–protein interactions. *Int J Mol Sci* **21**, (2020).

90. Li, M., Simonetti, F. L., Goncearenco, A. & Panchenko, A. R. MutaBind estimates and interprets the effects of sequence variants on protein–protein interactions. *Nucleic Acids Res* **44**, W494–W501 (2016).

91. Meireles, L. M. C., Dömling, A. S. & Camacho, C. J. ANCHOR: A web server and database for analysis of protein-protein interaction binding pockets for drug discovery. *Nucleic Acids Res* **38**, (2010).

92. Wood, C. W. *et al.* BAlaS: Fast, interactive and accessible computational alanine-scanning using BudeAlaScan. *Bioinformatics* **36**, 2917–2919 (2020).

93. Rodrigues, C. H. M., Myung, Y., Pires, D. E. V. & Ascher, D. B. MCSM-PPI2: predicting the effects of mutations on protein-protein interactions. *Nucleic Acids Res* **47**, W338–W344 (2019).

94. Kim, D. E., Chivian, D. & Baker, D. Protein structure prediction and analysis using the Robetta server. *Nucleic Acids Res* **32**, (2004).

95. Winkler, R. ESIprot: A universal tool for charge state determination and molecular weight calculation of proteins from electrospray ionization mass spectrometry data. *Rapid Communications in Mass Spectrometry* **24**, 285–294 (2010).

96. Marcus, K., Eisenacher, M., & Sitek, B. (Eds.).. *Quantitative methods in proteomics*. Totowa, NJ, USA: Humana Press. **893**, (2012)

97. Bonvin Lab. HADDOCK CASP-CAPRI T70 ab-initio docking tutorial.

98. Gowers, R. J. *et al. MDAnalysis: A Python Package for the Rapid Analysis of Molecular Dynamics Simulations*. *PROC. OF THE 15th PYTHON IN SCIENCE CONF* **98**, 105 (2016).

99. Michaud-Agrawal, N., Denning, E. J., Woolf, T. B. & Beckstein, O. MDAnalysis: A toolkit for the analysis of molecular dynamics simulations. *J Comput Chem* **32**, 2319–2327 (2011).

100. Hunter, J. D.. Matplotlib: A 2D graphics environment. *Computing in science & engineering*, **9**(03), 90-95 (2007).

101. Waskom, M. seaborn: statistical data visualization. *J Open Source Softw* **6**, 3021 (2021).

102. Niepmann, M. & Zheng, J. Discontinuous native protein gel electrophoresis. *Electrophoresis* **27**, 3949–3951 (2006).

103. Lima, D. B. *et al.* Characterization of homodimer interfaces with cross-linking mass spectrometry and isotopically labeled proteins. *Nat Protoc* **13**, 431–458 (2018).

104. Norris, N. C. *et al.* Structural and biophysical analyses of the skeletal dihydropyridine receptor β subunit β1a reveal critical roles of domain interactions for stability. *Journal of Biological Chemistry* **292**, 8401–8411 (2017).

105. Rumfeldt, J. A. O., Galvagnion, C., Vassall, K. A. & Meiering, E. M. Conformational stability and folding mechanisms of dimeric proteins. *Progress in Biophysics and Molecular Biology* **98**, 61–84 (2008).

106. Whitten, A. E., Jeffries, C. M., Harris, S. P., & Trewhella, J. (2008). Cardiac myosin-binding protein C decorates F-actin: implications for cardiac function. *Proceedings of the National Academy of Sciences*, **105**(47), 18360-18365. (2008).

107. Iwamoto, D. V. *et al.* Structural basis of the filamin A actin-binding domain interaction with F-actin. *Nat Struct Mol Biol* **25**, 918–927 (2018).

108. Oosterheert, W., Klink, B. U., Belyy, A., Pospich, S. & Raunser, S. Structural basis of actin filament assembly and aging. *Nature* **611**, 374–379 (2022).

109. Kumari, A., Kesarwani, S., Javoor, M. G., Vinothkumar, K. R. & Sirajuddin, M. Structural insights into actin filament recognition by commonly used cellular actin markers. *EMBO J* **39**, (2020).

110. Galkin, V. E., Orlova, A., Schröder, G. F. & Egelman, E. H. Structural polymorphism in F-actin. *Nat Struct Mol Biol* **17**, 1318–1323 (2010).

111. Merino, F. *et al.* Structural transitions of F-actin upon ATP hydrolysis at near-atomic resolution revealed by cryo-EM. *Nat Struct Mol Biol* **25**, 528–537 (2018).

112. Scheffner, M. & Kumar, S. Mammalian HECT ubiquitin-protein ligases: Biological and pathophysiological aspects. *Biochim Biophys Acta Mol Cell Res* **1843**, 61–74 (2014).

113. Manning, J. A. & Kumar, S. Physiological functions of Nedd4-2: lessons from knockout mouse models. *Trends in biochemical sciences*, **43**(8), 635-647 (2018).

114. Walker, R. G. *et al.* The structure of human apolipoprotein A-IV as revealed by stable isotope-assisted cross-linking, molecular dynamics, and small angle X-ray scattering. *Journal of Biological Chemistry* **289**, 5596–5608 (2014).

115. Rehkamp, A. *et al.* First 3D-Structural Data of Full-Length Guanylyl Cyclase 1 in Rod-Outer-Segment Preparations of Bovine Retina by Cross-Linking/Mass Spectrometry. *J Mol Biol* **433**, (2021).

116. Pettelkau, J. *et al.* Structural analysis of guanylyl cyclase-activating protein-2 (GCAP-2) homodimer by stable isotope-labeling, chemical cross-linking, and mass spectrometry. *J Am Soc Mass Spectrom* **24**, 1969–1979 (2013).